J. Mech. Phys. Solids 219 (2027) 106905

Contents lists available at ScienceDirect

Journal of the Mechanics and Physics of Solids

journal homepage: www.elsevier.com/locate/jmps

Nonlinear thermoelastic contact between a rigid indenter and a wavy surface

Lizichen Chen [a], Yangkun Du [a,*], Yafei Wang [b,c], Zhanfeng Li [d], Zihao Du [a], Zhuangzhuang He [a], Rongqiao Xu [e], Michel Destrade [a,f], Gangfeng Wang [g,*], C.W. Lim [a], Weiqiu Chen [a,h,i,f,*]

[a] State Key Laboratory of Fluid Power and Mechatronic Systems, Key Laboratory of Soft Machines and Smart Devices of Zhejiang Province, Department of Engineering Mechanics, Soft Matter Research Center, Zhejiang University, Hangzhou, 310027, PR China
[b] National Key Laboratory of Science and Technology on Advanced Composites in Special Environments, Harbin, 150001, PR China
[c] Center for Composite Materials and Structure, Harbin Institute of Technology, Harbin, 150001, PR China
[d] School of Civil Engineering and Transportation, South China University of Technology, Guangzhou, 510641, PR China
[e] Department of Civil Engineering, Zhejiang University, Hangzhou, 310051, PR China
[f] School of Mathematical and Statistical Sciences, University of Galway, University Road, Galway, Ireland
[g] Department of Engineering Mechanics, SVL and MMML, Xi'an Jiaotong University, Xi'an, 710049, PR China
[h] Intelligent Structures and Advanced Equipments Technology (ISAET) Center, Huanjiang Laboratory, Zhejiang University, Zhuji, 311800, PR China
[i] Faculty of Mechanical Engineering and Mechanics, Ningbo University, Ningbo, 315211, PR China

ARTICLE INFO

Keywords:
Contact analysis
Wavy surfaces
Adhesive contact
Potential theory method
Instability analysis

ABSTRACT

Accurate modeling of the contact between a mold and an imprint resist under finite deformation remains a critical challenge in nanoimprint lithography. This paper presents a theoretical framework for analyzing thermoelastic contact problems in pre-deformed hyperelastic materials. Within the framework of nonlinear thermoelasticity, incremental governing equations are derived in the updated Lagrangian formulation. General solutions to the incremental governing equations are expressed as combinations of quasi-harmonic functions based on the generalized Almansi's theorem. The potential theory method is developed to solve the problem of frictionless thermoelastic contact between a rigid indenter and a hyperelastic half-space under prescribed incremental mechanical and thermal boundary conditions. Single-layer potentials are constructed, and their densities are explicitly obtained by inverting the resulting integro-differential equations. Closed-form expressions obtained for incremental displacement, temperature field, stress components, and incremental indentation force are validated through finite element simulations, showing excellent agreement for small perturbations. This framework is then extended to a hyperelastic film bonded to a rigid substrate using the generalized image method, where Fredholm integral equations of the second kind arise and are solved iteratively by establishing contraction mappings according to the Banach-Caccioppoli theorem. For wavy surfaces, adhesive contact is analyzed using an energy release rate criterion, leading to an extended JKR model that incorporates thermal effects, pre-stretch, and surface topography. The modified JKR solution reveals that pre-stretch can modulate the equivalent modulus, equivalent inverse temperature, and surface waviness, thereby enabling tunable interface strength. Surface instability-induced waviness is further investigated, where a computational buckling analysis in the total Lagrangian formulation is performed to generate ini-

* Corresponding authors.
E-mail addresses: lzcchen@zju.edu.cn (L. Chen), yangkundu@zju.edu.cn (Y. Du), yafeiwang@hit.edu.cn (Y. Wang), zhanfengli@scut.edu.cn (Z. Li), zihaodu@outlook.com (Z. Du), 468456160@qq.com (Z. He), xurongqiao@zju.edu.cn (R. Xu), michel.destrade@nuigalway.ie (M. Destrade), wanggf@mail.xjtu.edu.cn (G. Wang), cwlim@zju.edu.cn (C.W. Lim), chenwq@zju.edu.cn (W. Chen).

https://doi.org/10.1016/j.jmps.2026.106905
Received 25 July 2026; Received in revised form 5 October 2026; Accepted 3 November 2026
Available online 5 November 2026
0022-5096/© 2026 Elsevier Ltd. All rights are reserved, including those for text and data mining, AI training, and similar technologies.

tial imperfections, followed by contact simulation using the augmented Lagrangian method. This work establishes a systematic analytical foundation for thermoelastic contact in soft materials under finite deformation, with implications for precision surface engineering and manufacturing.

1. Introduction

The reliable description of contact between a rigid indenter and a soft material undergoing finite deformations is essential for technologies such as transfer printing (Meitl et al., 2006; Carlson et al., 2012; Linghu et al., 2018), microindentation of biological tissues (Li et al., 2007; McKee et al., 2011), and the fabrication of surface relief structures via nanoimprint (Lan and Ding, 2010; Chen, 2015b). In this regime, contact is not merely a boundary condition but a governing mechanism that controls stress distribution, adhesion, friction, and morphological replication (Barber and Ciavarella, 2000; Popov et al., 2010). However, the contact involving soft materials such as crosslinked elastomers, polymer gels, and biological membranes is far more complex than that in metallic or ceramic materials (Du et al., 2023; Mu et al., 2025, 2026). This complexity stems from the fact that large deformation, constitutive nonlinearity, surface adhesion, and thermal stimuli frequently interact with one another. Nanoimprint lithography (Chou et al., 1995; Chou and Zhuang, 1999; Guo, 2007) and related soft pattern transfer processes (Wang et al., 2024b, 2025) provide a representative example. During fabrication, a compliant polymeric or elastomeric substrate may be stretched before contact in order to tune feature dimensions, suppress defects, or facilitate release. Simultaneously, heating is often applied to modify the rheological or thermoelastic response of the medium and to promote faithful topographic replication (Yu et al., 2026). The final patterning outcome depends not only on bulk deformation but also on the morphology of the contacting interface. This morphology may be externally imposed by the mold geometry or may arise spontaneously through wrinkling, creasing, or other instability driven processes (Huang et al., 2008). In both cases, the local topography determines pressure distribution, gap evolution, and interfacial adhesion over the contact area. Because soft materials are highly sensitive to prestress and temperature, even modest changes in processing conditions can alter tangent stiffness and the evolution of contact area in a substantial way. Accordingly, a predictive description of imprinting requires a framework that can consistently treat pre-deformation, thermal effects, adhesion, and surface geometry in a coupled manner. (Fig. 1)

The development of contact mechanics has historically proceeded from the Hertzian theory (Hertz, 1882; Johnson, 1982), which established the foundational relation between indentation load, displacement, and contact radius for smooth non-adhesive elastic bodies under the assumptions of linear constitutive behavior and infinitesimal strain. While this classical framework remains indispensable, its direct applicability to soft materials is limited because elastomers and gels often undergo large deformation prior to or during contact. As a result, the stress and deformation increment should be described based on the deformed state when contacting with a rubberlike material subjected to pre-stretch or large indentation. An effective strategy is provided by incremental field theory, in which a large pre -deformation is imposed on the initial configuration and subsequent contact loading is treated as a small perturbation (Dorfmann and Ogden, 2014). The resulting incremental governing equations capture the essential influence of the pre-deformation through non-isotropic tangent moduli, while remaining accessible to analytical or semi-analytical treatment. This perspective is deeply rooted in the continuum theories of incremental elasticity, and has proven useful in wave propagation (Dowaikh and Ogden, 1990), surface instability (Ogden, 1992), and indentation in pre-stretched media (Zhang et al., 2012). In parallel with these developments, the potential theory method has emerged as a powerful tool in contact and fracture analyses (Fabrikant, 1989). In particular, the formulations established by Fabrikant and subsequent extensions have shown that a broad class of contact problems in transversely isotropic media can be reduced to tractable integral representations. Zhang et al. (2012) successfully extended the potential theory method to contact analysis of compressible isotropic soft electroactive half -spaces under uniform finite deformation, showing its feasibility for problems with finite pre-deformation and electromechanical coupling. Huang et al. (2016) and Xia et al. (2020, 2023) subsequently applied the method to solve soft electroactive and magnetoactive contact problems and derived the Green's functions analytically. The potential theory method is attractive for its direct treatment of Abel integral equations, but its extension to thermal contact analysis of pre-deformed hyperelastic materials remains incomplete. Adding thermal effects introduces substantial complexity (Jesse et al., 2008; Yang and Jin, 2014). A non-uniform temperature field induces inhomogeneous thermal expansion, which makes the displacement field incompatible. As a result, constructing a potential function for thermoelasticity is more challenging than for electromechanical or magnetomechanical couplings, although Chen (2015a) did construct such a potential for the linear elastic regime. Additional complications arise from finite deformation, specifically the requirement of objective stress rates. Moreover, nanoimprinting typically deals with film-substrate systems, but applying potential theory to such systems via the generalized image method (Fabrikant, 2004) remains challenging. Fabrikant (2011a,b) attempted a constructive solution for contact analysis of a linear elastic film-substrate system, but the convergence of the iterative solution of the resulting Fredholm integral equation has not been fully resolved and requires further investigation.

Another important aspect of contact analysis concerns the role of surface morphology and adhesion. The classical theories of adhesive contact, including the Johnson-Kendall-Roberts (JKR) (Johnson et al., 1971), Derjaguin-Muller-Toporov (DMT) (Derjaguin et al., 1975), and Maugis-Dugdale (MD) (Maugis, 1992) models, established the balance between elastic deformation and interfacial surface energy for smooth bodies and clarified the transition between short-range and long-range adhesion regimes (Huang et al., 2026). These theories have had lasting impact because adhesion is especially significant in soft materials, where low modulus and large compliance allow surface forces to influence contact geometry. However, real interfaces are rarely perfectly smooth. Instead, they exhibit roughness or waviness over a spectrum of scales, whether generated by fabrication, environmental exposure, or intentional design (Li et al., 2026). Considerable investigations have therefore examined how topography modifies adhesion and contact stiffness. For statistically rough surfaces, early insights such as those of Fuller and Tabor (Fuller and Tabor, 1975; Greenwood, 2017)

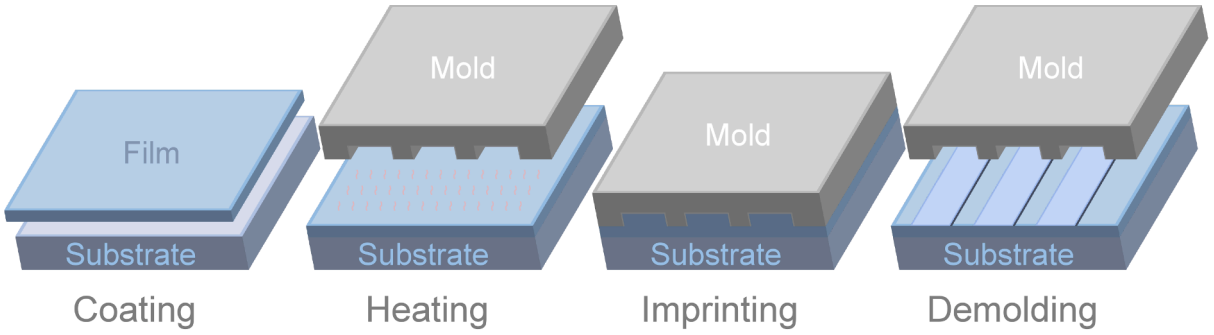


Fig. 1. Schematic of the thermal nanoimprint. A uniform resist film is first deposited on the substrate by spin coating and subsequently heated above its transition temperature to enable viscous flow. A hard mold bearing nanoscale relief patterns is then pressed into the softened resist under precisely controlled pressure and dwell time, achieving high-fidelity pattern replication. After the resist is cooled and solidified, the mold is separated from the patterned resist in a demolding step, thereby completing the nanostructure transfer.

emphasized the reduction of adhesion through loss of true contact area, while later analyses by Persson and others developed multiscale descriptions linking roughness spectra to effective adhesion and detachment behavior (Persson and Tosatti, 2001; Persson, 2002; Feng et al., 2026). Fractal and self-affine surface descriptions extended this line of inquiry by capturing the hierarchical nature of many engineering and biological interfaces (Wu and Sun, 2023; Liang et al., 2024). At the same time, analytically prescribed geometries, such as sinusoidal wavy surfaces, offered a theoretically more tractable path to understanding the geometric mechanism behind adhesion enhancement or suppression. A landmark result was the study by Guduru (2007), which demonstrated that the contact involving a wavy surface may exhibit a pronounced increase in apparent adhesion during detachment, despite the intuitive expectation that roughness should always weaken the interfacial strength. Subsequent works by Kesari et al. (Kesari et al., 2010; Kesari and Lew, 2011), Ciavarella et al. (Ciavarella, 2016; Papangelo and Ciavarella, 2020; Ciavarella and Papangelo, 2021), and Zhu et al. (2021) further clarified that the effect depends sensitively on profile amplitude, wavelength, and loading path. These findings have generated broad discussion concerning whether roughness weakens adhesion by disrupting conformity or strengthens it by storing elastic energy in a way that resists crack advance. Yet most of these analyses are formulated in an undeformed, linear elastic regime. For soft hyperelastic materials subjected to pre-stretch, the issue is more subtle. Pre-stretch modifies the geometry of a wavy surface, changing its wavelength, amplitude, and curvature in the current configuration. At the same time, it changes the material resistance to normal and tangential perturbations through the tangent stiffness. Thermal loading may further modify the topography, either directly through expansion or indirectly through instability thresholds and thermal modulus variations. Therefore, a model should be developed to investigate the adhesive contact on a wavy surface of pre-stretched and heated soft materials, specifically to determine the role of pre-stretch in modifying the waviness and thereby altering the apparent adhesion.

Beyond prescribed surface topography, soft materials can also generate their own surface morphology through mechanical instability (Mora et al., 2011; Li et al., 2012; Xu et al., 2022), thereby introducing an intrinsically nonlinear route by which contact may be affected. Surface wrinkling, folding, and creasing are now well established as generic responses of soft materials subjected to compression, differential growth, swelling, or thermal mismatch (Lee et al., 2022; Wang et al., 2023, 2024a). Since the bifurcation analyses of compressed elastic half-spaces and the later development of thin film wrinkling theories, instability-driven pattern formation has become a cornerstone at the intersection of mechanics, materials science, and manufacturing (Narayanan et al., 2025). Such spontaneous patterns are not simply mechanical curiosities. They provide practical strategies for generating regular micro and nanoscale features without relying entirely on direct lithographic resolution. This principle underlies a range of self-organized or contact-assisted patterning techniques (Mukherjee and Sharma, 2015), including lithographically induced self-assembly approaches in which applied confinement, local stress concentration, or thermal processing promotes ordered surface structures in soft media. From the standpoint of contact mechanics, however, the appearance of an instability raises a new set of questions. Once a surface has wrinkled or creased, contact with a rigid indenter occurs against a topography that is itself the product of a nonlinear bifurcation process. The resulting profile is generally characterized by the wavelength, amplitude, and residual stress. At the same time, the imposed contact pressure may feed back into the buckling configuration, suppressing certain modes, or causing transitions between distinct post-buckling states. Despite these couplings, many studies of surface instability focus on onset conditions, post-buckling amplitude evolution, or pattern transitions, without carrying the analysis forward to subsequent contact interactions. Hence, a more complete treatment should connect instability analysis to incremental contact mechanics so that the generated morphology is not imposed *a priori* but arises naturally from external loadings.

Despite progress in these individual aspects, the coupling of incremental contact, thermal effects, adhesion, and surface instability is still not well understood from an analytical perspective. The specific gaps are threefold. First, there is no closed-form solution for frictionless thermoelastic contact on a pre-deformed hyperelastic half-space under various thermal boundary conditions. Second, there is a lack of the parametric understanding of how pre-stretch and thermal expansion reshape the oscillatory indentation response involving wavy surfaces. Third, it is necessary to connect the critical conditions for surface instability with the subsequent contact simulation of an indenter acting upon a wavy surface induced by a buckling imperfection. Addressing these interconnected issues would provide a predictive mechanics basis for optimizing the replication fidelity in soft surface patterning technologies.

The article is organized as follows. In Section 2, the incremental governing equations of nonlinear thermoelasticity are derived under a uniform biasing field within the updated Lagrangian framework, and their solutions are reduced to a set of quasi-harmonic functions according to the generalized Almansi's theorem. Section 3 is devoted to the potential theory method for frictionless thermoelastic contact. For a rigid indenter acting on a half-space, explicit expressions for the potentials and their associated densities are derived. Finite element simulations are then performed to validate these theoretical expressions. Section 4 extends the analysis to contact on wavy surfaces. Non-adhesive, adhesive, and viscoelastic adhesive wavy contacts are taken into consideration. A modified JKR model is formulated to incorporate thermal effect, pre-deformation, and surface topography. Envelope functions are constructed to evaluate the oscillation behavior of the incremental indentation response. The conclusions are summarized in Section 5. Of note, the generalized image method is employed in Appendix C to extend the potential theory method to frictionless thermoelastic contact between a rigid indenter and a film-substrate system, where the resulting Fredholm integral equations can be solved iteratively through contraction mappings. Appendix F computationally explores the interplay between surface instability and indentation, where buckling analysis in the total Lagrangian description is used to generate initial imperfections and the augmented Lagrangian method handles the subsequent contact simulation.

2. Basic theory

This section is devoted to establishing the incremental governing equations and presenting their general solutions within the framework of nonlinear thermoelasticity. The definitions of the reference, initial, and current configurations and their mapping relations are provided in Section 2.1. Based on the updated Lagrangian formulation, the general incremental equilibrium equations, constitutive relations, and kinematic equations are derived, and the corresponding objective stress rates are obtained. The incremental governing equations and boundary conditions under a specific biasing field are formulated in Section 2.2. According to the generalized Almansi's theorem, the general solution to the governing equations is given in Section 2.3 in a unified form as a combination of quasi-harmonic functions.

2.1. Nonlinear thermoelasticity and incremental formulations

Consider a compressible hyperelastic body that occupies the domain $\mathcal{B}_r$ in a stress-free reference configuration, with boundary $\partial\mathcal{B}_r$ and outward unit normal vector $\mathbf{N}$. To characterize the material response, a material frame is established in the reference configuration, with basis vectors $\{\boldsymbol{E}^r_\alpha\}(\alpha=1,2,3)$. A material point can then be identified by its position vector $\mathbf{X} := \mathrm{X}_\alpha \boldsymbol{E}^r_\alpha$. The surface and volume elements in this configuration are denoted by $\mathrm{d}\check{\boldsymbol{A}}$ and $\mathrm{d}V$, respectively. When subjected to external loadings, the body deforms to new configurations. Given the objectivity and consistency in the description of a physical process, we may assume that the thermal loadings are applied to the body first, followed by the mechanical counterparts. If a non-uniform spatial variation of the temperature field is present, the body undergoes an incompatible deformation under pure thermal loading and occupies an intermediate domain $\mathcal{B}_\theta$ in a virtual stress-free configuration. To accommodate the deformation mismatch between neighboring material points, an elastic deformation is required to restore compatibility, resulting in a globally compatible configuration denoted $\mathcal{B}^{\mathrm{I}}$. In this configuration, a local frame with basis $\{\boldsymbol{E}^\theta_s\}(s=1,2,3)$ is introduced. Further changes in the elastic field induce additional deformation, bringing the body to the initial configuration $\mathcal{B}^{\mathrm{II}}$, with boundary $\partial\mathcal{B}^{\mathrm{II}}$ and outward unit normal vector $\mathbf{n}$. A space-fixed frame with basis vectors $\{\boldsymbol{e}_i\}(i=1,2,3)$ is adopted in $\mathcal{B}^{\mathrm{II}}$, enabling the representation of a material point by the position vector $\mathbf{x} := \mathrm{x}_i \boldsymbol{e}_i$. The corresponding surface and volume elements are denoted by $\mathrm{d}\check{\boldsymbol{a}}$ and $\mathrm{d}v$, respectively.

The deformation of the hyperelastic body from $\mathcal{B}_r$ to $\mathcal{B}^{\mathrm{II}}$ is described by the material point mapping $\chi : \mathbf{X} \mapsto \mathbf{x}$. The deformation gradient is given by $\mathbf{F} = \mathrm{Grad}\chi$, where Grad denotes the gradient operator defined in the reference configuration. A multiplicative decomposition of the deformation gradient into thermal and elastic parts is expressed as $\mathbf{F} = \mathbf{F}_e\mathbf{F}_\theta$, in which $\mathbf{F}_\theta = \left[\mathrm{F}_\theta\right]_{s\alpha}\boldsymbol{E}^\theta_s \otimes \boldsymbol{E}^r_\alpha$ represents the deformation gradient from $\mathcal{B}_r$ to $\mathcal{B}_\theta$, and $\mathbf{F}_e = \left[\mathrm{F}_e\right]_{is}\boldsymbol{e}_i \otimes \boldsymbol{E}^\theta_s$ denotes the deformation gradient from $\mathcal{B}_\theta$ to $\mathcal{B}^{\mathrm{II}}$. Here, $\otimes$ is the tensor product. The deformation gradients from $\mathcal{B}_\theta$ to $\mathcal{B}^{\mathrm{I}}$ and from $\mathcal{B}^{\mathrm{I}}$ to $\mathcal{B}^{\mathrm{II}}$ are denoted $\mathbf{F}^{\mathrm{I}}_e$ and $\mathbf{F}^{\mathrm{II}}_e$, respectively, satisfying $\mathbf{F}_e = \mathbf{F}^{\mathrm{II}}_e\mathbf{F}^{\mathrm{I}}_e$. The mappings between these configurations are depicted in Fig. 2. The left and right Cauchy-Green deformation tensors are respectively defined as $\mathbf{b} = \mathbf{F}\mathbf{F}^{\mathrm{T}}$ and $\mathbf{C} = \mathbf{F}^{\mathrm{T}}\mathbf{F}$. Surface and volume elements in the initial and reference configurations are related via Nanson's formula $\mathrm{d}\check{\boldsymbol{a}} = \mathbf{n}\mathrm{d}\check{a} = J\mathbf{F}^{-\mathrm{T}}\mathbf{N}\mathrm{d}\check{A}$ and $\mathrm{d}v = J\mathrm{d}V$, respectively, where $J = \det\mathbf{F}$ is the volume ratio.

If we neglect body forces, the equilibrium equation is given by $\mathrm{Div}\mathbf{T} = \mathbf{0}$, where $\mathbf{T} = J\mathbf{F}^{-1}\boldsymbol{\tau}$ denotes the nominal stress tensor and Div represents the divergence operator defined on the reference configuration $\mathcal{B}_r$. The boundary condition on $\partial\mathcal{B}^{\mathrm{II}}$ is specified as $\boldsymbol{\tau}\mathbf{n} = \mathbf{t}_a$, with $\mathbf{t}_a$ being the surface traction. By introducing an energy density function $\Omega(\mathbf{F}_e)$ per unit reference volume, the nonlinear constitutive equation is established as $\mathbf{T}_e = \partial\Omega/\partial\mathbf{F}_e$. When $\Omega(\mathbf{F}_e)$ is formulated as a function of invariants, the nonlinear constitutive equations can be further expressed as $\mathbf{T}_e = \sum_{m=1}^{3}\Omega_m\partial\mathcal{I}_m/\partial\mathbf{F}_e$, where $\Omega_m := \partial\Omega/\partial\mathcal{I}_m$ for $m=1,2,3$. The invariants are $\mathcal{I}_1 = \mathrm{tr}\,\mathbf{C}_e$, $\mathcal{I}_2 = [(\mathrm{tr}\,\mathbf{C}_e)^2 - \mathrm{tr}\,\mathbf{C}_e^2]/2$, and $\mathcal{I}_3 = \det\mathbf{C}_e$. Then, $\mathbf{T} = J_\theta\mathbf{F}_\theta^{-1}\mathbf{T}_e = J_\theta\mathbf{F}_\theta^{-1}\partial\Omega/\partial\mathbf{F}_e$ is derived via mappings across configurations, where $J_\theta = \det\mathbf{F}_\theta$. Consequently, the Cauchy stress tensor $\boldsymbol{\tau}$ takes the form

$$\begin{aligned}\boldsymbol{\tau} &= J^{-1}\mathbf{F}\mathbf{T} = (J_eJ_\theta)^{-1}(\mathbf{F}_e\mathbf{F}_\theta)\left(J_\theta\mathbf{F}_\theta^{-1}\frac{\partial\Omega}{\partial\mathbf{F}_e}\right) = J_e^{-1}\mathbf{F}_e\frac{\partial\Omega}{\partial\mathbf{F}_e}\\ &= 2J_e^{-1}[\Omega_1\mathbf{b}_e + \Omega_2(\mathcal{I}_1\mathbf{b}_e - \mathbf{b}_e^2) + \mathcal{I}_3\Omega_3\mathbb{I}],\end{aligned} \tag{1}$$

with $J_e = \det\mathbf{F}_e$ and $\mathbf{F}_\theta = \overline{\mathscr{I}} + \boldsymbol{\kappa}(\Theta - \Theta_{\mathrm{ref}})$, where $\mathbb{I} = \delta_{ij}\boldsymbol{e}_i \otimes \boldsymbol{e}_j$ and $\overline{\mathscr{I}} = \delta_{a\alpha}\boldsymbol{E}^\theta_a \otimes \boldsymbol{E}^r_\alpha$ are identity tensors, δ_{ij} and $\delta_{a\alpha}$ are both Kronecker delta; $\boldsymbol{\kappa}$ is the coefficient of thermal expansion; Θ and Θ_{ref} are temperature and its reference counterpart, respectively.

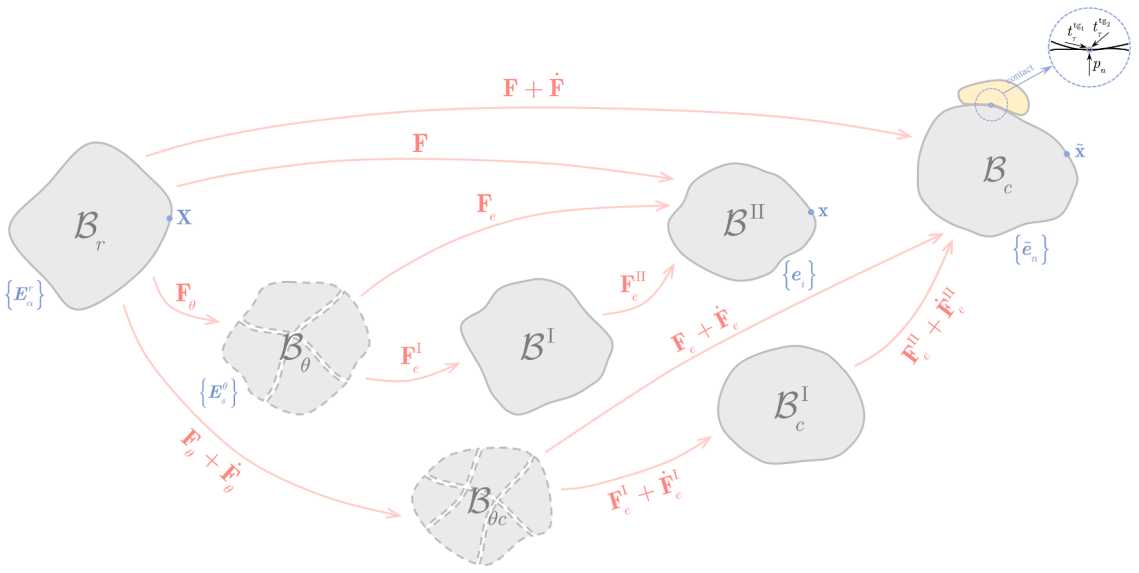


Fig. 2. Relations among different configurations. The dashed enclosure highlights the virtual stress free configuration. The deformable domain is shown in gray, and the rigid domain representing the indenter is shown in yellow. During contact, p_n denotes the normal contact force, and $t_\tau^{\mathrm{tg}_1}$ together with $t_\tau^{\mathrm{tg}_2}$ represent the tangential forces along the two orthogonal horizontal directions.

When the additional elastic field induced by applied load and displacement is significantly smaller than the biasing field, an infinitesimal incremental perturbation is superimposed on the initial configuration $\mathcal{B}^{\mathrm{II}}$, resulting in the current configuration $\mathcal{B}_c$. In this configuration, a frame with basis $\{\tilde{\boldsymbol{e}}_n\}(n=1,2,3)$ is introduced, so that the material point can be described by the position vector $\tilde{\mathbf{x}} := \tilde{\mathrm{x}}_n \tilde{\boldsymbol{e}}_n$. Owing to the infinitesimal nature of the perturbation, the displacement from $\mathcal{B}^{\mathrm{II}}$ to $\mathcal{B}_c$ is denoted by $\dot{\mathbf{x}}(\mathbf{X})$, satisfying $\widetilde{\mathscr{I}}^{\mathrm{T}}\tilde{\mathbf{x}} = \mathbf{x} + \dot{\mathbf{x}}$, where $\widetilde{\mathscr{I}} = \delta_{ni}\tilde{\boldsymbol{e}}_n \otimes \boldsymbol{e}_i$. For convenience, the incremental deformation $\dot{\mathbf{x}}$ is also frequently written as $\mathbf{u}$. Hence, we may define the displacement gradient tensor as $\mathbf{L} := \left(\widetilde{\mathscr{I}}^{\mathrm{T}}\tilde{\mathbf{F}} - \mathbf{F}\right)\mathbf{F}^{-1} = \dot{\mathbf{F}}\mathbf{F}^{-1} = \operatorname{grad}\mathbf{u} = \mathbf{L}_e + \mathbf{F}_e\mathbf{L}_\theta\mathbf{F}_e^{-1}$, where $\mathbf{L}_e := \dot{\mathbf{F}}_e\mathbf{F}_e^{-1}$ and $\mathbf{L}_\theta := \dot{\mathbf{F}}_\theta\mathbf{F}_\theta^{-1}$. Of note, $\widetilde{\mathscr{I}}$ is a two-point identity tensor employed for basis transform across configurations. It will be omitted hereafter unless necessary for clarity.

Incremental fields of other physical quantities are likewise indicated by the overdots. Based on the incremental relation for the nominal stress tensor

$$\begin{aligned}\tilde{\mathbf{T}} = \mathbf{T} + \dot{\mathbf{T}} &= (J_\theta + \dot{J}_\theta)(\mathbf{F}_\theta + \dot{\mathbf{F}}_\theta)^{-1}(\mathbf{T}_e + \dot{\mathbf{T}}_e)\\ &\simeq (J_\theta + \dot{J}_\theta)(\mathbf{F}_\theta^{-1} - \mathbf{F}_\theta^{-1}\dot{\mathbf{F}}_\theta\mathbf{F}_\theta^{-1})(\mathbf{T}_e + \dot{\mathbf{T}}_e)\\ &= J_\theta\mathbf{F}_\theta^{-1}\mathbf{T}_e + J_\theta\mathbf{F}_\theta^{-1}\dot{\mathbf{T}}_e + \dot{J}_\theta\mathbf{F}_\theta^{-1}\mathbf{T}_e - J_\theta\mathbf{F}_\theta^{-1}\dot{\mathbf{F}}_\theta\mathbf{F}_\theta^{-1}\mathbf{T}_e,\end{aligned} \tag{2}$$

with $\dot{J}_\theta = \tilde{J}_\theta - J_\theta = \det(\mathbf{F}_\theta + \dot{\mathbf{F}}_\theta) - \det(\mathbf{F}_\theta)$ and $\dot{\mathbf{F}}_\theta = \boldsymbol{\kappa}\dot{\Theta}$, the incremental equilibrium equation in Eulerian form can be formulated as $\operatorname{div}\dot{\mathbf{T}}_0 = \mathbf{0}$, where $\dot{\mathbf{T}}_0 = J^{-1}\mathbf{F}\dot{\mathbf{T}}$ represents the push-forward version of the incremental nominal stress tensor. Hence, the corresponding objective stress rate yields

$$\begin{aligned}\overset{\star}{\mathbf{T}}_0 &= (J_eJ_\theta)^{-1}(\mathbf{F}_e\mathbf{F}_\theta)\overset{\star}{\mathbf{T}} = J_e^{-1}J_\theta^{-1}\mathbf{F}_e\mathbf{F}_\theta\dot{\mathbf{S}}\mathbf{F}^{\mathrm{T}}\\ &= J_e^{-1}J_\theta^{-1}\mathbf{F}_e\mathbf{F}_\theta\left[\dot{\overline{(J_eJ_\theta\mathbf{F}_\theta^{-1}\mathbf{F}_e^{-1}\boldsymbol{\tau})}} - \mathbf{T}\mathbf{L}_e^{\mathrm{T}} - \mathbf{T}\mathbf{F}_e^{-\mathrm{T}}\mathbf{L}_\theta^{\mathrm{T}}\mathbf{F}_e^{\mathrm{T}}\right]\\ &= \dot{\boldsymbol{\tau}} - \mathbf{L}_e\boldsymbol{\tau} - \boldsymbol{\tau}\mathbf{L}_e^{\mathrm{T}} - \mathbf{F}_e\mathbf{L}_\theta\mathbf{F}_e^{-1}\boldsymbol{\tau} - \boldsymbol{\tau}\mathbf{F}_e^{-\mathrm{T}}\mathbf{L}_\theta^{\mathrm{T}}\mathbf{F}_e^{\mathrm{T}} + \operatorname{tr}(\mathbf{L}_e)\boldsymbol{\tau} + \operatorname{tr}(\mathbf{L}_\theta)\boldsymbol{\tau},\end{aligned} \tag{3}$$

where $\dot{\mathbf{S}}$ is the incremental second Piola-Kirchhoff stress tensor, $\dot{\mathbf{F}}^{-1} = -\mathbf{F}^{-1}\dot{\mathbf{F}}\mathbf{F}^{-1}$ and $\dot{J} = J\mathbf{F}^{-1}\cdot\cdot\dot{\mathbf{F}} = J\operatorname{tr}(\mathbf{L})$ are utilized to simplify Eq. (3). Here, the double inner product follows $\boldsymbol{\Xi}_1\cdot\cdot\boldsymbol{\Xi}_2 = [\Xi_1]_{ij}[\Xi_2]_{ji}$. The incremental boundary condition is established as $\dot{\mathbf{T}}_0^{\mathrm{T}}\mathbf{n} = \dot{\mathbf{t}}_a$, where $\dot{\mathbf{t}}_a$ is the incremental surface traction satisfying $\dot{\mathbf{t}}_a\mathrm{d}a = \dot{\mathbf{t}}_A\mathrm{d}A$. According to Eq. (2), the incremental constitutive equation is derived as

$$\begin{aligned}\dot{\mathbf{T}}_0 &= (J_eJ_\theta)^{-1}(\mathbf{F}_e\mathbf{F}_\theta)\left(J_\theta\mathbf{F}_\theta^{-1}\frac{\partial^2\Omega}{\partial\mathbf{F}_e\partial\mathbf{F}_e}\cdot\cdot\dot{\mathbf{F}}_e + \dot{J}_\theta\mathbf{F}_\theta^{-1}\mathbf{T}_e - J_\theta\mathbf{F}_\theta^{-1}\dot{\mathbf{F}}_\theta\mathbf{F}_\theta^{-1}\mathbf{T}_e\right)\\ &= J_e^{-1}\mathbf{F}_e\frac{\partial^2\Omega}{\partial\mathbf{F}_e\partial\mathbf{F}_e}\cdot\cdot[(\mathbf{L} - \mathbf{F}_e\mathbf{L}_\theta\mathbf{F}_e^{-1})\mathbf{F}_e] + J_e^{-1}\operatorname{tr}(\mathbf{L}_\theta)\mathbf{F}_e\frac{\partial\Omega}{\partial\mathbf{F}_e} - J_e^{-1}\mathbf{F}_e\mathbf{L}_\theta\frac{\partial\Omega}{\partial\mathbf{F}_e}\\ &= J_e^{-1}\mathbf{F}_e\frac{\partial^2\Omega}{\partial\mathbf{F}_e\partial\mathbf{F}_e}\circ_2^{\mathrm{T}}\mathbf{F}_e^{\mathrm{T}}\cdot\cdot\mathbf{L} - J_e^{-1}\mathbf{F}_e\frac{\partial^2\Omega}{\partial\mathbf{F}_e\partial\mathbf{F}_e}\cdot\cdot(\mathbf{F}_e\mathbf{L}_\theta) + J_e^{-1}\mathbf{F}_e[\operatorname{tr}(\mathbf{L}_\theta)\bar{\mathbb{I}} - \mathbf{L}_\theta]\frac{\partial\Omega}{\partial\mathbf{F}_e}\\ &:= \mathbf{A}_0\cdot\cdot\mathbf{L} - \mathbf{M}_0\dot{\Theta},\end{aligned} \tag{4}$$

where $\bar{\mathbb{I}} = \delta_{ab}\boldsymbol{E}_a^\theta \otimes \boldsymbol{E}_b^\theta$ and the product "$\underset{2}{\circ}$" follows $\boldsymbol{\Xi}_3 \underset{2}{\circ} \boldsymbol{\Xi}_4 = [\Xi_3]_{\alpha i \beta j}[\Xi_4]_{k\beta}\boldsymbol{E}_\alpha^r \otimes \boldsymbol{e}_i \otimes \boldsymbol{e}_k \otimes \boldsymbol{e}_j$. The components of $\mathbf{A}_0$ and $\mathbf{M}_0$ are expressed as

$$\begin{aligned}
\mathrm{A}_{0jigk} &= J_e^{-1}\left[\mathrm{F}_e\right]_{ja}\left[\mathrm{F}_e\right]_{gb}\left(\sum_{m=1}^{3}\sum_{n=1}^{3}\Omega_{mn}\frac{\partial \mathcal{I}_m}{\partial\left[\mathrm{F}_e\right]_{ia}}\frac{\partial \mathcal{I}_n}{\partial\left[\mathrm{F}_e\right]_{kb}} + \sum_{m=1}^{3}\Omega_m\frac{\partial^2 \mathcal{I}_m}{\partial\left[\mathrm{F}_e\right]_{ia}\partial\left[\mathrm{F}_e\right]_{kb}}\right) = \mathrm{A}_{0gkji}, \\
\mathrm{M}_{0ji} &= J_e^{-1}\left[\mathrm{F}_e\right]_{ja}\left[\mathrm{F}_e\right]_{kc}\kappa_{c\alpha}\left[\mathrm{F}_\theta^{-1}\right]_{\alpha b}\left(\sum_{m=1}^{3}\sum_{n=1}^{3}\Omega_{mn}\frac{\partial \mathcal{I}_m}{\partial\left[\mathrm{F}_e\right]_{ia}}\frac{\partial \mathcal{I}_n}{\partial\left[\mathrm{F}_e\right]_{kb}} + \sum_{m=1}^{3}\Omega_m\frac{\partial^2 \mathcal{I}_m}{\partial\left[\mathrm{F}_e\right]_{ia}\partial\left[\mathrm{F}_e\right]_{kb}}\right) \\
&\quad + J_e^{-1}\left[\mathrm{F}_e\right]_{ja}\left(\kappa_{a\alpha}\left[\mathrm{F}_\theta^{-1}\right]_{\alpha b} - \kappa_{c\alpha}\left[\mathrm{F}_\theta^{-1}\right]_{\alpha c}\delta_{ab}\right)\left(\sum_{m=1}^{3}\Omega_m\frac{\partial \mathcal{I}_m}{\partial\left[\mathrm{F}_e\right]_{ib}}\right),
\end{aligned} \tag{5}$$

respectively, where $\Omega_{mn} := \partial^2\Omega/(\partial \mathcal{I}_m \partial \mathcal{I}_n)$, and the elements of instantaneous material tensors A_{0jigk} and M_{0jk} $(i, j, k, g = 1, 2, 3)$ are presented in Appendix A.

2.2. Governing equations

The governing equations for a hyperelastic body subjected to biasing fields are established in this section. We apply a uniform equi-biaxial pre-stretch λ_1 to the hyperelastic material in the $x - y$ plane, while ensuring that it remains stress-free in the z-direction. Hence, the pre-deformation is described via the deformation gradient $\mathbf{F} = \mathrm{diag}(\lambda_1, \lambda_1, \lambda_3)$, where λ_3 can be represented in terms of λ_1 according to the stress-free boundary conditions at $z = 0$. The coefficient of thermal expansion is assumed to be deformation-independent and transversely isotropic as $\boldsymbol{\kappa} = \mathrm{diag}(\kappa_1, \kappa_1, \kappa_3)$. Besides, the thermal responses of the other materials are assumed negligible, such that these materials are treated as temperature-independent.

If we substitute the specific forms of $\mathbf{F}$ and $\boldsymbol{\kappa}$ mentioned above into Eq. (4) and then into the incremental equilibrium equation, the governing equations can be derived as

$$\begin{aligned}
&\left(\mathrm{A}_{01111}\frac{\partial^2 u_x}{\partial x^2} + \mathrm{A}_{01212}\frac{\partial^2 u_x}{\partial y^2} + \mathrm{A}_{03131}\frac{\partial^2 u_x}{\partial z^2}\right) + \left(\mathrm{A}_{01122} + \mathrm{A}_{01221}\right)\frac{\partial^2 u_y}{\partial x \partial y} + \left(\mathrm{A}_{01133} + \mathrm{A}_{01331}\right)\frac{\partial^2 u_z}{\partial x \partial z} - \mathrm{M}_{011}\frac{\partial \dot{\Theta}}{\partial x} = 0, \\
&\left(\mathrm{A}_{01221} + \mathrm{A}_{01122}\right)\frac{\partial^2 u_x}{\partial x \partial y} + \left(\mathrm{A}_{01212}\frac{\partial^2 u_y}{\partial x^2} + \mathrm{A}_{01111}\frac{\partial^2 u_y}{\partial y^2} + \mathrm{A}_{03131}\frac{\partial^2 u_y}{\partial z^2}\right) + \left(\mathrm{A}_{01133} + \mathrm{A}_{01331}\right)\frac{\partial^2 u_z}{\partial y \partial z} - \mathrm{M}_{011}\frac{\partial \dot{\Theta}}{\partial y} = 0, \\
&\left(\mathrm{A}_{01331} + \mathrm{A}_{01133}\right)\frac{\partial^2 u_x}{\partial x \partial z} + \left(\mathrm{A}_{01331} + \mathrm{A}_{01133}\right)\frac{\partial^2 u_y}{\partial y \partial z} + \left[\mathrm{A}_{01313}\Delta u_z + \mathrm{A}_{03333}\frac{\partial^2 u_z}{\partial z^2}\right] - \mathrm{M}_{033}\frac{\partial \dot{\Theta}}{\partial z} = 0,
\end{aligned} \tag{6}$$

where $\Delta := \partial^2/\partial x^2 + \partial^2/\partial y^2$ is the two-dimensional Laplacian. To rewrite Eq. (6) in a compact form, Φ_0 and Ψ_0 are introduced such that $u_x = \partial\Psi_0/\partial y - \partial\Phi_0/\partial x$ and $u_y = -\partial\Psi_0/\partial x - \partial\Phi_0/\partial y$. Thus, the governing equations are organized in terms of Ψ_0, Φ_0, u_z, and $\dot{\Theta}$ as

$$\left(\mathrm{A}_{01212}\Delta + \mathrm{A}_{03131}\frac{\partial^2}{\partial z^2}\right)\Psi_0 = 0, \tag{7}$$

$$\mathfrak{D}\begin{Bmatrix}\Phi_0 \\ u_z \\ \dot{\Theta}\end{Bmatrix} = \begin{bmatrix} \mathrm{A}_{01111}\Delta + \mathrm{A}_{03131}\frac{\partial^2}{\partial z^2} & -\left(\mathrm{A}_{01133} + \mathrm{A}_{01331}\right)\frac{\partial}{\partial z} & \mathrm{M}_{011} \\ -\left(\mathrm{A}_{01133} + \mathrm{A}_{01331}\right)\Delta\frac{\partial}{\partial z} & \mathrm{A}_{01313}\Delta + \mathrm{A}_{03333}\frac{\partial^2}{\partial z^2} & -\mathrm{M}_{033}\frac{\partial}{\partial z} \\ 0 & 0 & k_{11}\Delta + k_{33}\frac{\partial^2}{\partial z^2} \end{bmatrix}\begin{Bmatrix}\Phi_0 \\ u_z \\ \dot{\Theta}\end{Bmatrix} = \mathbf{0}, \tag{8}$$

where $\mathrm{A}_{01111} - \mathrm{A}_{01122} = \mathrm{A}_{01221} + \mathrm{A}_{01212}$ is adopted here.

2.3. General solutions

We assume that the solution to Eq. (8) takes the form

$$\begin{Bmatrix}\Phi_0 \\ u_z \\ \dot{\Theta}\end{Bmatrix} = \mathfrak{D}^\dagger\boldsymbol{\xi} = \begin{bmatrix} \mathfrak{D}_{11}^\dagger & \mathfrak{D}_{21}^\dagger & \mathfrak{D}_{31}^\dagger \\ \mathfrak{D}_{12}^\dagger & \mathfrak{D}_{22}^\dagger & \mathfrak{D}_{32}^\dagger \\ \mathfrak{D}_{13}^\dagger & \mathfrak{D}_{23}^\dagger & \mathfrak{D}_{33}^\dagger \end{bmatrix}\begin{Bmatrix}\xi^{(1)} \\ \xi^{(2)} \\ \xi^{(3)}\end{Bmatrix}, \tag{9}$$

where $\mathfrak{D}^\dagger$ is the adjugate of the operator matrix $\mathfrak{D}$, and its (i, j)-th entry is the cofactor of $\mathfrak{D}$. $\boldsymbol{\xi} = [\xi^{(1)}, \xi^{(2)}, \xi^{(3)}]^{\mathrm{T}}$ is governed by

$$\mathfrak{D}\mathfrak{D}^\dagger\boldsymbol{\xi} = (\det\mathfrak{D})\boldsymbol{\xi} = \left(\hbar_0\frac{\partial^4}{\partial z^4} + \hbar_1\Delta\frac{\partial^2}{\partial z^2} + \hbar_2\Delta^2\right)\left(k_{11}\Delta + k_{33}\frac{\partial^2}{\partial z^2}\right)\boldsymbol{\xi} = \mathbf{0}, \tag{10}$$

where $\hbar_0 = \mathrm{A}_{03131}\mathrm{A}_{03333}$, $\hbar_1 = \mathrm{A}_{01111}\mathrm{A}_{03333} + \mathrm{A}_{03131}\mathrm{A}_{01313} - \left(\mathrm{A}_{01133}\mathrm{A}_{01331}\right)^2$, and $\hbar_2 = \mathrm{A}_{01111}\mathrm{A}_{01313}$. In view of the fact that $\xi^{(i)}(i = 1, 2, 3)$ are not independent, it suffices to retain only $\xi^{(3)}$. Based on the generalized Almansi's theorem (Ding et al., 1996), the solutions to

Eq. (10) fall into three categories depending on the nature of the roots of the algebraic equation, such that

$$\begin{cases} \xi^{(3)} = \xi_1^{(3)} + \xi_2^{(3)} + \xi_3^{(3)}, & (\text{when } s_1^2 \neq s_2^2 \neq s_3^2 \neq s_1^2) \\ \xi^{(3)} = \xi_1^{(3)} + \xi_2^{(3)} + z\xi_3^{(3)}, & (\text{when } s_1^2 \neq s_2^2 = s_3^2) \\ \xi^{(3)} = \xi_1^{(3)} + z\xi_2^{(3)} + z^2\xi_3^{(3)}, & (\text{when } s_1^2 = s_2^2 = s_3^2) \end{cases} \tag{11}$$

where $\xi_k^{(3)}(k=1,2,3)$ are governed by $\left(\Delta + \frac{\partial^2}{\partial z_k^2}\right)\xi_k^{(3)} = 0 (k=1,2,3)$, with $z_k^2 = s_k^2 z^2 (k=1,2,3)$, whereby $s_k^2 (k=1,2)$ are the roots of the biquadratic equation $\hbar_0 s^4 - \hbar_1 s^2 + \hbar_2 = 0$ and $s_3^2 = k_{11}/k_{33}$. It warrants noting that imaginary roots may arise when excessive pre-deformation is applied to the hyperelastic body, indicating the onset of instability. We assume that there are three distinct real roots (i.e., the first case in Eq. (11)), so that Φ_0, u_z, and $\dot{\Theta}$ are established in terms of novel functions $\Psi_k (k=1,2,3)$ as

$$\begin{aligned} \Phi_0 &= \mathfrak{D}_{31}^{\dagger}\xi^{(3)} = \left\{ -\mathrm{M}_{011}\mathrm{A}_{01313}\Delta + \left[\mathrm{M}_{033}\left(\mathrm{A}_{01133} + \mathrm{A}_{01331}\right) - \mathrm{M}_{011}\mathrm{A}_{03333}\right]\frac{\partial^2}{\partial z^2} \right\} \sum_{k=1}^{3} \xi_k^{(3)} \\ &= \sum_{k=1}^{3} \left\{ \left[\mathrm{M}_{033}\left(\mathrm{A}_{01133} + \mathrm{A}_{01331}\right) - \mathrm{M}_{011}\mathrm{A}_{03333}\right]s_k^2 + \mathrm{M}_{011}\mathrm{A}_{01313} \right\} \frac{\partial^2 \xi_k^{(3)}}{\partial z_k^2} := \sum_{k=1}^{3} \Psi_k, \\ u_z &= \mathfrak{D}_{32}^{\dagger}\xi^{(3)} = \left\{ \left[\mathrm{M}_{033}\mathrm{A}_{01111} - \mathrm{M}_{011}\left(\mathrm{A}_{01133} + \mathrm{A}_{01331}\right)\right]\Delta + \mathrm{M}_{033}\mathrm{A}_{03131}\frac{\partial^2}{\partial z^2} \right\} \sum_{k=1}^{3} \frac{\partial \xi_k^{(3)}}{\partial z} \\ &= \sum_{k=1}^{3} \left[\mathrm{M}_{011}\left(\mathrm{A}_{01133} + \mathrm{A}_{01331}\right) - \mathrm{M}_{033}\mathrm{A}_{01111} + \mathrm{M}_{033}\mathrm{A}_{03131}s_k^2\right] s_k \frac{\partial^3 \xi^{(3)}}{\partial z_k^3} := \sum_{k=1}^{3} \alpha_k \frac{\partial \Psi_k}{\partial z_k}, \\ \dot{\Theta} &= \mathfrak{D}_{33}^{\dagger}\xi^{(3)} = \left\{ \mathrm{A}_{01111}\mathrm{A}_{01313}\Delta^2 + \left[\mathrm{A}_{01111}\mathrm{A}_{03333} + \mathrm{A}_{03131}\mathrm{A}_{01313} - \left(\mathrm{A}_{01133} + \mathrm{A}_{01331}\right)^2\right]\Delta \frac{\partial^2}{\partial z^2} + \mathrm{A}_{03131}\mathrm{A}_{03333}\frac{\partial^4}{\partial z^4} \right\} \sum_{k=1}^{3} \xi_k^{(3)} \\ &= \sum_{k=1}^{3} \left\{ \mathrm{A}_{01111}\mathrm{A}_{01313} - \left[\mathrm{A}_{01111}\mathrm{A}_{03333} + \mathrm{A}_{03131}\mathrm{A}_{01313} - \left(\mathrm{A}_{01133} + \mathrm{A}_{01331}\right)^2\right]s_k^2 + \mathrm{A}_{03131}\mathrm{A}_{03333}s_k^4 \right\} \frac{\partial^4 \xi_k^{(3)}}{\partial z_k^4} := \sum_{k=1}^{3} \beta_k \frac{\partial^2 \Psi_k}{\partial z_k^2}, \end{aligned} \tag{12}$$

where α_k and $\beta_k (k=1,2,3)$ are presented in Appendix A. From the definitions given in Eq. (12) together with Eq. (7), Ψ_k satisfy $\left(\Delta + \frac{\partial^2}{\partial z_k^2}\right)\Psi_k = 0 (k=0,1,2,3)$, where $s_0^2 = \mathrm{A}_{01212}/\mathrm{A}_{03131}$.

In the Cartesian coordinate system (x, y, z), the general solution for the displacement components and incremental temperature is given by

$$u_x = \frac{\partial \Psi_0}{\partial y} - \sum_{k=1}^{3} \frac{\partial \Psi_k}{\partial x}, \quad u_y = -\frac{\partial \Psi_0}{\partial x} - \sum_{k=1}^{3} \frac{\partial \Psi_k}{\partial y}, \quad u_z = \sum_{k=1}^{3} \alpha_k \frac{\partial \Psi_k}{\partial z_k}, \quad \dot{\Theta} = \sum_{k=1}^{3} \beta_k \frac{\partial^2 \Psi_k}{\partial z_k^2}. \tag{13}$$

For the convenience of later analysis, this solution is reformulated in the cylindrical coordinate system (ρ, ϕ, z) as

$$u_\rho = \frac{1}{\rho}\frac{\partial \Psi_0}{\partial \phi} - \sum_{k=1}^{3} \frac{\partial \Psi_k}{\partial \rho}, \qquad u_\phi = -\frac{\partial \Psi_0}{\partial \rho} - \frac{1}{\rho}\sum_{k=1}^{3} \frac{\partial \Psi_k}{\partial \phi}, \qquad u_z = \sum_{k=1}^{3} \alpha_k \frac{\partial \Psi_k}{\partial z_k} := w_1, \qquad \dot{\Theta} = \sum_{k=1}^{3} \beta_k \frac{\partial^2 \Psi_k}{\partial z_k^2} := \sigma_{z2}. \tag{14}$$

Consequently, the incremental stress components are accordingly obtained as

$$\begin{aligned} \dot{\mathrm{T}}_{0zz} &= \sum_{k=1}^{3} \left(\mathrm{A}_{01133} + \mathrm{A}_{03333}\alpha_k s_k - \mathrm{M}_{033}\beta_k\right)\frac{\partial^2 \Psi_k}{\partial z_k^2} := \sigma_{z1}, \\ \dot{\mathrm{T}}_{0\rho\rho} + \dot{\mathrm{T}}_{0\phi\phi} &= \sum_{k=1}^{3} \left[\left(\mathrm{A}_{01111} + \mathrm{A}_{01122}\right) + 2\mathrm{A}_{01133}\alpha_k s_k - 2\mathrm{M}_{011}\beta_k\right]\frac{\partial^2 \Psi_k}{\partial z_k^2} := \sigma_{z3}, \\ \dot{\mathrm{T}}_{0\rho\rho} - \dot{\mathrm{T}}_{0\phi\phi} &= \left(\mathrm{A}_{01111} - \mathrm{A}_{01122}\right)\left[\frac{2}{\rho}\left(\frac{\partial^2 \Psi_0}{\partial \rho \partial \phi} - \frac{1}{\rho}\frac{\partial \Psi_0}{\partial \phi}\right) + \sum_{k=1}^{3}\left(-\frac{\partial^2 \Psi_k}{\partial \rho^2} + \frac{1}{\rho}\frac{\partial \Psi_k}{\partial \rho} + \frac{1}{\rho^2}\frac{\partial^2 \Psi_k}{\partial \phi^2}\right)\right] := \sigma_{\rho t}, \\ \dot{\mathrm{T}}_{0\rho\phi} + \dot{\mathrm{T}}_{0\phi\rho} &= \left(\mathrm{A}_{01221} + \mathrm{A}_{01212}\right)\left[\left(-\frac{\partial^2 \Psi_0}{\partial \rho^2} + \frac{1}{\rho}\frac{\partial \Psi_0}{\partial \rho} + \frac{1}{\rho^2}\frac{\partial^2 \Psi_0}{\partial \phi^2}\right) + \sum_{k=1}^{3}\frac{2}{\rho}\left(\frac{1}{\rho}\frac{\partial \Psi_k}{\partial \phi} - \frac{\partial^2 \Psi_k}{\partial \rho \partial \phi}\right)\right] := \sigma_{\phi t}, \\ \dot{\mathrm{T}}_{0\rho\phi} - \dot{\mathrm{T}}_{0\phi\rho} &= \left(\mathrm{A}_{01221} - \mathrm{A}_{01212}\right)\Delta\Psi_0 := \sigma_{zt}, \\ \dot{\mathrm{T}}_{0z\rho} &= \mathrm{A}_{03131}\frac{1}{\rho}\frac{\partial^2 \Psi_0}{\partial \phi \partial z} + \sum_{k=1}^{3}\left(-\mathrm{A}_{03131}s_k + \mathrm{A}_{01331}\alpha_k\right)\frac{\partial^2 \Psi_k}{\partial \rho \partial z_k} := \sigma_{\rho 1}, \\ \dot{\mathrm{T}}_{0\rho z} &= \mathrm{A}_{01331}\frac{1}{\rho}\frac{\partial^2 \Psi_0}{\partial \phi \partial z} + \sum_{k=1}^{3}\left(-\mathrm{A}_{01331}s_k + \mathrm{A}_{01313}\alpha_k\right)\frac{\partial^2 \Psi_k}{\partial \rho \partial z_k} := \sigma_{\rho 2}, \\ \dot{\mathrm{T}}_{0z\phi} &= -\mathrm{A}_{03131}\frac{\partial^2 \Psi_0}{\partial \rho \partial z} + \sum_{k=1}^{3}\left(-\mathrm{A}_{03131}s_k + \mathrm{A}_{01331}\alpha_k\right)\frac{1}{\rho}\frac{\partial^2 \Psi_k}{\partial \phi \partial z_k} := \sigma_{\phi 1}, \end{aligned} \tag{15}$$

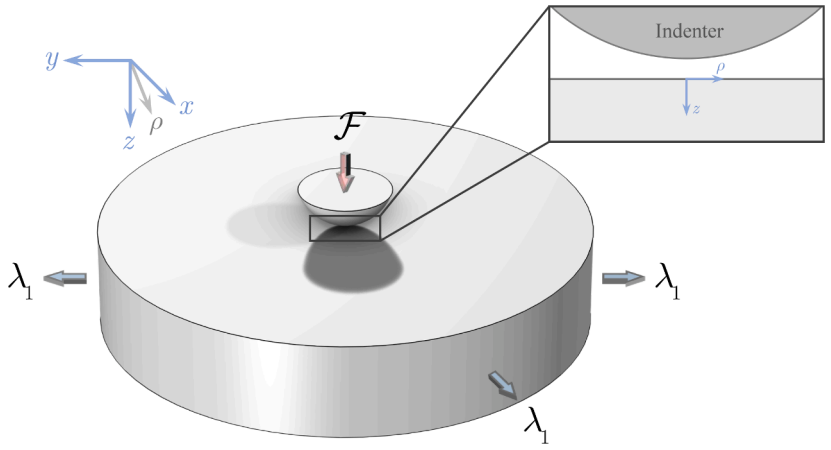


Fig. 3. Schematic diagram of contact between a rigid indenter and a pre-deformed hyperelastic half-space.

$$\dot{\mathrm{T}}_{0\phi z} = -\mathrm{A}_{01331}\frac{\partial^2\Psi_0}{\partial\rho\partial z} + \sum_{k=1}^{3}\left(-\mathrm{A}_{01331}s_k + \mathrm{A}_{01313}\alpha_k\right)\frac{1}{\rho}\frac{\partial^2\Psi_k}{\partial\phi\partial z_k} := \sigma_{\phi 2}.$$

3. Contact solution for an indenter with a prescribed heat flux

Analytical solutions to the contact problems under various boundary conditions are derived herein via the potential theory method. Here, we analyze the thermoelastic contact between a rigid indenter and a hyperelastic half-space. Single-layer potentials are established, and their densities are solved explicitly. The analytical solutions derived from those potentials are then validated via finite element simulations. Besides, we examine the contact behavior of a hyperelastic film on a smooth substrate according to the generalized image method in Appendix C. Contraction mappings are formulated, and the densities are subsequently approximated through iteration.

Consider a rigid conducting indenter in frictionless and adhesionless thermoelastic contact with the surface of a hyperelastic half-space, as illustrated in Fig. 3. The indenter profile is described by a C^1-continuous function $f(\rho,\phi)$. Within the contact area S, the incremental axial surface displacement is given by $W(\rho,\phi) = d - f(\rho,\phi)$, with d being the indentation depth. ζ is the thermal conductivity, and the prescribed incremental heat flux is $\check{P}(\rho,\phi)$. For the convenience of the following derivation, we introduce the incremental equivalent heat flux $P(\rho,\phi) := \check{P}(\rho,\phi)/\zeta$. Outside the contact area, the surface is traction-free and subjected to a constant temperature condition. Therefore, the incremental boundary conditions at $z = 0$ yield

$$\begin{aligned}
&w_1 = W(\rho,\phi), \quad \zeta\frac{\partial\sigma_{z2}}{\partial z} = \check{P}(\rho,\phi), && (\rho,\phi)\in S\\
&\sigma_{z1} = 0, \qquad\quad \sigma_{z2} = 0, && (\rho,\phi)\notin S\\
&\sigma_{\rho 1} = 0, \qquad\quad \sigma_{\phi 1} = 0. && (\rho,\phi)\in[0,+\infty)\times[0,2\pi]
\end{aligned} \tag{16}$$

We take $\Psi_0 = 0$ and $\Psi_k = \sum_{i=1}^{2}\varsigma_{ki}\hat{H}_i(\rho,\phi,z_k)(k=1,2,3)$, where the potential functions read

$$\hat{H}_i(\rho,\phi,z_k) = \iint_S \ln\left[\sqrt{\rho^2+\rho_0^2-2\rho\rho_0\cos(\phi-\phi_0)+z_k^2}+z_k\right]\omega_i(\rho_0,\phi_0)\rho_0\mathrm{d}\rho_0\mathrm{d}\phi_0 \tag{17}$$

for $i = 1,2$ and $k = 1,2,3$, where ω_1 and ω_2 are the densities of single-layer potentials for incremental stress σ_{z1} and incremental temperature σ_{z2}, respectively. It is noted that Eq. (17) contains a logarithmic function whose argument has been non-dimensionalized through division by a unit length (1 m). This convention will be implicitly assumed throughout the rest of this work, as its repeated statement is unnecessary for clarity. In view of the properties of the single-layer potential (Fabrikant, 1989), it follows that

$$\begin{aligned}
&\lim_{z_k\to 0^+}\frac{\partial^2\hat{H}_i(\rho,\phi,z_k)}{\partial z_k^2} = -2\pi\omega_i(\rho,\phi) = -2\pi\sigma_{zi}(\rho,\phi,0), && (\rho,\phi)\in S\\
&\lim_{z_k\to 0^+}\frac{\partial^2\hat{H}_i(\rho,\phi,z_k)}{\partial z_k^2} = 0, && (\rho,\phi)\notin S
\end{aligned} \tag{18}$$

for $i = 1, 2$. In view of Eqs. (15), (16), and (18), we have

$$\begin{aligned}\sigma_{zj}(\rho,\phi,0) &= \sum_{i=1}^{2}\sum_{k=1}^{3}\gamma_{jk}\varsigma_{ki}\lim_{z_k\to 0^+}\frac{\partial^2\hat{H}_i(\rho,\phi,z_k)}{\partial z_k^2} = -2\pi\sum_{i=1}^{2}\sum_{k=1}^{3}\gamma_{jk}\varsigma_{ki}\sigma_{zi}(\rho,\phi,0),\\ \sigma_{\rho 1}(\rho,\phi,0) &= \sum_{i=1}^{2}\sum_{k=1}^{3}\varpi_{1k}\varsigma_{ki}\lim_{z_k\to 0^+}\frac{\partial^2\hat{H}_i(\rho,\phi,z_k)}{\partial z_k\partial\rho} = 0,\end{aligned} \tag{19}$$

leading to

$$\sum_{k=1}^{3}\gamma_{jk}\varsigma_{ki} = -\delta_{ji}/2\pi, \qquad \sum_{k=1}^{3}\varpi_{1k}\varsigma_{ki} = 0, \tag{20}$$

for $i, j = 1, 2$, where $\gamma_{1k} = \mathrm{A}_{01133} + \mathrm{A}_{03333}\alpha_k s_k - \mathrm{M}_{033}\beta_k$, $\gamma_{2k} = \beta_k$, and $\varpi_{1k} = -\mathrm{A}_{03131}s_k + \mathrm{A}_{01331}\alpha_k$. Note that $\sigma_{\phi 1}(\rho,\phi,0) = 0$ yields the same relation as $\sigma_{\rho 1}(\rho,\phi,0) = 0$ when $\Psi_0 = 0$. Hence, the condition $\sigma_{\phi 1} = 0$ is omitted for brevity. Here, the order of summation in Eq. (19) has been interchanged for the convenience of subsequent derivations. From Eq. (20), we can solve for $\varsigma_{ki}(k = 1, 2, 3; i = 1, 2)$ via

$$\begin{Bmatrix}\varsigma_{1i}\\ \varsigma_{2i}\\ \varsigma_{3i}\end{Bmatrix} = -\frac{1}{2\pi}\begin{bmatrix}\varpi_{11} & \varpi_{12} & \varpi_{13}\\ \gamma_{11} & \gamma_{12} & \gamma_{13}\\ \gamma_{21} & \gamma_{22} & \gamma_{23}\end{bmatrix}^{-1}\begin{Bmatrix}0\\ \delta_{1i}\\ \delta_{2i}\end{Bmatrix}. \tag{21}$$

Once the coefficients ς_{ki} for combination of potential functions are established, the densities ω_i remain to be determined. To this end, we resort to the boundary conditions prescribed on $(\rho,\phi) \in S$. As stated in Eq. $(16)_{1\text{-}2}$, we have

$$\begin{aligned}w_1 = W(\rho,\phi) &= \sum_{i=1}^{2}\sum_{k=1}^{3}\alpha_k\varsigma_{ki}\lim_{z_k\to 0^+}\frac{\partial\hat{H}_i(\rho,\phi,z_k)}{\partial z_k}\\ &= \sum_{i=1}^{2}\sum_{k=1}^{3}\alpha_k\varsigma_{ki}\iint_S\frac{\omega_i(\rho_0,\phi_0)\rho_0\mathrm{d}\rho_0\mathrm{d}\phi_0}{\sqrt{\rho^2+\rho_0^2-2\rho\rho_0\cos(\phi-\phi_0)}},\end{aligned} \tag{22}$$

$$\begin{aligned}\frac{\partial\sigma_{z2}}{\partial z} = P(\rho,\phi) &= \sum_{i=1}^{2}\sum_{k=1}^{3}\gamma_{2k}\varsigma_{ki}\lim_{z_k\to 0^+}\frac{\partial^3\hat{H}_i(\rho,\phi,z_k)}{\partial z_k^3}\\ &= \sum_{i=1}^{2}\sum_{k=1}^{3}\gamma_{2k}\varsigma_{ki}\lim_{z_k\to 0^+}\frac{\partial^2}{\partial z_k^2}\iint_S\frac{\omega_i(\rho_0,\phi_0)\rho_0\mathrm{d}\rho_0\mathrm{d}\phi_0}{\sqrt{\rho^2+\rho_0^2-2\rho\rho_0\cos(\phi-\phi_0)+z_k^2}}.\end{aligned} \tag{23}$$

Since s_k are the roots of the numerator of β_k given in Appendix A, we arrive at $\beta_k = 0$ for $k = 1, 2$, which implies $\gamma_{2k} = 0(k = 1, 2)$ and $\varsigma_{31} = 0$. Therefore, Eq. (23) can be further simplified to

$$P(\rho,\phi) = \beta_3\varsigma_{32}\lim_{z_3\to 0^+}\frac{\partial^2}{\partial z_3^2}\iint_S\frac{\omega_2(\rho_0,\phi_0)\rho_0\mathrm{d}\rho_0\mathrm{d}\phi_0}{\sqrt{\rho^2+\rho_0^2-2\rho\rho_0\cos(\phi-\phi_0)+z_3^2}}. \tag{24}$$

Following Appendix B of Chen et al. (2026), Eq. (24) is first solved for ω_2; once derived, it is then substituted into

$$\iint_S\frac{\omega_1(\rho_0,\phi_0)\rho_0\mathrm{d}\rho_0\mathrm{d}\phi_0}{\sqrt{\rho^2+\rho_0^2-2\rho\rho_0\cos(\phi-\phi_0)}} = \frac{1}{\sum_{k=1}^{3}\alpha_k\varsigma_{k1}}\left[W(\rho,\phi) - \sum_{k=1}^{3}\alpha_k\varsigma_{k2}\iint_S\frac{\omega_2(\rho_0,\phi_0)\rho_0\mathrm{d}\rho_0\mathrm{d}\phi_0}{\sqrt{\rho^2+\rho_0^2-2\rho\rho_0\cos(\phi-\phi_0)}}\right] \tag{25}$$

to obtain ω_1, where Eq. (25) follows from Eq. (22). For the torsionless axisymmetric case, $\partial(\#)/\partial\phi = 0$, $u_\phi = 0$, and $\sigma_{\phi i} = 0$ for $i = 1, 2$ are adopted. With $S = \{(\rho,\phi)|0 \leqslant \rho \leqslant a; 0 \leqslant \phi \leqslant 2\pi\}$, the densities are derived by inverting the integro-differential equations, as

$$\begin{aligned}\omega_2(\rho,\phi) =& \frac{1}{\pi^2\beta_3\varsigma_{32}}\int_\rho^a\frac{\mathrm{d}x}{\sqrt{x^2-\rho^2}}\int_0^x\frac{\rho_0\mathrm{d}\rho_0}{\sqrt{x^2-\rho_0^2}}\mathcal{L}\left(\frac{\rho\rho_0}{x^2}\right)P(\rho_0,\phi),\\ \omega_1(\rho,\phi) =& -\frac{1}{\pi^2\rho}\mathcal{L}(\rho)\frac{\mathrm{d}}{\mathrm{d}\rho}\int_\rho^a\frac{t\mathrm{d}t}{\sqrt{t^2-\rho^2}}\mathcal{L}\left(\frac{1}{t^2}\right)\frac{\mathrm{d}}{\mathrm{d}t}\int_0^t\frac{\rho_0\mathrm{d}\rho_0}{\sqrt{t^2-\rho_0^2}}\mathcal{L}(\rho_0)\times\\ &\frac{1}{\sum_{k=1}^{3}\alpha_k\varsigma_{k1}}\left[W(\rho_0,\phi) - 4\sum_{k=1}^{3}\alpha_k\varsigma_{k2}\int_0^{\rho_0}\frac{\mathrm{d}x}{\sqrt{\rho_0^2-x^2}}\int_x^a\frac{y\mathrm{d}y}{\sqrt{y^2-x^2}}\mathcal{L}\left(\frac{x^2}{\rho_0 y}\right)\omega_2(y,\phi)\right],\end{aligned} \tag{26}$$

where $\mathcal{L}(\#)$ is a Poisson operator defined as $\mathcal{L}(k)f(\phi) := \frac{1}{2\pi}\int_0^{2\pi}\mathcal{G}(k,\phi-\phi_0)f(\phi_0)\mathrm{d}\phi_0$ when $0 < k < 1$. Here, $\mathcal{G}(k,\phi) := \sum_{n=-\infty}^{+\infty}k^{|n|}\mathrm{e}^{\mathrm{i}n\phi} = (1-k^2)/[1+k^2-2k\cos(\phi)]$.

To validate the analytical solution, we consider the thermoelastic contact between a flat punch with constant incremental heat flux and a hyperelastic half-space surface (i.e., $W(\rho,\phi)$ and $P(\rho,\phi)$ are both constant, denoted by d and P, respectively), in the absence of friction and adhesion. The densities are then solved as

$$\omega_2(\rho)=\frac{P}{\pi^2\beta_3\varsigma_{32}}\sqrt{a^2-\rho^2},\quad \omega_1(\rho)=\frac{1}{\pi^2}\left(\frac{d}{\sum_{k=1}^3\alpha_k\varsigma_{k1}}\frac{1}{\sqrt{a^2-\rho^2}}-\frac{\sum_{k=1}^3\alpha_k\varsigma_{k2}}{\sum_{k=1}^3\alpha_k\varsigma_{k1}}\frac{P}{\beta_3\varsigma_{32}}\sqrt{a^2-\rho^2}\right). \tag{27}$$

The expression of ω_1 shows that the flat punch induces a stress singularity at the edge of the contact area. According to Chen et al. (2026), the potential functions $\hat{H}_i$ in Eq. (17) can be rewritten as

$$\hat{H}_i(\rho,\phi,z_k)=\int\left[4\int_0^{l_1(a)}\frac{\mathrm{d}x}{\sqrt{\rho^2-x^2}}\int_{g(x)}^{a}\frac{\rho_0\mathrm{d}\rho_0}{\sqrt{\rho_0^2-g^2(x)}}\mathcal{L}\left(\frac{x^2}{\rho\rho_0}\right)\omega_i(\rho_0,\phi)\right]\mathrm{d}z_k, \tag{28}$$

where $l_1(a)=l_1(a,\rho,z_k):=\left[\sqrt{(\rho+a)^2+z_k^2}-\sqrt{(\rho-a)^2+z_k^2}\right]/2$ and $g(x):=x\sqrt{1+z_k^2/(\rho^2-x^2)}$. Here, the physical quantities are connected to the potential functions via derivative relations, which indicate that the constants of integration over z_k in Eq. (28) are inconsequential to the final results. Thus, we have

$$\begin{aligned}\hat{H}_1(\rho,\phi,z_k)=\frac{2}{\pi}\frac{d}{\sum_{k=1}^3\alpha_k\varsigma_{k1}}&\left\{-\sqrt{a^2-l_1^2(a)}+\frac{\sqrt{[a^2-l_1^2(a)][\rho^2-l_1^2(a)]}}{l_1(a)}\arcsin\left[\frac{l_1(a)}{\rho}\right]\right.\\&\left.-a\ln\left[\frac{l_1(a)}{a\left(a+\sqrt{a^2-l_1^2(a)}\right)}\right]\right\}+\frac{\sum_{k=1}^3\alpha_k\varsigma_{k2}}{\sum_{k=1}^3\alpha_k\varsigma_{k1}}\frac{P}{\pi\beta_3\varsigma_{32}}\left\{\frac{\sqrt{a^2-l_1^2(a)}}{18}[5l_1^2(a)-9\rho^2+16a^2+6z_k^2]\right.\\&\left.-\frac{\sqrt{[a^2-l_1^2(a)][\rho^2-l_1^2(a)]}}{6l_1(a)}(2z_k^2+6a^2-3\rho^2)\arcsin\left[\frac{l_1(a)}{\rho}\right]+\frac{2a^3}{3}\ln\left[\frac{l_1(a)}{a\left(a+\sqrt{a^2-l_1^2(a)}\right)}\right]\right\},\end{aligned} \tag{29}$$

$$\begin{aligned}\hat{H}_2(\rho,\phi,z_k)=\frac{P}{\pi\beta_3\varsigma_{32}}&\left\{\frac{\sqrt{[a^2-l_1^2(a)][\rho^2-l_1^2(a)]}}{6l_1(a)}(2z_k^2+6a^2-3\rho^2)\arcsin\left[\frac{l_1(a)}{\rho}\right]\right.\\&\left.-\frac{2a^3}{3}\ln\left[\frac{l_1(a)}{a\left(a+\sqrt{a^2-l_1^2(a)}\right)}\right]-\frac{\sqrt{a^2-l_1^2(a)}}{18}[5l_1^2(a)-9\rho^2+16a^2+6z_k^2]\right\},\end{aligned} \tag{30}$$

where $z_k^2=l_1^2(a)+\rho^2a^2/l_1^2(a)-a^2-\rho^2$ and $\mathrm{d}z_k=-[l_2^2(a)-l_1^2(a)]/[z_kl_1(a)]\mathrm{d}l_1(a)$ are utilized in solving Eqs. (29) and (30), with $l_2(a)=l_2(a,\rho,z_k):=\left[\sqrt{(\rho+a)^2+z_k^2}+\sqrt{(\rho-a)^2+z_k^2}\right]/2$. This result then allows us to further determine the physical quantities in Eqs. (14) and (15). For instance, the incremental surface displacement

$$\begin{aligned}u_z|_{z=0}&=\sum_{i=1}^{2}\sum_{k=1}^{3}\alpha_k\varsigma_{ki}\left.\frac{\partial\hat{H}_i(\rho,\phi,z_k)}{\partial z_k}\right|_{z_k=0}\\&=4\sum_{i=1}^{2}\sum_{k=1}^{3}\alpha_k\varsigma_{ki}\int_0^{\min(\rho,a)}\frac{\mathrm{d}x}{\sqrt{\rho^2-x^2}}\int_x^a\frac{\rho_0\mathrm{d}\rho_0}{\sqrt{\rho_0^2-x^2}}\mathcal{L}\left(\frac{x^2}{\rho\rho_0}\right)\omega_i(\rho_0,\phi)\end{aligned} \tag{31}$$

is of interest in the contact analysis, which leads to

$$u_z|_{z=0}=\begin{cases}d, & (0\leqslant\rho\leqslant a)\\ \frac{2}{\pi}\arcsin\left(\frac{a}{\rho}\right)d. & (\rho>a)\end{cases} \tag{32}$$

The incremental surface displacement presented in Eq. (32) matches the boundary condition $w_1=d$ within the contact area $0\leqslant\rho\leqslant a$, thereby confirming the validity of the analytical solutions. Once the indenter comes into contact with the half-space, the incremental surface displacement is governed solely by the compatibility condition and remains unaffected by the temperature field. The thermal

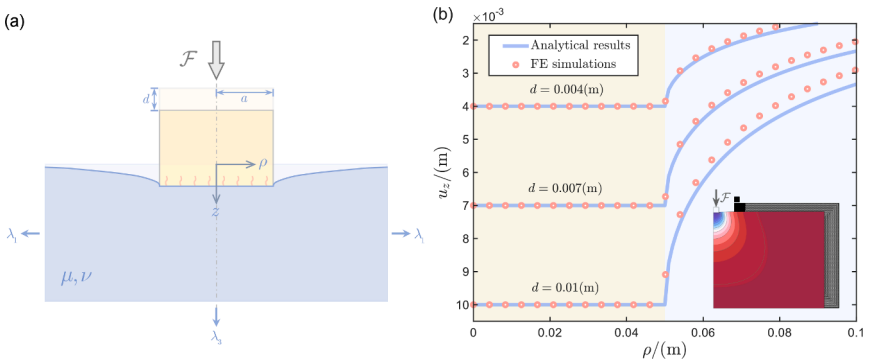


Fig. 4. Comparison between FE simulations and analytical solutions. (a) Schematic diagram of thermal indentation with a flat punch and (b) axial displacement $u_z|_{z=0}$ within the region near the indenter, specifically for $\rho \in [0, 0.1]$(m), with $\lambda_1 = 1.054$, $\mu = 1.0$(MPa), $\nu = 0.45$, $\kappa_1 = 1.0 \times 10^{-4}$(1/K), $\kappa_3 = 1.5 \times 10^{-4}$(1/K), $\Theta - \Theta_{\text{ref}} = 0.1$(K), and $P = 0.01$(K/m). Different colors are used to distinguish the contact zone $0 \leqslant \rho \leqslant a = 0.05$(m) from the area outside contact, i.e., $\rho > a$. In the two dimensional axisymmetric finite element simulation, a cylindrical geometry of radius 1(m) and height 1(m) is employed, which is substantially larger than the contact area to represent a half-space. The mesh contains 37,770 triangular elements and 19,182 nodes, as illustrated in (b). The augmented Lagrangian method (ALM) is adopted in finite element simulation to solve the contact problem (Mijar and Arora, 2004), which formulates the constrained minimization via the functional $\mathfrak{L}_{\text{ALM}}(\mathbf{u}, \varrho) = \Pi(\mathbf{u}) + \int_{\Gamma_c} (\varrho \langle \check{g}_n \rangle_- + \jmath \langle \check{g}_n \rangle_-^2 / 2) \mathrm{d}\Gamma$, where $\Pi(\mathbf{u})$ is the total potential energy, Γ_c is the contact boundary, $\langle \# \rangle_- := \min(0, \#)$ denotes the negative part, $\check{g}_n(\mathbf{u})$ is the normal gap, ϱ is the contact pressure multiplier, and $\jmath > 0$ is a penalty parameter. The solution is obtained through an iterative Uzawa scheme in which $\mathbf{u}^{[k+1]}$ minimizes $\mathfrak{L}_{\text{ALM}}$ for fixed $\varrho^{[k]}$, followed by the multiplier update $\varrho^{[k+1]} = \langle \varrho^{[k]} + \jmath \check{g}_n(\mathbf{u}^{[k+1]}) \rangle_-$, guaranteeing exact satisfaction of the Karush-Kuhn-Tucker conditions upon convergence.

effects manifest in the stress response, as can be seen from Eq. (33). Besides, the incremental indentation force follows

$$\mathcal{F}(d) := -\int_0^{2\pi} \int_0^a \omega_1(\rho, \phi) \rho \mathrm{d}\rho \mathrm{d}\phi = \frac{2}{\pi} \left(\frac{\sum_{k=1}^3 \alpha_k \varsigma_{k2}}{\sum_{k=1}^3 \alpha_k \varsigma_{k1}} \frac{P a^3}{3 \beta_3 \varsigma_{32}} - \frac{d a}{\sum_{k=1}^3 \alpha_k \varsigma_{k1}} \right). \tag{33}$$

It is worth noting that when $P < 0$ (corresponding to thermal contraction), the condition for initial contact shifts from $d = 0$ to $d = P a^2 \left(\sum_{k=1}^3 \alpha_k \varsigma_{k2} \right) / (3 \beta_3 \varsigma_{32}) > 0$ in order to maintain a non-negative contact force $\mathcal{F}(d) \geqslant 0$.

Finite element (FE) simulations are also carried out for a neoHookean hyperelastic half-space (with the energy density function $\Omega = \mu(J_e^{-2\Lambda} - 1)/(2\Lambda) + \mu(\mathcal{I}_1 - 3)/2$, where $\Lambda = \nu/(1 - 2\nu)$, μ is shear modulus, and ν is Poisson's ratio) to evaluate the accuracy of the theoretical model, as illustrated in Fig. 4. The numerical results exhibit excellent consistency with the analytical solution. We have analyzed the indentation results not only for flat punch but also for conical and spherical indenters. The corresponding analytical solutions for these indenter profiles, as well as the solution for polynomial indenter profiles, are provided in Appendix B. It is found that the accuracy of the theoretical predictions diminishes when the indentation depth becomes relatively large. This is because the incremental theory provides accurate predictions only under relatively small perturbations; consequently, a multi-step incremental procedure is required for large incremental loadings. For spherical indenters, the common practice of approximating the indenter profile (when ρ/R is small enough) by a parabolic function $\rho^2/(2R)$ introduces additional error. This error can be mitigated by employing a higher-order expansion of the profile function, which yields enhanced accuracy.

4. Contact between a rigid indenter and a wavy surface

The objective of nanoimprint lithography is to transfer the pattern from a mask (indenter) onto the target material, making it particularly important to analyze the imprinting process and the stress distributions for surfaces with topographic features. Based on the solutions for nonlinear thermoelastic contact established in Section 3, we further investigate the contact and adhesion between wavy surfaces using the potential theory method, which facilitates precise control in the nanoimprint process and contributes to improved imprint fidelity. We first analyze the case of non-adhesive contact, and subsequently incorporate the adhesion effect and viscoelasticity.

4.1. Non-adhesive contact

As illustrated in Fig. 5, the axisymmetric wavy surface in $\mathcal{B}^{\text{II}}$ is described by $\mathrm{M}(\rho) = \Upsilon[1 - \cos(2\pi\rho/\ell)]$, where Υ denotes the amplitude of the waviness and its wavelength ℓ (Guduru, 2007). The boundary conditions are taken to be identical to those presented in Eq. (16). The indenter is assumed to be rigid, spherical, and in frictionless, non-adhesive contact, with its profile approximated by $\rho^2/(2R)$. The surface displacement within the contact area is then expressed as $W(\rho, \phi) := d - f(\rho) = d - \{\rho^2/(2R) + \Upsilon[1 - \cos(2\pi\rho/\ell)]\}$. In order to maintain a simply connected contact area upon indentation, it is necessary that $f(\rho)$ be monotonically increasing with ρ. This monotonicity condition, namely $\mathrm{d}f/\mathrm{d}\rho > 0$ for $\rho > 0$, yields the inequality $\ell^2/(4\pi^2 \Upsilon R) > -\sin(2\pi\rho/\ell)/(2\pi\rho/\ell)$.

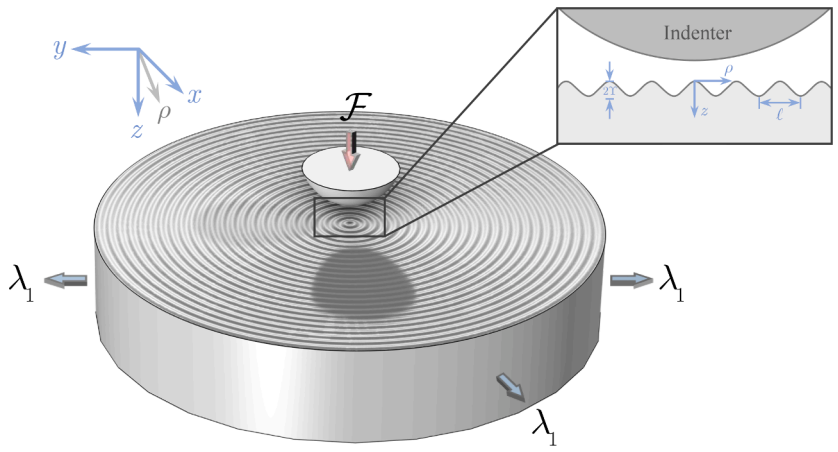


Fig. 5. Schematic diagram of contact between a rigid indenter and an axisymmetric wavy surface of a pre-deformed hyperelastic half-space. The wavy surface has amplitude Υ and wavelength ℓ. The coordinate system is also indicated in the figure.

If the incremental equivalent heat flux $P(\rho,\phi)$ is prescribed as a constant value P over the contact area, the density ω_2 remains unchanged as that in Eq. (27). Consequently, ω_1 can be determined from Eq. (26) as

$$\begin{aligned}\omega_1(\rho) = {} & \frac{1}{\pi^2\sum_{k=1}^3\alpha_k\varsigma_{k1}}\left\{\frac{d-\frac{a^2}{R}-\Upsilon\frac{\pi^2 a}{\ell}\widehat{H}_0\left(\frac{2\pi}{\ell}a\right)}{\sqrt{a^2-\rho^2}}+\left(\frac{2}{R}-\frac{P\sum_{k=1}^3\alpha_k\varsigma_{k2}}{\beta_3\varsigma_{32}}+\frac{4\pi^2\Upsilon}{\ell^2}\right)\sqrt{a^2-\rho^2}\right\}\\ & +\frac{\Upsilon}{\ell\sum_{k=1}^3\alpha_k\varsigma_{k1}}\int_\rho^a\frac{1}{\sqrt{t^2-\rho^2}}\left[\widehat{H}_0\left(\frac{2\pi}{\ell}t\right)-\frac{2\pi}{\ell}t\widehat{H}_1\left(\frac{2\pi}{\ell}t\right)\right]\mathrm{d}t,\end{aligned} \tag{34}$$

where $\widehat{H}_v(\#)$ is the Struve function of the first kind. $\mathrm{d}[t\widehat{H}_{-1}(t)]/\mathrm{d}t = 2/\pi - t\widehat{H}_0(t)$ and $\widehat{H}_{-1}(t)+\widehat{H}_1(t) = 2/\pi$ are adopted to obtain Eq. (34). For spherical indentation, no stress singularity occurs at the contact edge. Thus, the coefficient of the $1/\sqrt{a^2-\rho^2}$ term is required to vanish, from which the relationship between indentation depth d and contact radius a follows

$$d = \frac{a^2}{R}+\Upsilon\frac{\pi^2 a}{\ell}\widehat{H}_0\left(\frac{2\pi a}{\ell}\right). \tag{35}$$

Besides, the incremental indentation force is described as

$$\begin{aligned}\mathcal{F}(a) = {} & \frac{2}{\pi}\left[\frac{\sum_{k=1}^3\alpha_k\varsigma_{k2}}{\sum_{k=1}^3\alpha_k\varsigma_{k1}}\frac{P}{\beta_3\varsigma_{32}}-\frac{2/R+4\pi^2\Upsilon/\ell^2}{\sum_{k=1}^3\alpha_k\varsigma_{k1}}\right]\int_0^a\sqrt{a^2-\rho^2}\rho\mathrm{d}\rho\\ & -\frac{2\pi\Upsilon/\ell}{\sum_{k=1}^3\alpha_k\varsigma_{k1}}\int_0^a t\left[\widehat{H}_0\left(\frac{2\pi}{\ell}t\right)-\frac{2\pi}{\ell}t\widehat{H}_1\left(\frac{2\pi}{\ell}t\right)\right]\mathrm{d}t\\ = {} & \frac{2a^3}{3\pi}\left[\frac{\sum_{k=1}^3\alpha_k\varsigma_{k2}}{\sum_{k=1}^3\alpha_k\varsigma_{k1}}\frac{P}{\beta_3\varsigma_{32}}-\frac{2/R}{\sum_{k=1}^3\alpha_k\varsigma_{k1}}\right]+\frac{\Upsilon}{\sum_{k=1}^3\alpha_k\varsigma_{k1}}\left[a\widehat{H}_1\left(\frac{2\pi}{\ell}a\right)-\frac{2\pi}{\ell}a^2\widehat{H}_0\left(\frac{2\pi}{\ell}a\right)\right],\end{aligned} \tag{36}$$

where the order of integration is reversed to evaluate Eq. (36).

4.2. Adhesive contact

When adhesion is incorporated into axisymmetric contact analysis, we introduce the notation

$$\mathcal{E}_1(t) := \frac{\mathrm{d}}{\mathrm{d}t}\int_0^t\frac{\mathcal{W}(\rho_0,\phi)\rho_0\mathrm{d}\rho_0}{\sqrt{t^2-\rho_0^2}}, \tag{37}$$

in terms of which the density ω_1 is expressed as

$$\omega_1(\rho) = -\frac{1}{\pi^2\rho}\frac{\mathrm{d}}{\mathrm{d}\rho}\int_\rho^a\frac{t\mathrm{d}t}{\sqrt{t^2-\rho^2}}\mathcal{E}_1(t) = \frac{1}{\pi^2}\left[\frac{\mathcal{E}_1(a)}{\sqrt{a^2-\rho^2}}-\int_\rho^a\frac{\mathrm{d}t}{\sqrt{t^2-\rho^2}}\frac{\mathrm{d}\mathcal{E}_1(t)}{\mathrm{d}t}\right], \tag{38}$$

where $\mathcal{W}(\rho,\phi) := \left[\frac{W(\rho,\phi)}{\sum_{k=1}^{3}\alpha_k\varsigma_{k1}} - \frac{\sum_{k=1}^{3}\alpha_k\varsigma_{k2}}{\sum_{k=1}^{3}\alpha_k\varsigma_{k1}} \iint_S \frac{\omega_2(\rho_0,\phi_0)\rho_0 \mathrm{d}\rho_0\mathrm{d}\phi_0}{\sqrt{\rho^2+\rho_0^2-2\rho\rho_0\cos(\phi-\phi_0)}}\right]$. Then, the incremental indentation force accordingly follows as

$$\mathcal{F}(a) = -\frac{2}{\pi}\int_0^a \left[\frac{\mathcal{E}_1(a)}{\sqrt{a^2-\rho^2}} - \int_\rho^a \frac{\mathrm{d}t}{\sqrt{t^2-\rho^2}}\frac{\mathrm{d}\mathcal{E}_1(t)}{\mathrm{d}t}\right]\rho\mathrm{d}\rho = -\frac{2}{\pi}\int_0^a \mathcal{E}_1(t)\mathrm{d}t. \tag{39}$$

For hyperelastic materials, the Tabor number is relatively large. Therefore, the JKR model is adopted here. If we further define the incremental stress intensity factor $K_\mathrm{I}(a)$ as

$$K_\mathrm{I} := \lim_{\rho\to a}\left[\sqrt{2\pi(a-\rho)}\omega_1(\rho)\right] = \frac{\mathcal{E}_1(a)}{\pi\sqrt{\pi a}} \tag{40}$$

at the contact edge, ω_1 can be rewritten as $\omega_1(\rho) = \sqrt{\frac{a}{\pi}}\frac{K_\mathrm{I}}{\sqrt{a^2-\rho^2}} - \frac{1}{\pi^2}\int_\rho^a \frac{\mathrm{d}t}{\sqrt{t^2-\rho^2}}\frac{\mathrm{d}\mathcal{E}_1(t)}{\mathrm{d}t}$. Adopting the framework developed by Maugis (2000), the indentation unloading process can be treated as a crack growth problem. This analogy leads to the incremental energy release rate at the contact edge

$$G = \lim_{\delta a\to 0}\frac{1}{\delta a}\int_0^{\delta a}\frac{1}{2}\omega_1(a-\delta\rho,\phi,0)[\![w_1]\!](a+\delta a-\delta\rho,\phi,0)\mathrm{d}(\delta\rho), \tag{41}$$

where δa represents the infinitesimal decrease in the contact radius, corresponding to a crack extension increment, and $\delta\rho$ is the infinitesimal increment in the radial coordinate. It should be noted that Maugis's definition of the energy release rate for fracture has been modified herein to accommodate contact analysis, as expressed in Eq. (41). The density ω_1 corresponds to the incremental surface normal stress, which is evaluated as

$$\begin{aligned}\omega_1(a-\delta\rho,\phi,0) &= \sqrt{\frac{a}{\pi}}\frac{K_\mathrm{I}}{\sqrt{2a\delta\rho-(\delta\rho)^2}} - \frac{1}{\pi^2}\int_{a-\delta\rho}^{a}\frac{\mathrm{d}t}{\sqrt{t^2-(a-\delta\rho)^2}}\frac{\mathrm{d}\mathcal{E}_1(t)}{\mathrm{d}t}\\ &\simeq \sqrt{\frac{a}{\pi}}\frac{K_\mathrm{I}}{\sqrt{2a\delta\rho}},\end{aligned} \tag{42}$$

since the first term of Eq. (42) becomes singular as $\delta\rho\to 0$. $[\![w_1]\!]$ denotes the incremental surface displacement discontinuity. To evaluate it, we first simplify Eq. (22) as

$$\begin{aligned}w_1 &= 4K_\mathrm{I}\sqrt{\frac{a}{\pi}}\sum_{k=1}^{3}\alpha_k\varsigma_{k1}\int_0^\rho\frac{\mathrm{d}x}{\sqrt{\rho^2-x^2}}\int_x^a\frac{\rho_0\mathrm{d}\rho_0}{\sqrt{a^2-\rho_0^2}\sqrt{\rho_0^2-x^2}}\\ &-\frac{4}{\pi^2}\sum_{k=1}^{3}\alpha_k\varsigma_{k1}\int_0^\rho\frac{\mathrm{d}x}{\sqrt{\rho^2-x^2}}\int_x^a\int_x^t\frac{\rho_0\mathrm{d}\rho_0}{\sqrt{t^2-\rho_0^2}\sqrt{\rho_0^2-x^2}}\frac{\mathrm{d}\mathcal{E}_1(t)}{\mathrm{d}t}\mathrm{d}t\\ &+\frac{4}{\pi^2}\sum_{k=1}^{3}\alpha_k\varsigma_{k2}\int_0^\rho\frac{\mathrm{d}x}{\sqrt{\rho^2-x^2}}\int_x^a\int_x^t\frac{\rho_0\mathrm{d}\rho_0}{\sqrt{t^2-\rho_0^2}\sqrt{\rho_0^2-x^2}}\frac{\mathrm{d}\mathcal{E}_2(t)}{\mathrm{d}t}\mathrm{d}t\\ &= \frac{2}{\pi}\sum_{k=1}^{3}\alpha_k\varsigma_{k1}\int_0^\rho\frac{\mathcal{E}_1(x)\mathrm{d}x}{\sqrt{\rho^2-x^2}} + \frac{2}{\pi}\sum_{k=1}^{3}\alpha_k\varsigma_{k2}\int_0^\rho\frac{\mathrm{d}x}{\sqrt{\rho^2-x^2}}\int_x^a\mathcal{E}_2(t)\mathrm{d}t,\end{aligned} \tag{43}$$

where $\mathcal{E}_2$ fulfills $\omega_2(\rho_0) = \frac{1}{\pi^2}\int_{\rho_0}^a\frac{\mathcal{E}_2(x)\mathrm{d}x}{\sqrt{x^2-\rho_0^2}}$. Here, Eq. (40) is involved in the derivation above. Hence, $w_1(a+\delta\rho,\phi,0)$ is obtained as

$$\begin{aligned}w_1(a+\delta\rho,\phi,0) &= \frac{2}{\pi}\sum_{k=1}^{3}\alpha_k\varsigma_{k1}\left[\int_0^a\frac{\mathcal{E}_1(x)\mathrm{d}x}{\sqrt{(a+\delta\rho)^2-x^2}} + \int_a^{a+\delta\rho}\frac{\mathcal{E}_1(x)\mathrm{d}x}{\sqrt{(a+\delta\rho)^2-x^2}}\right]\\ &+\frac{2}{\pi}\sum_{k=1}^{3}\alpha_k\varsigma_{k2}\left[\int_0^a\frac{\mathrm{d}x}{\sqrt{(a+\delta\rho)^2-x^2}}\int_x^a\mathcal{E}_2(t)\mathrm{d}t + \int_a^{a+\delta\rho}\frac{\mathrm{d}x}{\sqrt{(a+\delta\rho)^2-x^2}}\int_x^a\mathcal{E}_2(t)\mathrm{d}t\right]\\ &\simeq \frac{2}{\pi}\sum_{k=1}^{3}\alpha_k\varsigma_{k1}\int_a^{a+\delta\rho}\frac{\mathcal{E}_1(a)\mathrm{d}x}{\sqrt{(a+\delta\rho)^2-a^2}}\\ &\simeq 2\pi\sum_{k=1}^{3}\alpha_k\varsigma_{k1}\sqrt{\frac{\delta\rho}{2\pi}}K_\mathrm{I},\end{aligned} \tag{44}$$

leading to $[\![w_1]\!](a+\delta\rho,\phi,0) = -2w_1 = -4\pi\sum_{k=1}^{3}\alpha_k\varsigma_{k1}\sqrt{\frac{\delta\rho}{2\pi}}K_\mathrm{I}$. Since the crack tip advances by δa during the detachment process, the reference point for the displacement discontinuity should be readjusted accordingly, which results in $[\![w_1]\!](a+\delta a-\delta\rho,\phi,0) = -4\pi\sum_{k=1}^{3}\alpha_k\varsigma_{k1}\sqrt{\frac{\delta a-\delta\rho}{2\pi}}K_\mathrm{I}$. Substituting Eq. (42) and $[\![w_1]\!]$ into Eq. (41), the incremental energy release rate can be expressed as

$$G = -K_\mathrm{I}^2\sum_{k=1}^{3}\alpha_k\varsigma_{k1}\lim_{\delta a\to 0}\frac{1}{\delta a}\int_0^{\delta a}\sqrt{\frac{\delta a-\delta\rho}{\delta\rho}}\mathrm{d}(\delta\rho) = -\frac{\pi}{2}K_\mathrm{I}^2\sum_{k=1}^{3}\alpha_k\varsigma_{k1}. \tag{45}$$

According to Lu et al. (2011), the equilibrium condition is given by $\left(G-\eta\frac{\partial\mathcal{A}}{\partial\mathcal{A}_p}\right)\mathrm{d}\mathcal{A}_p=0$ for adhesive contact, in which η is the work of adhesion, following the Dupré equation, and $\mathcal{A}_p=\pi a^2$ denotes the projected area corresponding to the actual contact area $\mathcal{A}$. It is worth noting that in the classical JKR theory, the distinction between the actual contact area and its projected counterpart is not accounted for. The derivative takes the form $\partial\mathcal{A}/\partial\mathcal{A}_p=\sqrt{1+[f'(a)]^2}$ at $\rho=a$, leading to $G=\eta\sqrt{1+[f'(a)]^2}$. From Eq. (45) together with the expression for G, the incremental stress intensity factor is derived as

$$K_{\mathrm{I}}=\sqrt{-\frac{2\eta\sqrt{1+[a/R+(2\pi\Upsilon/\ell)\sin(2\pi a/\ell)]^2}}{\pi\sum_{k=1}^{3}\alpha_k\varsigma_{k1}}}. \tag{46}$$

Combining this result with Eqs. (37) and (40) yields the relationship between indentation depth d and contact radius a:

$$d=\frac{a^2}{R}+\Upsilon\frac{\pi^2 a}{\ell}\widehat{H}_0\left(\frac{2\pi a}{\ell}\right)+\sum_{k=1}^{3}\alpha_k\varsigma_{k1}\sqrt{-\frac{2\eta\pi^2 a\sqrt{1+[a/R+(2\pi\Upsilon/\ell)\sin(2\pi a/\ell)]^2}}{\sum_{k=1}^{3}\alpha_k\varsigma_{k1}}}, \tag{47}$$

when $P(\rho,\phi)=P$. Correspondingly, the incremental indentation force is expressed as

$$\begin{aligned}\mathcal{F}(a)=&\frac{2a^3}{3\pi}\left[\frac{\sum_{k=1}^{3}\alpha_k\varsigma_{k2}}{\sum_{k=1}^{3}\alpha_k\varsigma_{k1}}\frac{P}{\beta_3\varsigma_{32}}-\frac{2/R}{\sum_{k=1}^{3}\alpha_k\varsigma_{k1}}\right]+\frac{\Upsilon}{\sum_{k=1}^{3}\alpha_k\varsigma_{k1}}\left[a\widehat{H}_1\left(\frac{2\pi}{\ell}a\right)-\frac{2\pi}{\ell}a^2\widehat{H}_0\left(\frac{2\pi}{\ell}a\right)\right]\\&-\frac{2}{\pi}\sqrt{-\frac{2\eta\pi^2a^3\sqrt{1+[a/R+(2\pi\Upsilon/\ell)\sin(2\pi a/\ell)]^2}}{\sum_{k=1}^{3}\alpha_k\varsigma_{k1}}}.\end{aligned} \tag{48}$$

It can be seen that in the absence of adhesion (i.e., $\eta=0$), Eqs. (47) and (48) recover the forms given by Eqs. (35) and (36), respectively. To investigate the role of various non-dimensional quantities on the incremental indentation response, $\mathcal{F}(a)$ is normalized with the magnitude of the classical JKR maximum pull-off force $|\mathcal{F}_{\mathrm{JKR}}|:=3\pi\eta R/2$. Therefore, $\mathcal{F}^{\ddagger}:=\mathcal{F}/|\mathcal{F}_{\mathrm{JKR}}|$ can be represented in terms of the non-dimensional quantities, i.e., contact radius $a^{\ddagger}:=a/R$, wavelength $\ell^{\ddagger}:=\ell/R$, waviness amplitude $\Upsilon^{\ddagger}:=\Upsilon/\ell$, work of adhesion $\eta^{\ddagger}:=2\pi^2\eta\sum_{k=1}^{3}\alpha_k\varsigma_{k1}/R$, and incremental equivalent heat flux $P^{\ddagger}:=PR\sum_{k=1}^{3}\alpha_k\varsigma_{k2}/(2\beta_3\varsigma_{32})$. As depicted in panel (a) of Fig. 6, an increase in waviness amplitude (or a decrease in wavelength) amplifies the oscillation of $\mathcal{F}^{\ddagger}$ without altering the nodes. The cases of zero amplitude (or infinite wavelength) are indicated with thin dashed lines, where the wavy surface becomes perfectly flattened. Panel (b) reveals that as the non-dimensional incremental equivalent heat flux rises, the oscillation of the curve remains unchanged, whereas the dashed line shifts upward. In addition, applying different pre-stretches to the hyperelastic material can alter the amplitude and wavelength of the wavy surface, together with the instantaneous material tensors. These parameters in turn influence the non-dimensionl quantities $P^{\ddagger}$, $\Upsilon^{\ddagger}$, $\ell^{\ddagger}$, and $\eta^{\ddagger}$. Consequently, the sensitivity analysis presented in Fig. 6 can also be interpreted as the incremental indentation response of a hyperelastic half-space subjected to various pre-stretching. It should be noted that only the gray curve in panel (a) satisfies the monotonicity condition ($\ell^{\ddagger}/\Upsilon^{\ddagger}>-4\pi^2\sin(2\pi\rho/\ell)/(2\pi\rho/\ell)\approx 8.576$). As a result, the remaining cases are not valid for the "approach" problem because the contact region is not simply connected but annular when an indenter approaches a wavy surface. Yet this does not imply that those solutions are physically implausible. If the indenter is pressed sufficiently hard so that the contact area turns simply connected (i.e., ρ is large enough to fulfill the monotonicity condition), and then the indenter is retracted, the contact area will stay as a simply connected region throughout the detachment process until final pull-off.

The comparison in Fig. 7 shows that adhesion induces negative values of $\mathcal{F}^{\ddagger}$, which implies that contact can occur via adhesion alone in the absence of an applied force. A notable point is that the non-dimensional incremental indentation force can reach values below -1, which indicates that the inclusion of surface waviness enhances adhesion when compared with the classical JKR solution that neglects surface topography. Nevertheless, increasing waviness causes the adhesion mode to change from simple contact to multi-point contact, which in turn weakens the adhesive effect (Zhu et al., 2021). In contrast to linear elastic materials, hyperelastic materials offer the possibility of applying pre-stretch to modulate the equivalent modulus, equivalent inverse temperature, and surface waviness, thereby enabling tunable interface strength. Besides, compared with the classical JKR solution, the modified counterpart displays enhanced adhesion. This enhancement is attributed to the inclusion of the projected surface topography in the definition of surface energy within the modified JKR model. It is interesting to note that the interplay between the Struve function and the sinusoidal function causes irregular periodic oscillation in the modified JKR solution under incipient contact, as depicted in panel (a) of Fig. 7. Upon further indentation, the oscillations gradually settle into a regular pattern.

According to the expansions

$$d(a)=d^{\natural}(a)-\sqrt{\frac{\pi a}{2\ell}}\mathrm{N}\left(\frac{a}{\ell}\right)+a\mathcal{O}\left(\frac{\ell}{a}\right)\quad\text{and}\quad\mathcal{F}(a)=\mathcal{F}^{\natural}(a)+\frac{\sqrt{2a^3}}{\sqrt{\pi\ell}\sum_{k=1}^{3}\alpha_k\varsigma_{k1}}\mathrm{N}\left(\frac{a}{\ell}\right)+a^2\mathcal{O}\left(\frac{\ell}{a}\right) \tag{49}$$

proposed by Kesari and Lew (2011), Ciavarella (2016) demonstrated that the Guduru solution produces oscillations bounded by two exact classical JKR envelope curves for the smooth sphere. These envelope curves are obtained from an asymptotic solution that holds for small roughness dimensions, namely when $\ell\ll a$. Consequently, the contact area includes a sufficiently large number of roughness wavelengths (Kesari et al., 2010). Here $d^{\natural}$ and $\mathcal{F}^{\natural}$ are the indentation depth and incremental indentation force, respectively, both evaluated only considering indenter profile and adhesion. Meanwhile, $\mathrm{N}(\rho):=\mathscr{F}^{-1}\left[\sqrt{-\mathrm{i}\xi}\mathscr{F}[\mathrm{M}(\rho)](\xi)\right]$, in which $\mathscr{F}[\#]$ denotes

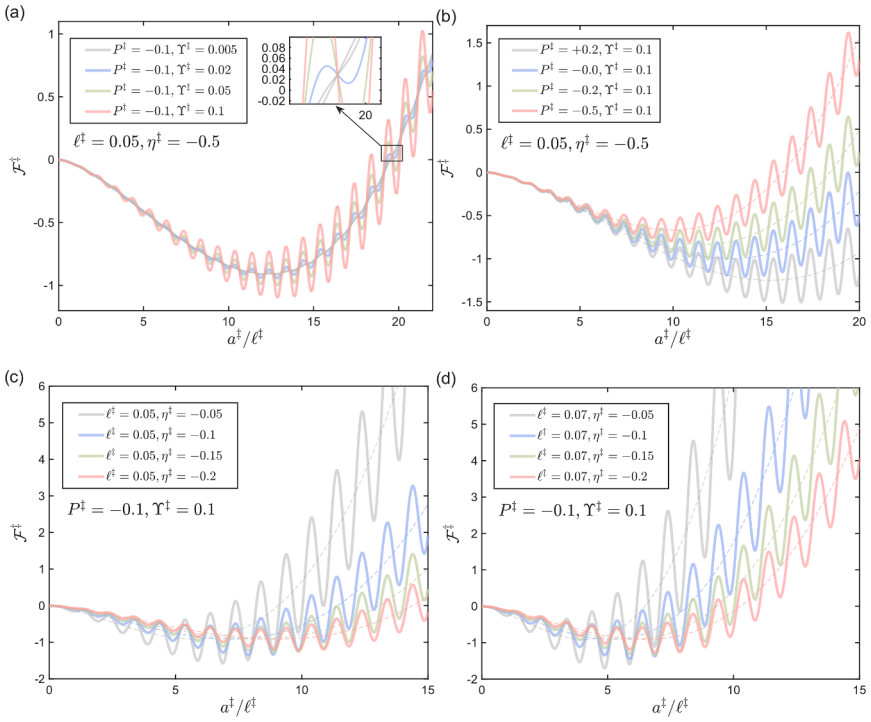


Fig. 6. Sensitivity of the adhesive incremental indentation response to non-dimensional quantities. Dependence of the non-dimensional incremental indentation forces on $a^\ddagger/\ell^\ddagger$, (a) $\Upsilon^\ddagger$, (b) $P^\ddagger$, and (c, d) $\eta^\ddagger$ & $\ell^\ddagger$ are shown in panels above. A magnified inset is created in (a) to distinguish the curves. (c) and (d) share an identical axis to allow comparison. The dashed lines represent the incremental indentation response of flattened surface.

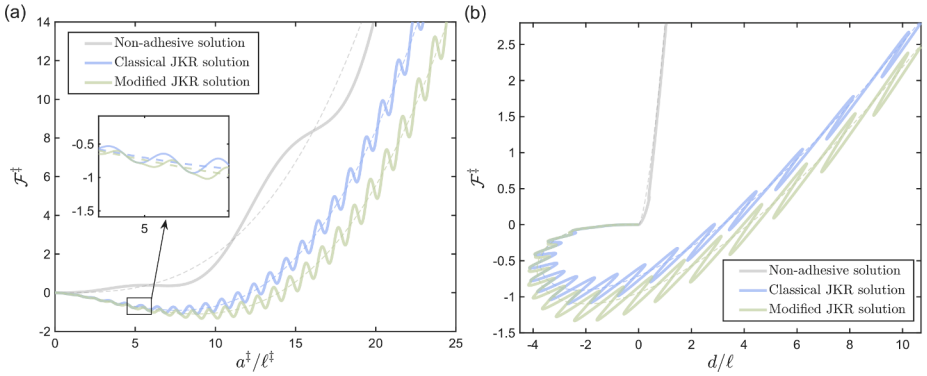


Fig. 7. Comparison among incremental indentation response predicted by the non-adhesive, classical JKR, and modified JKR models. (a) and (b) present the non-dimensional incremental indentation force versus the non-dimensional contact radius and indentation depth, respectively. The dashed lines represent the incremental indentation response of flattened surface. $P^\ddagger = -0.1$, $\Upsilon^\ddagger = 0.08$, $\ell^\ddagger = 0.8$, and $\eta^\ddagger = -0.5$ are taken in non-adhesive solution, while $P^\ddagger = -0.1$, $\Upsilon^\ddagger = 0.08$, $\ell^\ddagger = 0.08$, and $\eta^\ddagger = -0.5$ are adopted in adhesive solutions. A magnified inset is created in (a) to illustrate the irregular periodic oscillation.

the Fourier transform. $\mathcal{O}(\#)$ is the Landau symbol. Hence, the envelope curves for incremental contact analysis based on the classical JKR theory are derived as

$$
\begin{aligned}
d_{\mathrm{env}}(a) &= \frac{a^2}{R} - a^{1/2}\sqrt{2\pi\eta\left(-\pi\sum_{k=1}^{3}\alpha_k\varsigma_{k1}\right)}\left\{1 \pm \frac{1}{\sqrt{\pi}\alpha_{\mathrm{KLJ}}}\right\}, \\
\mathcal{F}_{\mathrm{env}}(a) &= \frac{2a^3}{3\pi}\left[\frac{\sum_{k=1}^{3}\alpha_k\varsigma_{k2}}{\sum_{k=1}^{3}\alpha_k\varsigma_{k1}}\frac{P}{\beta_3\varsigma_{32}} - \frac{2/R}{\sum_{k=1}^{3}\alpha_k\varsigma_{k1}}\right] - a^{3/2}\sqrt{\frac{8\pi\eta}{-\pi\sum_{k=1}^{3}\alpha_k\varsigma_{k1}}}\left\{1 \pm \frac{1}{\sqrt{\pi}\alpha_{\mathrm{KLJ}}}\right\},
\end{aligned}
\tag{50}
$$

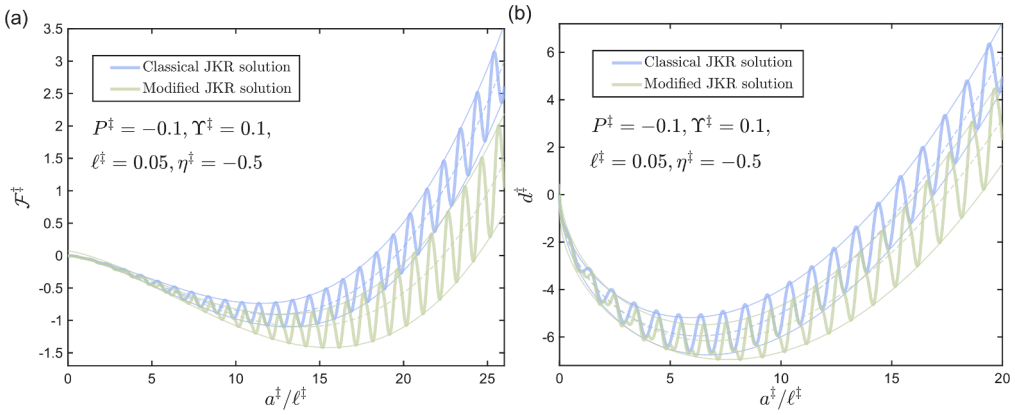


Fig. 8. Envelope curves for adhesive incremental indentation response based on the classical and modified JKR models. (a) presents the envelope curves for non-dimensional incremental indentation forces, while (b) presents the envelope curves for non-dimensional indentation depth. The thin solid lines on the outer contour represent the upper and lower envelopes. The dashed line in the middle is the adhesive incremental indentation response that neglects surface topography. The thick solid line corresponds to the solution curve.

where $\alpha_{\mathrm{KLJ}} := \sqrt{2\ell\eta\left(-\pi\sum_{k=1}^{3}\alpha_k\varsigma_{k1}\right)}/(\pi\Upsilon)$ denotes the parameter introduced by Johnson (1995) for the JKR adhesion of a nominally flat contact that has a single scale sinusoidal waviness. A key threshold is given by $\alpha_{\mathrm{KLJ}} = 1/\sqrt{\pi}$. This corresponds exactly to the condition under which a sinusoidal waviness flattens completely on its own without any external load. For a sinusoidal contact, if $\alpha_{\mathrm{KLJ}} > 1/\sqrt{\pi}$, the surfaces come into full contact instantly. Conversely, if $\alpha_{\mathrm{KLJ}} < 1/\sqrt{\pi}$, a certain level of pressure is required to attain full contact. Nevertheless, the consideration of small scale surface topography in the modified surface energy in Eqs. (47) and (48) introduces additional oscillation to incremental indentation response, which necessitates new envelope curves as

$$
\begin{aligned}
d^\ddagger_{\mathrm{env}} &= \frac{(a^\ddagger)^2}{\ell^\ddagger} - \frac{\sqrt{-\eta^\ddagger a^\ddagger}}{\ell^\ddagger}\sqrt[4]{1+(a^\ddagger)^2} \pm \mathrm{Envelope}\left[\pi^2\Upsilon^\ddagger\frac{a^\ddagger}{\ell^\ddagger}\widehat{H}_0\left(2\pi\frac{a^\ddagger}{\ell^\ddagger}\right)\right.\\
&\left. - \frac{\sqrt{-\eta^\ddagger a^\ddagger}}{\ell^\ddagger}\left(\sqrt[4]{1+[a^\ddagger+2\pi\Upsilon^\ddagger\sin(2\pi a^\ddagger/\ell^\ddagger)]^2} - \sqrt[4]{1+(a^\ddagger)^2}\right)\right],\\
\mathcal{F}^\ddagger_{\mathrm{env}} &= \frac{16}{9\eta^\ddagger}(P^\ddagger-1)(a^\ddagger)^3 - \frac{8}{3}\frac{(a^\ddagger)^{3/2}}{\sqrt{-\eta^\ddagger}}\sqrt[4]{1+(a^\ddagger)^2} \pm \mathrm{Envelope}\left\{\frac{4\pi}{3\eta^\ddagger}\Upsilon^\ddagger a^\ddagger\left[\ell^\ddagger\widehat{H}_1\left(2\pi\frac{a^\ddagger}{\ell^\ddagger}\right) - 2\pi a^\ddagger\widehat{H}_0\left(2\pi\frac{a^\ddagger}{\ell^\ddagger}\right)\right]\right.\\
&\left. - \frac{8}{3}\frac{(a^\ddagger)^{3/2}}{\sqrt{-\eta^\ddagger}}\left(\sqrt[4]{1+[a^\ddagger+2\pi\Upsilon^\ddagger\sin(2\pi a^\ddagger/\ell^\ddagger)]^2} - \sqrt[4]{1+(a^\ddagger)^2}\right)\right\},
\end{aligned}
\tag{51}
$$

where $d^\ddagger_{\mathrm{env}} := d_{\mathrm{env}}/\ell$ and Envelope[#] is an envelope function. Fig. 8 shows the envelope curves for classical and modified JKR solutions. Through numerical investigation, we find that in the modified JKR model, the presence of irregular periodic oscillations causes the upper and lower envelope curves not to be perfectly symmetric about the dashed line. Therefore, an envelope function presented in Eq. (51) is designed to numerically capture peaks of envelope curves.

For the film-substrate system with a wavy surface, the solution can be obtained by simply modifying $W(\rho,\phi)$ in Eq. (C.4) and following the same procedure. The details are omitted here for brevity. Generally, the indentation response induced by adhesion becomes increasingly suppressed as the substrate stiffness increases (Xia et al., 2023). This observation also allows us to tune the interfacial strength through modulating the substrate stiffness.

In addition, we note that for a hyperelastic material with an initially flattened surface, application of pre-stretching beyond a critical threshold can trigger surface instability, resulting in waviness. In the three-dimensional case of equi-biaxial stretching, the wavy surface is usually characterized by Bessel functions rather than the sinusoidal ones, as shown in Appendix F. After the onset of surface instability, indentation on the wavy surface may affect the instability modes, even leading to a snap through behavior. However, we simply disregard these complexities and assume that the surface displacement within the contact area takes the form $W(\rho) = d - f(\rho) = d - \{\rho^2/(2R) + \Upsilon[1 - \widehat{J}_0(\mathfrak{V}\rho)]\}$. The property that $f(\rho)$ is monotonically increasing implies that $1/(R\Upsilon\mathfrak{V}^2) > -\widehat{J}_1(\mathfrak{V}\rho)/(\mathfrak{V}\rho)$ should be fulfilled when $\rho > 0$, where Υ is the amplitude of the waviness, $\mathfrak{V}$ corresponds to the radial characteristic wavenumber, and $\widehat{J}_v(\#)$ denotes the Bessel function of the first kind. Following the same boundary conditions and derivation approach as in Eqs. (34)–(36), we have

$$
\omega_1(\rho) = \frac{1}{\pi^2\sum_{k=1}^{3}\alpha_k\varsigma_{k1}}\left\{\frac{d - \frac{a^2}{R} - \Upsilon[1-\cos(\mathfrak{V}a)]}{\sqrt{a^2-\rho^2}} + \left(\frac{2}{R} - \frac{P\sum_{k=1}^{3}\alpha_k\varsigma_{k2}}{\beta_3\varsigma_{32}}\right)\sqrt{a^2-\rho^2} + \Upsilon\mathfrak{V}\int_\rho^a \frac{\sin(\mathfrak{V}t)}{\sqrt{t^2-\rho^2}}\mathrm{d}t\right\},
\tag{52}
$$

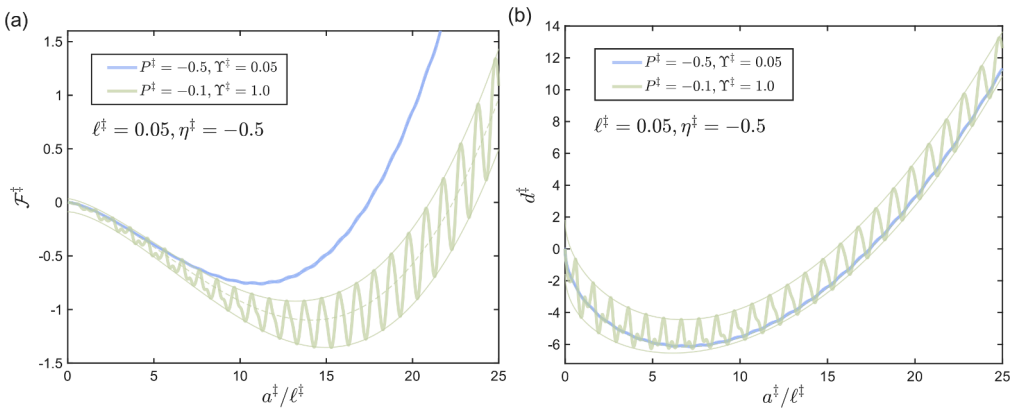


Fig. 9. Adhesive incremental indentation response under the modified JKR framework, where the wavy surface is described by a Bessel function. (a) and (b) present the non-dimensional incremental indentation force and indentation depth versus the non-dimensional contact radius, respectively. $\mathfrak{V}^\ddagger$ is defined as $\mathfrak{V}^\ddagger := 2\pi/(\mathfrak{V}R)$, which is identical to $\ell^\ddagger$.

where $\int_0^t \rho_0 \widehat{J}_0(\mathfrak{V}\rho_0)/\sqrt{t^2-\rho_0^2}\mathrm{d}\rho_0 = \sin(\mathfrak{V}t)/\mathfrak{V}$, $d = a^2/R + \Upsilon[1-\cos(\mathfrak{V}a)]$, and

$$\mathcal{F}(a) = \frac{2a^3}{3\pi}\left[\frac{\sum_{k=1}^3 \alpha_k\varsigma_{k2}}{\sum_{k=1}^3 \alpha_k\varsigma_{k1}}\frac{P}{\beta_3\varsigma_{32}} - \frac{2/R}{\sum_{k=1}^3 \alpha_k\varsigma_{k1}}\right] + \frac{2\Upsilon}{\pi\sum_{k=1}^3 \alpha_k\varsigma_{k1}}\left[a\cos(\mathfrak{V}a) - \frac{\sin(\mathfrak{V}a)}{\mathfrak{V}}\right]. \tag{53}$$

Upon additionally incorporating adhesive contact that complies with the modified JKR adhesion theory, we find

$$d = \frac{a^2}{R} + \Upsilon[1-\cos(\mathfrak{V}a)] + \sum_{k=1}^3 \alpha_k\varsigma_{k1}\sqrt{-\frac{2\eta\pi^2 a\sqrt{1+[a/R+\Upsilon\mathfrak{V}\widehat{J}_1(\mathfrak{V}a)]^2}}{\sum_{k=1}^3 \alpha_k\varsigma_{k1}}} \tag{54}$$

and

$$\begin{aligned}\mathcal{F}(a) = {} & \frac{2a^3}{3\pi}\left[\frac{\sum_{k=1}^3 \alpha_k\varsigma_{k2}}{\sum_{k=1}^3 \alpha_k\varsigma_{k1}}\frac{P}{\beta_3\varsigma_{32}} - \frac{2/R}{\sum_{k=1}^3 \alpha_k\varsigma_{k1}}\right] + \frac{2\Upsilon}{\pi\sum_{k=1}^3 \alpha_k\varsigma_{k1}}\left[a\cos(\mathfrak{V}a) - \frac{\sin(\mathfrak{V}a)}{\mathfrak{V}}\right] \\ & - \frac{2}{\pi}\sqrt{-\frac{2\eta\pi^2 a^3\sqrt{1+[a/R+\Upsilon\mathfrak{V}\widehat{J}_1(\mathfrak{V}a)]^2}}{\sum_{k=1}^3 \alpha_k\varsigma_{k1}}},\end{aligned} \tag{55}$$

where $\mathrm{d}\widehat{J}_0(\rho)/\mathrm{d}\rho = -\widehat{J}_1(\rho)$ is adopted. The adhesive incremental indentation response that satisfies the monotonicity condition $1/R\Upsilon\mathfrak{V}^2 > 0.06614$ (blue) and that which does not (green) are depicted in Fig. 9. The green dashed line is identical to the one shown in Fig. 8 to enable comparison. We also observe that the irregular periodic oscillation occurs again under incipient contact.

4.3. Viscoelastic adhesive contact

Viscoelasticity is essential in adhesive contact of soft materials, since the pull-off force measured experimentally is highly sensitive to loading/unloading rate and temperature. In polymers, elastomers, and gels, detachment is controlled not only by the work of adhesion, but also by rate-dependent energy dissipation near the moving contact edge (Argatov et al., 2023). Therefore, the apparent adhesion obtained from experimental contact tests usually differs from the equilibrium interfacial adhesion. Following the assumptions and derivations in Ciavarella and Papangelo (2021), we adopt the definition of the effective work of adhesion according to the Gent-Schultz model, i.e., $\eta_{\mathrm{eff}} = \eta[1+\mathfrak{g}(\mathfrak{a}_\Theta\check{v}_{\mathrm{ce}})^n]$, where $\mathfrak{g}$ is a dimensionless dissipation parameter, $\mathfrak{a}_\Theta$ is the Williams-Landel-Ferry factor at temperature Θ, $\check{v}_{\mathrm{ce}}$ represents the velocity of the contact edge, and n is the exponent. Here, the ratio η_{eff}/η remains larger than one reflects the energy dissipation induced by viscoelasticity. The velocity of the contact edge can then be expressed in terms of the indenter velocity $\check{v}_{\mathrm{in}} := -\mathrm{d}d/\mathrm{d}t$ as $\check{v}_{\mathrm{ce}} := -\mathrm{d}a/\mathrm{d}t = \check{v}_{\mathrm{in}}\mathrm{d}a/\mathrm{d}d$. With the effective energy release rate $G_{\mathrm{eff}}(a) = \eta_{\mathrm{eff}}\sqrt{1+[f'(a)]^2}$ and using Eq. (47), we arrive at

$$\frac{\mathrm{d}a}{\mathrm{d}d} = \frac{1}{\mathfrak{g}^{1/n}\mathfrak{a}_\Theta\check{v}_{\mathrm{in}}}\left[\frac{\eta_{\mathrm{eff}}\sqrt{1+[f'(a)]^2}}{\eta\sqrt{1+[f'(a)]^2}} - 1\right]^{\frac{1}{n}} = \frac{1}{\mathfrak{g}^{1/n}\mathfrak{a}_\Theta\check{v}_{\mathrm{in}}}\left\{\frac{\left[\frac{a^2}{R} + \Upsilon\frac{\pi^2 a}{\ell}\widehat{H}_0\left(\frac{2\pi a}{\ell}\right) - d(a)\right]^2}{2\pi a\left(-\pi\sum_{k=1}^3 \alpha_k\varsigma_{k1}\right)\eta\sqrt{1+[f'(a)]^2}} - 1\right\}^{\frac{1}{n}}, \tag{56}$$

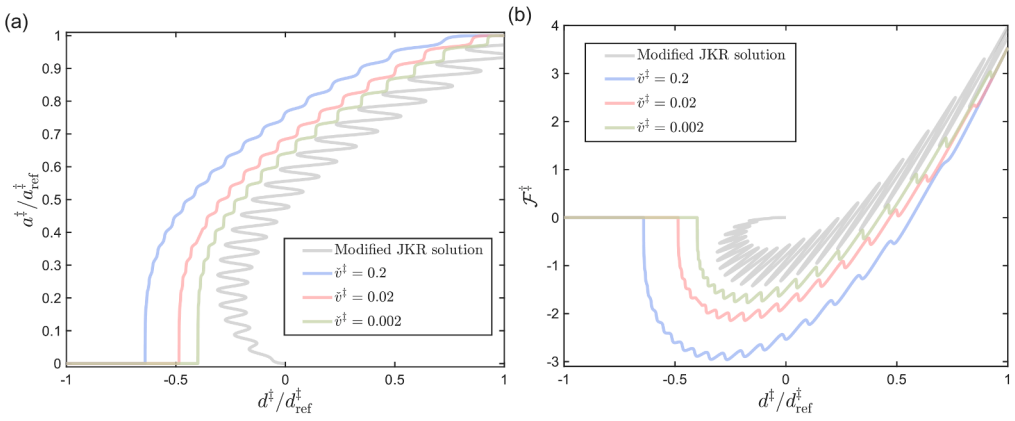


Fig. 10. Rate-dependent incremental indentation response. Based on the modified JKR model, (a) and (b) respectively display the contact radius and the incremental indentation force as functions of the indentation depth, at various velocities of the indenter. To allow direct comparison, the curves adopt parameters that are identical to those in Ciavarella and Papangelo (2021), given by $n = 0.330$, $\Upsilon^\ddagger = 0.005$, $\ell^\ddagger = 0.002$, $\eta^\ddagger = -1.325 \times 10^{-5}$, $P^\ddagger = -1.0 \times 10^{-4}$, $a^\ddagger_{\rm ref} = 0.04348$, $d^\ddagger_{\rm ref} = 1.045 \times 10^{-3}$.

where $f(a)$ is the axisymmetric indenter profile function at $\rho = a$. If we denote $\check{v}^\ddagger := \mathfrak{g}^{1/n}\mathfrak{a}_\Theta \check{v}_{\rm in}$ and take $f(a)$ to be the same as that in Eq. (46), the non-dimensional differential equation is derived as

$$\frac{{\rm d}a^\ddagger}{{\rm d}d^\ddagger} = \frac{\ell^\ddagger}{\check{v}^\ddagger}\left\{\frac{[(a^\ddagger)^2 + \pi^2\Upsilon^\ddagger a^\ddagger \widehat{H}_0(2\pi a^\ddagger/\ell^\ddagger) - d^\ddagger\ell^\ddagger]^2}{-\eta^\ddagger a^\ddagger\sqrt{1 + [a^\ddagger + 2\pi\Upsilon^\ddagger \sin(2\pi a^\ddagger/\ell^\ddagger)]^2}} - 1\right\}^{\frac{1}{n}}, \tag{57}$$

from which we can obtain $a^\ddagger - d^\ddagger$ relation numerically. Substituting this relation into

$$\mathcal{F}^\ddagger = \frac{16}{9\eta^\ddagger}(P^\ddagger - 1)(a^\ddagger)^3 + \frac{4\pi}{3\eta^\ddagger}\Upsilon^\ddagger a^\ddagger\left[\ell^\ddagger \widehat{H}_1\left(2\pi\frac{a^\ddagger}{\ell^\ddagger}\right) - 2\pi a^\ddagger \widehat{H}_0\left(2\pi\frac{a^\ddagger}{\ell^\ddagger}\right)\right] - \frac{8a^\ddagger}{3\eta^\ddagger}\left[d^\ddagger\ell^\ddagger - (a^\ddagger)^2 - \pi^2\Upsilon^\ddagger a^\ddagger \widehat{H}_0\left(2\pi\frac{a^\ddagger}{\ell^\ddagger}\right)\right] \tag{58}$$

yields the $\mathcal{F}^\ddagger - d^\ddagger$ relation. As illustrated in Fig. 10, the viscoelastic indentation response is delayed relative to the elastic response, and the delay grows with increasing indenter velocity. In addition, the viscoelastic peeling process ends only when the contact radius reaches zero, rather than at the critical JKR unstable radius. In contrast to the classical JKR model, the modified JKR model introduces irregular periodic oscillation in the indentation response under incipient contact.

5. Conclusions

This article has established a systematic analytical framework for solving thermoelastic contact problems in pre-deformed hyperelastic materials under incremental loading. Based on the updated Lagrangian formulation, the incremental governing equations were derived and subsequently reduced to a set of quasi-harmonic equations according to the generalized Almansi's theorem. The potential theory method was developed to construct single-layer potentials, allowing explicit inversion of the integro-differential equations that arise from the contact boundary conditions. For a rigid indenter in frictionless contact with a hyperelastic half-space, closed-form expressions for the incremental displacement, temperature, stress fields, and indentation force were obtained and validated by finite element simulations, demonstrating excellent agreement for sufficiently small perturbations. Under the prescribed boundary conditions, the incremental surface displacement within the contact area is governed solely by the geometric compatibility condition and is independent of the thermal field, whereas thermal effects manifest primarily in the stress response. This framework was further extended to a hyperelastic film bonded to a rigid smooth substrate via the generalized image method, where Fredholm integral equations of the second kind were derived and shown to be contractive, enabling an iterative solution procedure. The contraction property of the integral operators guarantees the convergence of the iterative scheme according to the Banach-Caccioppoli theorem, providing a practical pathway for approximating the potential densities. Adhesive contact on a wavy surface was also analyzed by introducing an energy release rate criterion, leading to an extended JKR-type relation that incorporates thermal effects, pre-deformation, and surface topography. The modified JKR solution reveals that pre-stretch can modulate the equivalent modulus, equivalent inverse temperature, and surface waviness, thereby enabling tunable interface strength. The analytical solutions derived herein not only incorporate adhesive interactions and thermal effects but also offer a benchmark for numerical methods. While the incremental formulation assumes small perturbations superimposed on a finite biasing field, the framework can be extended to larger indentation depths through a multi-step incremental procedure. When the indentation depth becomes sufficiently large, the Shuttleworth effect should be considered, as the large surface strain within the contact area may lead to an appreciable change in surface energy (Heyden and Bain, 2024). Therefore, the established model should be refined by incorporating surface elasticity.

Beyond the analytical treatments, a computational investigation was performed for wavy surfaces induced by surface instability. A total Lagrangian formulation was adopted to obtain the nonlinear solution, followed by a linearized buckling analysis to identify critical load factors and buckling modes. The imperfection-induced wavy configuration was then used as the reference state for subsequent contact analysis using the augmented Lagrangian method. This approach provides a robust tool for studying the interplay among finite deformation, surface instability, contact, and adhesion. Overall, this work establishes a comprehensive theoretical and computational foundation for understanding thermoelastic contact in soft materials under finite deformation, with direct applications in nanoimprint lithography, surface metrology, and precision manufacturing. In addition, the thermoelastic model and the volumetric growth model share a highly similar mathematical structure within the framework of continuum mechanics (Rodriguez et al., 1994). Hence, the present model can also be extended to analyze biological growth through contact interactions.

CRediT authorship contribution statement

Lizichen Chen: Writing – original draft, Validation, Methodology, Investigation, Funding acquisition, Conceptualization; **Yangkun Du:** Writing – review & editing, Conceptualization; **Yafei Wang:** Writing – review & editing, Conceptualization; **Zhanfeng Li:** Writing – review & editing, Conceptualization; **Zihao Du:** Writing – review & editing, Conceptualization; **Zhuangzhuang He:** Writing – review & editing, Conceptualization; **Rongqiao Xu:** Writing – review & editing, Conceptualization; **Michel Destrade:** Writing – review & editing; **Gangfeng Wang:** Writing – review & editing, Conceptualization; **C.W. Lim:** Writing – review & editing, Conceptualization; **Weiqiu Chen:** Writing – review & editing, Supervision, Funding acquisition, Conceptualization.

Declaration of competing interest

The authors declare that they have no known competing financial interests or personal relationships that could have appeared to influence the work reported in this paper.

Acknowledgment

The work was supported by the National Natural Science Foundation of China (Nos. 125B2042, 12192211 and 12192210), the 111 Project, PR China (No. B21034), the China Association for Science and Technology Young Elite Scientist Sponsorship Program (Doctoral Student Special Plan), the Qiushi Rising Star Program of Zhejiang University, Hangzhou, Zhejiang Province, the Open Foundation of the State Key Laboratory of Fluid Power and Mechatronic Systems, and the specialized research projects of Huanjiang Laboratory, Zhuji, Zhejiang Province.

Data availability

No data was used for the research described in the article.

Appendix A. Parameters and recurrence relations

Eq. (5) can be expanded to read

$$\begin{aligned}
\mathrm{A}_{0jigk} = {} & 4J_e^{-1}\Big\{\Omega_{11}[\mathrm{b}_e]_{ji}[\mathrm{b}_e]_{gk} + \Omega_{22}\Big(I_1[\mathrm{b}_e]_{ji} - [\mathrm{b}_e]_{js}[\mathrm{b}_e]_{si}\Big)\Big(I_1[\mathrm{b}_e]_{gk} - [\mathrm{b}_e]_{gs}[\mathrm{b}_e]_{sk}\Big) + I_3^2\Omega_{33}\delta_{ji}\delta_{gk} \\
& + \Omega_{12}\Big[[\mathrm{b}_e]_{ji}\Big(I_1[\mathrm{b}_e]_{gk} - [\mathrm{b}_e]_{gs}[\mathrm{b}_e]_{sk}\Big) + \Big(I_1[\mathrm{b}_e]_{ji} - [\mathrm{b}_e]_{js}[\mathrm{b}_e]_{si}\Big)[\mathrm{b}_e]_{gk}\Big] + I_3\Omega_{13}\Big([\mathrm{b}_e]_{ji}\delta_{gk} + \delta_{ji}[\mathrm{b}_e]_{gk}\Big) \\
& + I_3\Omega_{23}\Big[\Big(I_1[\mathrm{b}_e]_{ji} - [\mathrm{b}_e]_{js}[\mathrm{b}_e]_{si}\Big)\delta_{gk} + \delta_{ji}\Big(I_1[\mathrm{b}_e]_{gk} - [\mathrm{b}_e]_{gs}[\mathrm{b}_e]_{sk}\Big)\Big]\Big\} + 2J_e^{-1}\Big\{\Omega_1\delta_{ik}[\mathrm{b}_e]_{jg} \\
& + \Omega_2\Big(2[\mathrm{b}_e]_{ji}[\mathrm{b}_e]_{gk} - [\mathrm{b}_e]_{gi}[\mathrm{b}_e]_{jk} + I_1\delta_{ik}[\mathrm{b}_e]_{jg} - [\mathrm{b}_e]_{ik}[\mathrm{b}_e]_{jg} - \delta_{ik}[\mathrm{b}_e]_{js}[\mathrm{b}_e]_{sg}\Big) + I_3\Omega_3(2\delta_{ji}\delta_{gk} - \delta_{jk}\delta_{gi})\Big\},
\end{aligned} \tag{A.1}$$

$$\begin{aligned}
\mathrm{M}_{0ji} = {} & 4J_e^{-1}\kappa_{c\alpha}[\mathrm{F}_\theta^{-1}]_{\alpha b}\Big\{\Omega_{11}[\mathrm{b}_e]_{ji}[\mathrm{C}_e]_{cb} + \Omega_{22}\Big(I_1[\mathrm{b}_e]_{ji} - [\mathrm{b}_e]_{js}[\mathrm{b}_e]_{si}\Big)(I_1[\mathrm{C}_e]_{cb} - [\mathrm{C}_e]_{ch}[\mathrm{C}_e]_{hb}) + I_3^2\Omega_{33}\delta_{ji}\delta_{cb} \\
& + \Omega_{12}\Big[[\mathrm{b}_e]_{ji}(I_1[\mathrm{C}_e]_{cb} - [\mathrm{C}_e]_{ch}[\mathrm{C}_e]_{hb}) + \Big(I_1[\mathrm{b}_e]_{ji} - [\mathrm{b}_e]_{js}[\mathrm{b}_e]_{si}\Big)[\mathrm{C}_e]_{cb}\Big] + I_3\Omega_{13}\Big([\mathrm{b}_e]_{ji}\delta_{cb} + \delta_{ji}[\mathrm{C}_e]_{cb}\Big) \\
& + I_3\Omega_{23}\Big[\Big(I_1[\mathrm{b}_e]_{ji} - [\mathrm{b}_e]_{js}[\mathrm{b}_e]_{si}\Big)\delta_{cb} + \delta_{ji}(I_1[\mathrm{C}_e]_{cb} - [\mathrm{C}_e]_{ch}[\mathrm{C}_e]_{hb})\Big]\Big\} + 2J_e^{-1}\kappa_{c\alpha}[\mathrm{F}_\theta^{-1}]_{\alpha b}\Big\{\Omega_1[\mathrm{F}_e]_{jb}[\mathrm{F}_e]_{ic} \\
& + \Omega_2\Big(2[\mathrm{b}_e]_{ji}[\mathrm{C}_e]_{cb} - [\mathrm{F}_e]_{kc}[\mathrm{F}_e]_{ib}[\mathrm{b}_e]_{jk} + I_1[\mathrm{F}_e]_{jb}[\mathrm{F}_e]_{ic} - [\mathrm{b}_e]_{ik}[\mathrm{F}_e]_{jb}[\mathrm{F}_e]_{kc} - [\mathrm{C}_e]_{ab}[\mathrm{F}_e]_{ja}[\mathrm{F}_e]_{ic}\Big) \\
& + I_3\Omega_3\Big(2\delta_{ji}\delta_{cb} - [\mathrm{F}_e]_{jc}[\mathrm{F}_e^{-1}]_{bi}\Big)\Big\} + 2J_e^{-1}[\mathrm{F}_e]_{ja}(\kappa_{a\alpha}[\mathrm{F}_\theta^{-1}]_{\alpha b} - \kappa_{c\alpha}[\mathrm{F}_\theta^{-1}]_{\alpha c}\delta_{ab})\{\Omega_1[\mathrm{F}_e]_{ib} \\
& + \Omega_2(I_1[\mathrm{F}_e]_{ib} - [\mathrm{C}_e]_{bc}[\mathrm{F}_e]_{ic}) + I_3\Omega_3[\mathrm{F}_e^{-1}]_{bi}\}.
\end{aligned} \tag{A.2}$$

Therefore, the parameters involved in Eq. (4) are expressed as

$$
\begin{aligned}
\mathrm{A}_{01111} &= 4\lambda_1^2\lambda_3^{-1}\left\{\Omega_{11}+\Omega_{22}(\lambda_1^2+\lambda_3^2)^2+\Omega_{33}\lambda_1^4\lambda_3^4+2\Omega_{12}\left(\lambda_1^2+\lambda_3^2\right)+2\Omega_{13}\lambda_1^2\lambda_3^2+2\Omega_{23}\lambda_1^2\lambda_3^2(\lambda_1^2+\lambda_3^2)\right\}\\
&\quad+2\lambda_3^{-1}\{\Omega_1+\Omega_2(\lambda_1^2+\lambda_3^2)+\Omega_3\lambda_1^2\lambda_3^2\},\\
\mathrm{A}_{01122} &= 4\lambda_1^2\lambda_3^{-1}\left\{\Omega_{11}+\Omega_{22}(\lambda_1^2+\lambda_3^2)^2+\Omega_{33}\lambda_1^4\lambda_3^4+2\Omega_{12}\left(\lambda_1^2+\lambda_3^2\right)+2\Omega_{13}\lambda_1^2\lambda_3^2+2\Omega_{23}\lambda_1^2\lambda_3^2(\lambda_1^2+\lambda_3^2)\right\}+4\lambda_1^2\lambda_3^{-1}\{\Omega_2+\Omega_3\lambda_3^2\},\\
\mathrm{A}_{01133} &= 4\lambda_3\left\{\Omega_{11}+2\Omega_{22}\lambda_1^2(\lambda_1^2+\lambda_3^2)+\Omega_{33}\lambda_1^6\lambda_3^2+\Omega_{12}\left(3\lambda_1^2+\lambda_3^2\right)+\Omega_{13}\lambda_1^2(\lambda_1^2+\lambda_3^2)+\Omega_{23}\lambda_1^4(\lambda_1^2+3\lambda_3^2)\right\}+4\lambda_3\{\Omega_2+\Omega_3\lambda_1^2\},\\
\mathrm{A}_{03333} &= 4\lambda_1^{-2}\lambda_3^3\{\Omega_{11}+4\Omega_{22}\lambda_1^4+\Omega_{33}\lambda_1^8+4\Omega_{12}\lambda_1^2+2\Omega_{13}\lambda_1^4+4\Omega_{23}\lambda_1^6\}+2\lambda_1^{-2}\lambda_3\{\Omega_1+2\Omega_2\lambda_1^2+\Omega_3\lambda_1^4\},\\
\mathrm{A}_{01212} &= 2\lambda_3^{-1}(\Omega_1+\Omega_2\lambda_3^2),\\
\mathrm{A}_{01221} &= -2\lambda_1^2\lambda_3^{-1}(\Omega_2+\Omega_3\lambda_3^2),\\
\mathrm{A}_{01313} &= 2\lambda_3^{-1}(\Omega_1+\Omega_2\lambda_1^2),\\
\mathrm{A}_{01331} &= -2\lambda_3(\Omega_2+\Omega_3\lambda_1^2),\\
\mathrm{A}_{03131} &= 2\lambda_1^{-2}\lambda_3(\Omega_1+\Omega_2\lambda_1^2),
\end{aligned}
\tag{A.3}
$$

$$
\begin{aligned}
\mathrm{M}_{011} &= 4\lambda_3^{-1}\left\{\Omega_{11}(2\lambda_1^2\hat{\kappa}_1+\lambda_3^2\hat{\kappa}_3)+2\Omega_{22}\lambda_1^2(\lambda_1^2+\lambda_3^2)\left[(\lambda_1^2+\lambda_3^2)\hat{\kappa}_1+\lambda_3^2\hat{\kappa}_3\right]+\Omega_{33}\lambda_1^6\lambda_3^4(2\hat{\kappa}_1+\hat{\kappa}_3)+\Omega_{12}[4\lambda_1^2(\lambda_1^2+\lambda_3^2)\hat{\kappa}_1\right.\\
&\quad+\lambda_3^2(3\lambda_1^2+\lambda_3^2)\hat{\kappa}_3]+\Omega_{13}\lambda_1^2\lambda_3^2\left[4\lambda_1^2\hat{\kappa}_1+\left(\lambda_1^2+\lambda_3^2\right)\hat{\kappa}_3\right]+\Omega_{23}\lambda_1^4\lambda_3^2[4(\lambda_1^2+\lambda_3^2)\hat{\kappa}_1+(\lambda_1^2+3\lambda_3^2)\hat{\kappa}_3]\Big\}+2\lambda_3^{-1}\{\Omega_1\hat{\kappa}_1\\
&\quad+3\Omega_2(\lambda_1^2\hat{\kappa}_1+\lambda_3^2\hat{\kappa}_3)+\Omega_3\lambda_1^2\lambda_3^2(3\hat{\kappa}_1+2\hat{\kappa}_3)\}-2\lambda_3^{-1}(\hat{\kappa}_1+\hat{\kappa}_3)\{\Omega_1+\Omega_2(\lambda_1^2+\lambda_3^2)+\Omega_3\lambda_1^2\lambda_3^2\},\\
\mathrm{M}_{033} &= 4\lambda_1^{-2}\lambda_3\left\{\Omega_{11}(2\lambda_1^2\hat{\kappa}_1+\lambda_3^2\hat{\kappa}_3)+4\Omega_{22}\lambda_1^4[(\lambda_1^2+\lambda_3^2)\hat{\kappa}_1+\lambda_3^2\hat{\kappa}_3]+\Omega_{33}\lambda_1^8\lambda_3^2(2\hat{\kappa}_1+\hat{\kappa}_3)+2\Omega_{12}\lambda_1^2[(3\lambda_1^2+\lambda_3^2)\hat{\kappa}_1+2\lambda_3^2\hat{\kappa}_3]\right.\\
&\quad+2\Omega_{13}\lambda_1^4[(\lambda_1^2+\lambda_3^2)\hat{\kappa}_1+\lambda_3^2\hat{\kappa}_3]+2\Omega_{23}\lambda_1^6[(\lambda_1^2+3\lambda_3^2)\hat{\kappa}_1+2\lambda_3^2\hat{\kappa}_3]\Big\}+2\lambda_1^{-2}\lambda_3\{\Omega_1\hat{\kappa}_3+2\Omega_2\lambda_1^2(2\hat{\kappa}_1+\hat{\kappa}_3)+\Omega_3\lambda_1^4(4\hat{\kappa}_1+\hat{\kappa}_3)\}\\
&\quad-4\lambda_1^{-2}\lambda_3\hat{\kappa}_1\{\Omega_1+2\Omega_2\lambda_1^2+\Omega_3\lambda_1^4\},
\end{aligned}
\tag{A.4}
$$

where $\hat{\kappa}_i := \kappa_i/[1+\kappa_i(\Theta-\Theta_{\mathrm{ref}})](i=1,3)$.

The roots of the biquadratic equation $\hbar_0 s^4-\hbar_1 s^2+\hbar_2=0$ are given by $s_{1,2}^2=\left(\hbar_1\pm\sqrt{\hbar_1^2-4\hbar_0\hbar_2}\right)/(2\hbar_0)$. α_k and $\beta_k(k=1,2,3)$ in Eq. (12) are in the form of

$$
\alpha_k=\frac{\left[\mathrm{M}_{011}\left(\mathrm{A}_{01133}+\mathrm{A}_{01331}\right)-\mathrm{M}_{033}\mathrm{A}_{01111}+\mathrm{M}_{033}\mathrm{A}_{03131}s_k^2\right]s_k}{\left[\mathrm{M}_{033}\left(\mathrm{A}_{01133}+\mathrm{A}_{01331}\right)-\mathrm{M}_{011}\mathrm{A}_{03333}\right]s_k^2+\mathrm{M}_{011}\mathrm{A}_{01313}},
\tag{A.5}
$$

$$
\begin{aligned}
\beta_k &= \frac{\mathrm{A}_{01111}\mathrm{A}_{01313}-\left[\mathrm{A}_{01111}\mathrm{A}_{03333}+\mathrm{A}_{03131}\mathrm{A}_{01313}-\left(\mathrm{A}_{01133}+\mathrm{A}_{01331}\right)^2\right]s_k^2+\mathrm{A}_{03131}\mathrm{A}_{03333}s_k^4}{\left[\mathrm{M}_{033}\left(\mathrm{A}_{01133}+\mathrm{A}_{01331}\right)-\mathrm{M}_{011}\mathrm{A}_{03333}\right]s_k^2+\mathrm{M}_{011}\mathrm{A}_{01313}}\\
&= \frac{\hbar_2-\hbar_1 s_k^2+\hbar_0 s_k^4}{\left[\mathrm{M}_{033}\left(\mathrm{A}_{01133}+\mathrm{A}_{01331}\right)-\mathrm{M}_{011}\mathrm{A}_{03333}\right]s_k^2+\mathrm{M}_{011}\mathrm{A}_{01313}}.
\end{aligned}
\tag{A.6}
$$

The recurrence relations between the combination coefficients (presented in Eq. (C.2)) are derived as

$$
\sum_{k=1}^{3}\varpi_{1k}[1+\varsigma_{ki(+)}^{\{000\}}+\varsigma_{ki(-)}^{\{000\}}]=0,\quad \sum_{k=1}^{3}\varpi_{1k}[\varsigma_{ki(+)}^{\{mnq\}}+\varsigma_{ki(-)}^{\{mnq\}}]=0,\quad (i=1,2)
\tag{A.7}
$$

$$
\sum_{k=1}^{3}\gamma_{1k}[1+\varsigma_{ki(+)}^{\{000\}}+\varsigma_{ki(-)}^{\{000\}}]=-\frac{\delta_{1i}}{2\pi},\quad \sum_{k=1}^{3}\gamma_{1k}[\varsigma_{ki(+)}^{\{mnq\}}-\varsigma_{ki(-)}^{\{mnq\}}]\quad=0,\quad (i=1,2)
\tag{A.8}
$$

$$
\gamma_{23}[1+\varsigma_{3i(+)}^{\{000\}}+\varsigma_{3i(-)}^{\{000\}}]\quad=-\frac{\delta_{2i}}{2\pi},\quad \gamma_{23}[\varsigma_{3i(+)}^{\{mnq\}}-\varsigma_{3i(-)}^{\{mnq\}}]=0,\quad (i=1,2)
\tag{A.9}
$$

$$
\begin{aligned}
&\varpi_{1k}[1+\varsigma_{ki(+)}^{\{000\}}+\varsigma_{ki(-)}^{\{000\}}+\varsigma_{ki(-)}^{\{(2\delta_{1k})(2\delta_{2k})(2\delta_{3k})\}}]+\sum_{j=1}^{2}\varpi_{1\mathcal{T}_{k+j}}\varsigma_{\mathcal{T}_{k+j}i(-)}^{\{(\delta_{1k}+\delta_1\mathcal{T}_{k+j})(\delta_{2k}+\delta_2\mathcal{T}_{k+j})(\delta_{3k}+\delta_3\mathcal{T}_{k+j})\}}=0,\\
&\sum_{k=1}^{3}\varpi_{1k}[\varsigma_{ki(+)}^{\{(m-\delta_{1k})(n-\delta_{2k})(q-\delta_{3k})\}}+\varsigma_{ki(-)}^{\{(m+\delta_{1k})(n+\delta_{2k})(q+\delta_{3k})\}}]=0,\qquad (k=1,2,3;i=1,2)
\end{aligned}
\tag{A.10}
$$

$$
\begin{aligned}
&\alpha_k[1+\varsigma_{ki(+)}^{\{000\}}+\varsigma_{ki(-)}^{\{000\}}+\varsigma_{ki(-)}^{\{(2\delta_{1k})(2\delta_{2k})(2\delta_{3k})\}}]+\sum_{j=1}^{2}\alpha_{\mathcal{T}_{k+j}}\varsigma_{\mathcal{T}_{k+j}i(-)}^{\{(\delta_{1k}+\delta_1\mathcal{T}_{k+j})(\delta_{2k}+\delta_2\mathcal{T}_{k+j})(\delta_{3k}+\delta_3\mathcal{T}_{k+j})\}}=0,\\
&\sum_{k=1}^{3}\alpha_k[\varsigma_{ki(+)}^{\{(m-\delta_{1k})(n-\delta_{2k})(q-\delta_{3k})\}}+\varsigma_{ki(-)}^{\{(m+\delta_{1k})(n+\delta_{2k})(q+\delta_{3k})\}}]=0,\qquad (k=1,2,3;i=1,2)
\end{aligned}
\tag{A.11}
$$

$$\gamma_{23}[1+\varsigma_{3i(+)}^{\{000\}}+\varsigma_{3i(-)}^{\{000\}}-\varsigma_{3i(-)}^{\{002\}}]=0,\quad \gamma_{23}[\varsigma_{3i(+)}^{\{mn(q-1)\}}-\varsigma_{3i(-)}^{\{mn(q+1)\}}]=0,\quad (i=1,2) \tag{A.12}$$

where $\mathcal{T}_{k+j}=k+j-3\mathcal{H}(k+j-3)$, $\mathcal{H}(x)=\begin{cases}1 & x>0\\ 0 & x\leqslant 0\end{cases}$ is the Heaviside step function, and m,n,q are not simultaneously zero.

Appendix B. Analytical solutions for various contact problems

In the contact problem defined by the boundary conditions Eq. (16), the densities take the following forms depending on the indenter profile when $P(\rho,\phi)=P$. For a conical indenter characterized by $W(\rho,\phi)=d-\cot\vartheta\rho$, where ϑ is the half of the apex angle of the cone, the solution yields

$$\omega_1=\frac{\cot\vartheta}{2\pi\sum_{k=1}^{3}\alpha_k\varsigma_{k1}}\operatorname{arccoth}\left(\frac{a}{\sqrt{a^2-\rho^2}}\right)-\frac{\sum_{k=1}^{3}\alpha_k\varsigma_{k2}}{\sum_{k=1}^{3}\alpha_k\varsigma_{k1}}\frac{P}{\pi^2\beta_3\varsigma_{32}}\sqrt{a^2-\rho^2}, \tag{B.1}$$

with $d=\pi a\cot\vartheta/2$, from which we have

$$\begin{aligned}\hat{H}_1(\rho,\phi,z_k)=\frac{1}{4}\frac{\cot\vartheta}{\sum_{k=1}^{3}\alpha_k\varsigma_{k1}}\Bigg\{&-3a[2l_1^2(a)-\rho^2]\sqrt{a^2-l_1^2(a)}+\rho^2\ln\left[\frac{l_1(a)\left[\sqrt{a^2-l_1^2(a)}+a\right]}{a[\rho^2-l_1^2(a)]\left[a-\sqrt{a^2-l_1^2(a)}\right]^2}\right]\\&-3z_k\sqrt{z_k^2+\rho^2}-\rho^2\arctan\left(\frac{z_k}{\sqrt{z_k^2+\rho^2}}\right)+2z_k^2\ln\left(z_k+\sqrt{z_k^2+\rho^2}\right)+4a^2\ln\left[\frac{a\left[a+\sqrt{a^2-l_1^2(a)}\right]}{l_1(a)}\right]\\&+\frac{4a}{l_1(a)}\sqrt{[a^2-l_1^2(a)][\rho^2-l_1^2(a)]}\arctan\left[\frac{l_1(a)}{\sqrt{\rho^2-l_1^2(a)}}\right]+2l_1^2(a)\ln\left[\frac{\left[a-\sqrt{a^2-l_1^2(a)}\right]\sqrt{\rho^2-l_1^2(a)}}{l_1(a)}\right]\\&+2\frac{a^2\rho^2}{l_1^2(a)}\ln\left[\frac{\left[a-\sqrt{a^2-l_1^2(a)}\right]\sqrt{\rho^2-l_1^2(a)}}{l_1(a)}\right]-\frac{2[l_1^4(a)+\rho^2a^2-l_1^2(a)\rho^2]}{l_1^2(a)}\ln\left[\rho\sqrt{\rho^2-l_1^2(a)}\right]\Bigg\}\\&-\frac{1}{\pi}\frac{\sum_{k=1}^{3}\alpha_k\varsigma_{k2}}{\sum_{k=1}^{3}\alpha_k\varsigma_{k1}}\frac{P}{\beta_3\varsigma_{32}}\Bigg\{\frac{\sqrt{[a^2-l_1^2(a)][\rho^2-l_1^2(a)]}}{6l_1(a)}(2z_k^2+6a^2-3\rho^2)\arcsin\left[\frac{l_1(a)}{\rho}\right]\\&-\frac{2a^3}{3}\ln\left[\frac{l_1(a)}{a\left(a+\sqrt{a^2-l_1^2(a)}\right)}\right]-\frac{\sqrt{a^2-l_1^2(a)}}{18}[5l_1^2(a)-9\rho^2+16a^2+6z_k^2]\Bigg\}.\end{aligned} \tag{B.2}$$

The incremental indentation force is obtained as

$$\mathcal{F}(a)=\frac{\sum_{k=1}^{3}\alpha_k\varsigma_{k2}}{\sum_{k=1}^{3}\alpha_k\varsigma_{k1}}\frac{2Pa^3}{3\pi\beta_3\varsigma_{32}}-\frac{\cot\vartheta}{\sum_{k=1}^{3}\alpha_k\varsigma_{k1}}\frac{a^2}{2}. \tag{B.3}$$

For a spherical indenter with $W(\rho,\phi)=d-\rho^2/(2R)$, where R is the radius of the sphere, we obtain

$$\omega_1=\frac{1}{\pi^2}\left(\frac{1}{\sum_{k=1}^{3}\alpha_k\varsigma_{k1}}\frac{2}{R}-\frac{\sum_{k=1}^{3}\alpha_k\varsigma_{k2}}{\sum_{k=1}^{3}\alpha_k\varsigma_{k1}}\frac{P}{\beta_3\varsigma_{32}}\right)\sqrt{a^2-\rho^2}, \tag{B.4}$$

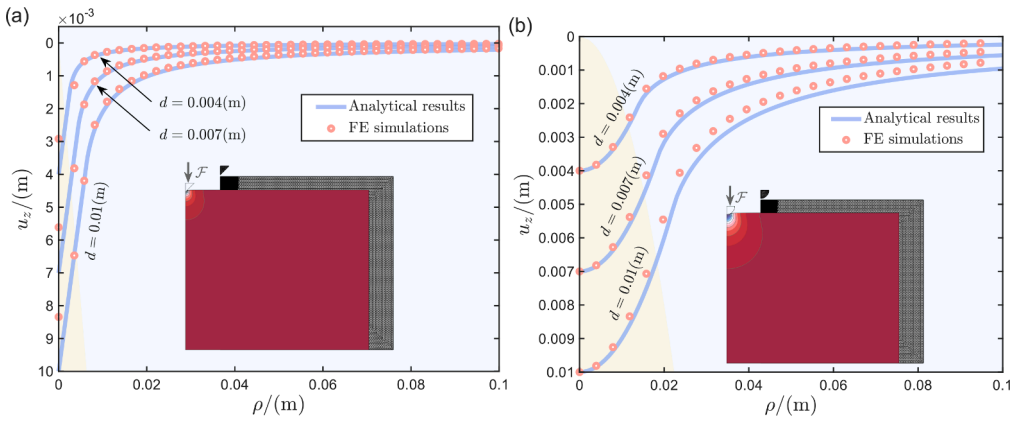


Fig. B.11. Comparison between FE simulations and analytical solutions derived for the case of (a) conical and (b) spherical indenters, where $\vartheta = \pi/4$ and $R = 0.05$(m). We adopt the same parameter values as those in Fig. 4.

with $d = a^2/R$, from which we can establish the potential function as

$$\hat{H}_1(\rho,\phi,z_k) = \frac{1}{\pi}\left(\frac{1}{\sum_{k=1}^3 \alpha_k\varsigma_{k1}}\frac{2}{R} - \frac{\sum_{k=1}^3 \alpha_k\varsigma_{k2}}{\sum_{k=1}^3 \alpha_k\varsigma_{k1}}\frac{P}{\beta_3\varsigma_{32}}\right)\left\{\frac{\sqrt{[a^2-l_1^2(a)][\rho^2-l_1^2(a)]}}{6l_1(a)}(2z_k^2+6a^2-3\rho^2)\arcsin\left[\frac{l_1(a)}{\rho}\right]\right.$$
$$\left. -\frac{2a^3}{3}\ln\left[\frac{l_1(a)}{a\left(a+\sqrt{a^2-l_1^2(a)}\right)}\right] - \frac{\sqrt{a^2-l_1^2(a)}}{18}[5l_1^2(a)-9\rho^2+16a^2+6z_k^2]\right\}. \tag{B.5}$$

Besides, the incremental indentation force is expressed as

$$\mathcal{F}(a) = \left(\frac{\sum_{k=1}^3 \alpha_k\varsigma_{k2}}{\sum_{k=1}^3 \alpha_k\varsigma_{k1}}\frac{P}{\beta_3\varsigma_{32}} - \frac{1}{\sum_{k=1}^3 \alpha_k\varsigma_{k1}}\frac{2}{R}\right)\frac{2a^3}{3\pi}. \tag{B.6}$$

The analytical solutions are verified by FE simulations, as presented in Fig. B.11. It should be noted that in panel (a), the conical indenter tends to penetrate the material near its sharp tip during finite element simulation, thus introducing computational errors.

For an indenter with a general profile described by $f(\rho,\phi) = \sum_{n=0}^{+\infty}\mho_n\rho^n$, where $\mho_n$ are the shape parameters, the corresponding densities are given by

$$\omega_1 = \frac{1}{\pi^2}\left[\frac{d}{\sum_{k=1}^3 \alpha_k\varsigma_{k1}}\frac{1}{\sqrt{a^2-\rho^2}} - \frac{\sum_{k=1}^3 \alpha_k\varsigma_{k2}}{\sum_{k=1}^3 \alpha_k\varsigma_{k1}}\frac{P}{\beta_3\varsigma_{32}}\sqrt{a^2-\rho^2}\right]$$
$$-\frac{1}{\sum_{k=1}^3 \alpha_k\varsigma_{k1}}\sum_{n=0}^{+\infty}\mho_n\frac{n(n+1)\rho^{n+1}\Gamma\left(\frac{1-n}{2}\right)\Gamma\left(\frac{n}{2}\right) - 2\sqrt{\pi}(n+1)\csc\left(\frac{n\pi}{2}\right)a^{n+1}\left[\frac{a}{\sqrt{a^2-\rho^2}} - {}_2\widehat{F}_1\left(\frac{1}{2},-\frac{n+1}{2};\frac{1-n}{2};\frac{\rho^2}{a^2}\right)\right]}{4\pi\rho^2\Gamma\left(-\frac{n}{2}\right)\Gamma\left(\frac{n+3}{2}\right)}, \tag{B.7}$$

where $d = -\sum_{n=0}^{+\infty}\mho_n\frac{\pi\sqrt{\pi}}{2}\frac{(n+1)\csc(n\pi/2)}{\Gamma(-n/2)\Gamma[(n+3)/2]}a^n$, $\Gamma(\#)$ is the gamma function, and ${}_2\widehat{F}_1(\#,\#;\#;\#)$ is the Gauss hypergeometric function. It is worth noting that, when determining the explicit form of each term for $n \in \mathbb{N}^+$, the limit with respect to n should be taken instead of directly substituting the positive integer value. The incremental indentation force is derived as

$$\mathcal{F}(a) = \frac{\sum_{k=1}^3 \alpha_k\varsigma_{k2}}{\sum_{k=1}^3 \alpha_k\varsigma_{k1}}\frac{2Pa^3}{3\pi\beta_3\varsigma_{32}} - \frac{1}{\sum_{k=1}^3 \alpha_k\varsigma_{k1}}\sum_{n=0}^{+\infty}\mho_n\frac{n\Gamma(1+n/2)}{\sqrt{\pi}\Gamma[(n+3)/2]}a^{n+1}. \tag{B.8}$$

Here, $-\pi\csc(n\pi/2)/\Gamma(-n/2) = \Gamma(1+n/2)$ and $\int {}_2\widehat{F}_1\left(\frac{1}{2},-\frac{n+1}{2};\frac{1-n}{2};\frac{\rho^2}{a^2}\right)\frac{1}{\rho}\mathrm{d}\rho = \frac{n+1}{4\sqrt{\pi}}\hat{G}^{2,2}_{3,3}\left(-\frac{\rho^2}{a^2}\middle|\begin{matrix}\frac{1}{2},\frac{n+3}{2},1\\0,0,\frac{n+1}{2}\end{matrix}\right)$ are adopted, where $\hat{G}^{m,n}_{p,q}(z|^{a_1,\ldots,a_p}_{b_1,\ldots,b_q}) := \frac{1}{2\pi i}\int_L \frac{\prod_{j=1}^m\Gamma(b_j+s)\prod_{j=1}^n\Gamma(1-a_j-s)}{\prod_{j=n+1}^p\Gamma(a_j+s)\prod_{j=m+1}^q\Gamma(1-b_j-s)}z^{-s}\mathrm{d}s$ is the Meijer G-function. For the special case $\mho_1 = \cot\vartheta$ and $\mho_2 = 1/(2R)$, Eq. (B.8) is consistent with Eqs. (B.3) and (B.6), respectively. Besides, the modified JKR solutions for indentation depth and

incremental indentation force are expressed as

$$d(a)=\sum_{n=0}^{+\infty}\mathfrak{V}_n\frac{\sqrt{\pi}(n+1)\Gamma(1+n/2)}{2\Gamma[(n+3)/2]}a^n+\sum_{k=1}^{3}\alpha_k\varsigma_{k1}\sqrt{-\frac{2\eta\pi^2 a\sqrt{1+\left[\sum_{n=1}^{+\infty}n\mathfrak{V}_n a^{n-1}\right]^2}}{\sum_{k=1}^{3}\alpha_k\varsigma_{k1}}},$$
$$\mathcal{F}(a)=\frac{\sum_{k=1}^{3}\alpha_k\varsigma_{k2}}{\sum_{k=1}^{3}\alpha_k\varsigma_{k1}}\frac{2Pa^3}{3\pi\beta_3\varsigma_{32}}-\frac{1}{\sum_{k=1}^{3}\alpha_k\varsigma_{k1}}\sum_{n=0}^{+\infty}\mathfrak{V}_n\frac{n\Gamma(1+n/2)}{\sqrt{\pi}\Gamma[(n+3)/2]}a^{n+1}-\frac{2}{\pi}\sqrt{-\frac{2\eta\pi^2a^3\sqrt{1+\left[\sum_{n=1}^{+\infty}n\mathfrak{V}_n a^{n-1}\right]^2}}{\sum_{k=1}^{3}\alpha_k\varsigma_{k1}}}. \tag{B.9}$$

If the boundary conditions at $z=0$ are altered to

$$\begin{aligned}&w_1=W(\rho,\phi),\quad &&\sigma_{z2}=Q(\rho,\phi),\quad &&(\rho,\phi)\in S\\&\sigma_{z1}=0,\quad &&\frac{\partial\sigma_{z2}}{\partial z}=0,\quad &&(\rho,\phi)\notin S\\&\sigma_{\rho1}=0,\quad &&\sigma_{\phi1}=0,\quad &&(\rho,\phi)\in[0,+\infty)\times[0,2\pi]\end{aligned} \tag{B.10}$$

we still adopt $\Psi_0=0$ and $\Psi_k=\sum_{i=1}^{2}\varsigma_{ki}\hat{H}_i(\rho,\phi,z_k)(k=1,2,3)$, but $\hat{H}_i(i=1,2)$ should now be constructed as

$$\begin{aligned}\hat{H}_1(\rho,\phi,z_k)&=\iint_S\ln\left[\sqrt{\rho^2+\rho_0^2-2\rho\rho_0\cos(\phi-\phi_0)+z_k^2}+z_k\right]\omega_1(\rho_0,\phi_0)\rho_0\mathrm{d}\rho_0\mathrm{d}\phi_0,\\\hat{H}_2(\rho,\phi,z_k)&=\iint_S\left\{z_k\ln\left[\sqrt{\rho^2+\rho_0^2-2\rho\rho_0\cos(\phi-\phi_0)+z_k^2}+z_k\right]\right.\\&\quad\left.-\sqrt{\rho^2+\rho_0^2-2\rho\rho_0\cos(\phi-\phi_0)+z_k^2}\right\}\omega_2(\rho_0,\phi_0)\rho_0\mathrm{d}\rho_0\mathrm{d}\phi_0,\end{aligned} \tag{B.11}$$

rather than in the form given in Eq. (17). Following the procedure similar to that described above, it can be shown that $\varsigma_{ki}(k=1,2,3;i=1,2)$ still satisfies Eq. (21). However, the densities are now governed by

$$\begin{aligned}&\iint_S\frac{\omega_1(\rho_0,\phi_0)\rho_0\mathrm{d}\rho_0\mathrm{d}\phi_0}{\sqrt{\rho^2+\rho_0^2-2\rho\rho_0\cos(\phi-\phi_0)}}=\frac{1}{\sum_{k=1}^{3}\alpha_k\varsigma_{k1}}\left\{W(\rho,\phi)-\sum_{k=1}^{3}\alpha_k\varsigma_{k2}\times\right.\\&\qquad\left.\iint_S\ln\left[\sqrt{\rho^2+\rho_0^2-2\rho\rho_0\cos(\phi-\phi_0)}\right]\omega_2(\rho_0,\phi_0)\rho_0\mathrm{d}\rho_0\mathrm{d}\phi_0\right\},\\&\iint_S\frac{\omega_2(\rho_0,\phi_0)\rho_0\mathrm{d}\rho_0\mathrm{d}\phi_0}{\sqrt{\rho^2+\rho_0^2-2\rho\rho_0\cos(\phi-\phi_0)}}=\frac{Q(\rho,\phi)}{\beta_3\varsigma_{32}},\end{aligned} \tag{B.12}$$

resulting in

$$\begin{aligned}\omega_2(\rho,\phi)&=-\frac{1}{\pi^2\rho}\mathcal{L}(\rho)\frac{\mathrm{d}}{\mathrm{d}\rho}\int_\rho^a\frac{t\mathrm{d}t}{\sqrt{t^2-\rho^2}}\mathcal{L}\left(\frac{1}{t^2}\right)\frac{\mathrm{d}}{\mathrm{d}t}\int_0^t\frac{\rho_0\mathrm{d}\rho_0}{\sqrt{t^2-\rho_0^2}}\mathcal{L}(\rho_0)\frac{Q(\rho_0,\phi)}{\beta_3\varsigma_{32}},\\\omega_1(\rho,\phi)&=-\frac{1}{\pi^2\rho}\mathcal{L}(\rho)\frac{\mathrm{d}}{\mathrm{d}\rho}\int_\rho^a\frac{t\mathrm{d}t}{\sqrt{t^2-\rho^2}}\mathcal{L}\left(\frac{1}{t^2}\right)\frac{\mathrm{d}}{\mathrm{d}t}\int_0^t\frac{\rho_0\mathrm{d}\rho_0}{\sqrt{t^2-\rho_0^2}}\mathcal{L}(\rho_0)\times\\&\quad\frac{1}{\sum_{k=1}^{3}\alpha_k\varsigma_{k1}}\left[W(\rho_0,\phi)-\sum_{k=1}^{3}\alpha_k\varsigma_{k2}\iint_S\ln\left[\sqrt{\rho_0^2+y^2-2\rho_0y\cos(\phi-\psi_0)}\right]\omega_2(y,\psi_0)y\mathrm{d}y\mathrm{d}\psi_0\right],\end{aligned} \tag{B.13}$$

when the torsionless axisymmetric problem is considered. Under the boundary conditions specified in Eq. (B.10), the densities are obtained as

$$\omega_2=\frac{Q}{4\beta_3\varsigma_{32}},\omega_1=\frac{1}{\pi^2}\left\{\frac{d}{\sum_{k=1}^{3}\alpha_k\varsigma_{k1}}\frac{1}{\sqrt{a^2-\rho^2}}+\frac{Q\pi}{2\beta_3\varsigma_{32}}\frac{\sum_{k=1}^{3}\alpha_k\varsigma_{k2}}{\sum_{k=1}^{3}\alpha_k\varsigma_{k1}}\left[\sqrt{a^2-\rho^2}-\frac{a^2(2\ln a+1)}{4}\frac{1}{\sqrt{a^2-\rho^2}}\right]\right\} \tag{B.14}$$

when we set $Q(\rho,\phi)=a\widehat{E}\left(\frac{\rho^2}{a^2}\right)Q=\int_0^\rho\frac{\mathrm{d}x}{\sqrt{\rho^2-x^2}}\int_x^a\frac{\rho_0\mathrm{d}\rho_0}{\sqrt{\rho_0^2-x^2}}\mathcal{L}\left(\frac{x^2}{\rho\rho_0}\right)Q$ and $W(\rho,\phi)=d$, where $\widehat{E}(\#)$ is the complete elliptic integrals of the second kind and Q is a constant. Here, the logarithmic function whose argument has also been non-dimensionalized through division by a unit length. Of note, the integral

$$\iint_S\ln\left[\sqrt{\rho^2+y^2-2\rho y\cos(\phi-\psi_0)}\right]\frac{Q}{4\beta_3\varsigma_{32}}y\mathrm{d}y\mathrm{d}\psi_0=\frac{Q\pi}{8\beta_3\varsigma_{32}}[a^2(2\ln a-1)+\rho^2] \tag{B.15}$$

is employed in solving for the density ω_1. Then, the corresponding incremental indentation force is obtained by

$$\mathcal{F}(d)=\frac{2}{\pi}\left\{\frac{\sum_{k=1}^{3}\alpha_k\varsigma_{k2}}{\sum_{k=1}^{3}\alpha_k\varsigma_{k1}}\frac{Q\pi a^3(6\ln a-1)}{24\beta_3\varsigma_{32}}-\frac{da}{\sum_{k=1}^{3}\alpha_k\varsigma_{k1}}\right\}. \tag{B.16}$$

Appendix C. A hyperelastic film on a smooth substrate

In nanoimprint lithography, modeling contact between the indenter and a film-substrate system provides a more physically accurate representation of experimental conditions than does a half-space approximation. A film-substrate system consists of distinct layers with differing mechanical properties, and the film-substrate interface critically influences the mechanical response during indentation. Thus, adopting a contact model that explicitly accounts for the layered configuration is essential to accurately capture local deformation mechanism and stress distribution, thereby enabling a more physically realistic description of the indentation process. Here, we examine the contact behaviors of a hyperelastic film on a smooth substrate according to the generalized image method. Contraction mappings are formulated, and the densities are subsequently approximated through iteration.

To extend the model established in Section 3, we examine the frictionless and non-adhesive thermoelastic contact between a rigid indenter and a hyperelastic film of thickness c bonded to a rigid smooth substrate. The boundary conditions at $z=0$ take the same form as in Eq. (16), while at $z=c$,

$$w_1=0,\quad \sigma_{\rho 1}=0,\quad \sigma_{\phi 1}=0,\quad \sigma_{z2}=0.\quad (\rho,\phi)\in[0,+\infty)\times[0,2\pi] \tag{C.1}$$

Based on the generalized image method (Fabrikant, 2004), we shift the potential functions and set

$$\begin{aligned}&\Psi_0=0,\\ &\Psi_k=\sum_{i=1}^{2}\left\{\hat{H}_i(\rho,\phi,z_k)+\sum_{m=0}^{+\infty}\sum_{n=0}^{+\infty}\sum_{q=0}^{+\infty}[\varsigma_{ki(+)}^{\{mnq\}}\hat{H}_i(\rho,\phi,z_k+c_{mnq})+\varsigma_{ki(-)}^{\{mnq\}}\hat{H}_i(\rho,\phi,z_k-c_{mnq})]\right\},\end{aligned} \tag{C.2}$$

where $c_{mnq}:=mc_1+nc_2+qc_3$, with $c_k=s_kc(k=1,2,3)$. Here, $\varsigma_{ki(+)}^{\{mnq\}}$ and $\varsigma_{ki(-)}^{\{mnq\}}$ denote the combination coefficients for the potential functions. The functions $\hat{H}_i$ are taken to have the same form as those in Eq. (17) and are required to satisfy Eq. (18). Substituting Eq. (C.2) into Eqs. $(16)_{3\text{-}6}$ and (C.1) yields the recurrence relations between the combination coefficients, as presented in Appendix A. With these coefficients determined, Eqs. $(16)_{1\text{-}2}$ lead to the integral equations containing the unknown densities as

$$\begin{aligned}P(\rho,\phi)=\gamma_{23}\Bigg\{&[1+\varsigma_{32(+)}^{\{000\}}+\varsigma_{32(-)}^{\{000\}}]\lim_{z_3\to0^+}\frac{\partial^2}{\partial z_3^2}\iint_S\frac{\omega_2(\rho_0,\phi_0)\rho_0\mathrm{d}\rho_0\mathrm{d}\phi_0}{\sqrt{\rho^2+\rho_0^2-2\rho\rho_0\cos(\phi-\phi_0)+z_3^2}}\\&+\sum_{\substack{m=0\\(m,n,q)\neq(0,0,0)}}^{+\infty}\sum_{n=0}^{+\infty}\sum_{q=0}^{+\infty}[\varsigma_{32(+)}^{\{mnq\}}+\varsigma_{32(-)}^{\{mnq\}}]\lim_{z_3\to0^+}\frac{\partial^2}{\partial z_3^2}\iint_S\frac{\omega_2(\rho_0,\phi_0)\rho_0\mathrm{d}\rho_0\mathrm{d}\phi_0}{\sqrt{\rho^2+\rho_0^2-2\rho\rho_0\cos(\phi-\phi_0)+(z_3+c_{mnq})^2}}\Bigg\},\end{aligned} \tag{C.3}$$

$$\begin{aligned}W(\rho,\phi)-\sum_{k=1}^{3}\alpha_k\Bigg\{&[1+\varsigma_{k2(+)}^{\{000\}}+\varsigma_{k2(-)}^{\{000\}}]\iint_S\frac{\omega_2(\rho_0,\phi_0)\rho_0\mathrm{d}\rho_0\mathrm{d}\phi_0}{\sqrt{\rho^2+\rho_0^2-2\rho\rho_0\cos(\phi-\phi_0)}}\\&+\sum_{\substack{m=0\\(m,n,q)\neq(0,0,0)}}^{+\infty}\sum_{n=0}^{+\infty}\sum_{q=0}^{+\infty}[\varsigma_{k2(+)}^{\{mnq\}}+\varsigma_{k2(-)}^{\{mnq\}}]\iint_S\frac{\omega_2(\rho_0,\phi_0)\rho_0\mathrm{d}\rho_0\mathrm{d}\phi_0}{\sqrt{\rho^2+\rho_0^2-2\rho\rho_0\cos(\phi-\phi_0)+c_{mnq}^2}}\Bigg\}\\=\sum_{k=1}^{3}\alpha_k\Bigg\{&[1+\varsigma_{k1(+)}^{\{000\}}+\varsigma_{k1(-)}^{\{000\}}]\iint_S\frac{\omega_1(\rho_0,\phi_0)\rho_0\mathrm{d}\rho_0\mathrm{d}\phi_0}{\sqrt{\rho^2+\rho_0^2-2\rho\rho_0\cos(\phi-\phi_0)}}\\&+\sum_{\substack{m=0\\(m,n,q)\neq(0,0,0)}}^{+\infty}\sum_{n=0}^{+\infty}\sum_{q=0}^{+\infty}[\varsigma_{k1(+)}^{\{mnq\}}+\varsigma_{k1(-)}^{\{mnq\}}]\iint_S\frac{\omega_1(\rho_0,\phi_0)\rho_0\mathrm{d}\rho_0\mathrm{d}\phi_0}{\sqrt{\rho^2+\rho_0^2-2\rho\rho_0\cos(\phi-\phi_0)+c_{mnq}^2}}\Bigg\}.\end{aligned} \tag{C.4}$$

ω_2 is solved from Eq. (C.3) first, and then substituted into Eq. (C.4) to obtain ω_1.

If we denote $[\varsigma_{32(+)}^{\{mnq\}}+\varsigma_{32(-)}^{\{mnq\}}]/[1+\varsigma_{32(+)}^{\{000\}}+\varsigma_{32(-)}^{\{000\}}]$ and $\gamma_{23}[1+\varsigma_{32(+)}^{\{000\}}+\varsigma_{32(-)}^{\{000\}}]$ as $\mathcal{R}_{mnq}$ and $\mathcal{R}_0$, respectively, Eq. (C.3) can be rewritten as

$$\begin{aligned}&\lim_{z_3\to0^+}\frac{\partial^2}{\partial z_3^2}\iint_S\frac{\omega_2(\rho_0,\phi_0)\rho_0\mathrm{d}\rho_0\mathrm{d}\phi_0}{\sqrt{\rho^2+\rho_0^2-2\rho\rho_0\cos(\phi-\phi_0)+z_3^2}}=\frac{P(\rho,\phi)}{\mathcal{R}_0}\\&-\sum_{\substack{m=0\\(m,n,q)\neq(0,0,0)}}^{+\infty}\sum_{n=0}^{+\infty}\sum_{q=0}^{+\infty}\mathcal{R}_{mnq}\lim_{z_3\to0^+}\frac{\partial^2}{\partial z_3^2}\iint_S\frac{\omega_2(\rho_0,\phi_0)\rho_0\mathrm{d}\rho_0\mathrm{d}\phi_0}{\sqrt{\rho^2+\rho_0^2-2\rho\rho_0\cos(\phi-\phi_0)+(z_3+c_{mnq})^2}}:=-2\pi\mathcal{P}(\rho,\phi),\end{aligned} \tag{C.5}$$

Consequently, a potential function can be constructed such that

$$\begin{aligned}&\lim_{z_3\to 0^+}\frac{\partial H(\rho,\phi,z_3)}{\partial z_3}=-2\pi\mathcal{P}(\rho,\phi),\quad &(\rho,\phi)\in[0,a)\times[0,2\pi]\\&H(\rho,\phi,0)=0,\quad &(\rho,\phi)\in[a,+\infty)\times[0,2\pi]\end{aligned}\tag{C.6}$$

where $H(\rho,\phi,z_3):=\frac{\partial}{\partial z_3}\iint_S\frac{\omega_2(\rho_0,\phi_0)\rho_0\mathrm{d}\rho_0\mathrm{d}\phi_0}{\sqrt{\rho^2+\rho_0^2-2\rho\rho_0\cos(\phi-\phi_0)+z_3^2}}$ can be established as

$$\begin{aligned}H(\rho,\phi,0)&=4\int_\rho^a\frac{\mathrm{d}x}{\sqrt{x^2-\rho^2}}\int_0^x\frac{\rho_0\mathrm{d}\rho_0}{\sqrt{x^2-\rho_0^2}}\mathcal{L}\left(\frac{\rho\rho_0}{x^2}\right)\mathcal{P}(\rho_0,\phi)\\&=\lim_{z_3\to 0^+}\frac{\partial}{\partial z_3}\iint_S\frac{\omega_2(\rho_0,\phi_0)\rho_0\mathrm{d}\rho_0\mathrm{d}\phi_0}{\sqrt{\rho^2+\rho_0^2-2\rho\rho_0\cos(\phi-\phi_0)+z_3^2}}=-2\pi\omega_2(\rho,\phi)\end{aligned}\tag{C.7}$$

at $z_3=0$. The expression above yields a Fredholm integral equation of the second kind, given by

$$\begin{aligned}&\omega_2(\rho,\phi)+\frac{1}{\pi^2}\sum_{\substack{m=0\\(m,n,q)\neq(0,0,0)}}^{+\infty}\sum_{n=0}^{+\infty}\sum_{q=0}^{+\infty}\mathcal{R}_{mnq}\lim_{z_*\to c_{mnq}}\frac{\partial^2}{\partial z^2}\int_\rho^a\frac{\mathrm{d}x}{\sqrt{x^2-\rho^2}}\int_0^x\frac{\rho_0\mathrm{d}\rho_0}{\sqrt{x^2-\rho_0^2}}\mathcal{L}\left(\frac{\rho\rho_0}{x^2}\right)\\&\times\int_0^{2\pi}\int_0^a\frac{\omega_2(s,\phi_0)s\mathrm{d}s\mathrm{d}\phi_0}{\sqrt{s^2+\rho_0^2-2\,s\rho_0\cos(\phi-\phi_0)+z_*^2}}=\frac{1}{\pi^2\mathcal{R}_0}\int_\rho^a\frac{\mathrm{d}x}{\sqrt{x^2-\rho^2}}\int_0^x\frac{\rho_0\mathrm{d}\rho_0}{\sqrt{x^2-\rho_0^2}}\mathcal{L}\left(\frac{\rho\rho_0}{x^2}\right)P(\rho_0,\phi),\end{aligned}\tag{C.8}$$

with z_* taken as (z_3+c_{mnq}), from which we have

$$\begin{aligned}\omega_2(\rho,\phi)=&\frac{1}{\pi^2\mathcal{R}_0}\int_\rho^a\frac{\mathrm{d}x}{\sqrt{x^2-\rho^2}}\int_0^x\frac{\rho_0\mathrm{d}\rho_0}{\sqrt{x^2-\rho_0^2}}\mathcal{L}\left(\frac{\rho\rho_0}{x^2}\right)P(\rho_0,\phi)\\&-\frac{1}{\pi^2}\sum_{\substack{m=0\\(m,n,q)\neq(0,0,0)}}^{+\infty}\sum_{n=0}^{+\infty}\sum_{q=0}^{+\infty}\mathcal{R}_{mnq}\int_0^{2\pi}\int_0^a\mathcal{K}_2(\rho,s,\phi,\phi_0;c_{mnq})\omega_2(s,\phi_0)s\mathrm{d}s\mathrm{d}\phi_0.\end{aligned}\tag{C.9}$$

Here, $\mathcal{K}_2(\rho,s,\phi,\phi_0;c_{mnq})$ is the integral kernel defined in Appendix D. According to the Banach-Caccioppoli theorem (Jachymski et al., 2024), it is further demonstrated in Appendix E that the operator

$$\begin{aligned}\mathcal{N}_2[\omega_2]:=&\frac{1}{\pi^2\mathcal{R}_0}\int_\rho^a\frac{\mathrm{d}x}{\sqrt{x^2-\rho^2}}\int_0^x\frac{\rho_0\mathrm{d}\rho_0}{\sqrt{x^2-\rho_0^2}}\mathcal{L}\left(\frac{\rho\rho_0}{x^2}\right)P(\rho_0,\phi)\\&-\frac{1}{\pi^2}\sum_{\substack{m=0\\(m,n,q)\neq(0,0,0)}}^{+\infty}\sum_{n=0}^{+\infty}\sum_{q=0}^{+\infty}\mathcal{R}_{mnq}\int_0^{2\pi}\int_0^a\mathcal{K}_2(\rho,s,\phi,\phi_0;c_{mnq})\omega_2(s,\phi_0)s\mathrm{d}s\mathrm{d}\phi_0\end{aligned}\tag{C.10}$$

is a contraction operator. Consequently, we can prescribe an initial density $\omega_2^{[0]}$ and then iteratively apply $\omega_2^{[k+1]}=\mathcal{N}_2[\omega_2^{[k]}](k\geqslant 0)$ to obtain the final solution ω_2, where $\lim_{k\to+\infty}\|\omega_2^{[k]}-\omega_2\|_\infty=0$, and $\|\#\|_\infty$ denotes the supremum norm, as defined in Appendix E.

Similarly, in terms of the coefficients $\mathcal{D}_{mnq}=\left(\sum_{k=1}^3\alpha_k[\varsigma_{k1(+)}^{\{mnq\}}+\varsigma_{k1(-)}^{\{mnq\}}]\right)/\left(\sum_{k=1}^3\alpha_k[1+\varsigma_{k1(+)}^{\{000\}}+\varsigma_{k1(-)}^{\{000\}}]\right)$ and $\mathcal{D}_0=\left(\sum_{k=1}^3\alpha_k[1+\varsigma_{k1(+)}^{\{000\}}+\varsigma_{k1(-)}^{\{000\}}]\right)$, Eq. (C.4) can be expressed as

$$\iint_S\frac{\omega_1(\rho_0,\phi_0)\rho_0\mathrm{d}\rho_0\mathrm{d}\phi_0}{\sqrt{\rho^2+\rho_0^2-2\rho\rho_0\cos(\phi-\phi_0)}}+\sum_{\substack{m=0\\(m,n,q)\neq(0,0,0)}}^{+\infty}\sum_{n=0}^{+\infty}\sum_{q=0}^{+\infty}\mathcal{D}_{mnq}\iint_S\frac{\omega_1(\rho_0,\phi_0)\rho_0\mathrm{d}\rho_0\mathrm{d}\phi_0}{\sqrt{\rho^2+\rho_0^2-2\rho\rho_0\cos(\phi-\phi_0)+c_{mnq}^2}}=\frac{\mathcal{Q}(\rho,\phi)}{\mathcal{D}_0},\tag{C.11}$$

where

$$\begin{aligned}\mathcal{Q}(\rho,\phi):=W(\rho,\phi)-\sum_{k=1}^3\alpha_k\Bigg\{&[1+\varsigma_{k2(+)}^{\{000\}}+\varsigma_{k2(-)}^{\{000\}}]\iint_S\frac{\omega_2(\rho_0,\phi_0)\rho_0\mathrm{d}\rho_0\mathrm{d}\phi_0}{\sqrt{\rho^2+\rho_0^2-2\rho\rho_0\cos(\phi-\phi_0)}}\\&+\sum_{\substack{m=0\\(m,n,q)\neq(0,0,0)}}^{+\infty}\sum_{n=0}^{+\infty}\sum_{q=0}^{+\infty}[\varsigma_{k2(+)}^{\{mnq\}}+\varsigma_{k2(-)}^{\{mnq\}}]\iint_S\frac{\omega_2(\rho_0,\phi_0)\rho_0\mathrm{d}\rho_0\mathrm{d}\phi_0}{\sqrt{\rho^2+\rho_0^2-2\rho\rho_0\cos(\phi-\phi_0)+c_{mnq}^2}}\Bigg\}\end{aligned}\tag{C.12}$$

becomes a known function after substituting ω_2 derived from Eq. (C.9). Through Eq. (D.1), Eq. (C.11) takes the form

$$\begin{aligned}
&4\int_0^{\rho}\frac{\mathrm{d}x}{\sqrt{\rho^2-x^2}}\int_x^{a}\frac{\rho_0\mathrm{d}\rho_0}{\sqrt{\rho_0^2-x^2}}\mathcal{L}\left(\frac{x^2}{\rho\rho_0}\right)\omega_1(\rho_0,\phi)\\
&+4\sum_{\substack{m=0\\(m,n,q)\neq(0,0,0)}}^{+\infty}\sum_{n=0}^{+\infty}\sum_{q=0}^{+\infty}\mathcal{D}_{mnq}\int_0^{a}\int_0^{\rho}\frac{\mathrm{d}x}{\sqrt{\rho^2-x^2}}\frac{\frac{\partial l_1(x,\rho_0,c_{mnq})}{\partial x}}{\sqrt{\rho_0^2-l_1^2(x,\rho_0,c_{mnq})}}\mathcal{L}\left[\frac{l_1^2(x,\rho_0,c_{mnq})}{\rho\rho_0}\right]\omega_1(\rho_0,\phi)\rho_0\mathrm{d}\rho_0=\frac{\mathcal{Q}(\rho,\phi)}{\mathcal{D}_0},
\end{aligned}\tag{C.13}$$

which leads to another Fredholm integral equation of the second kind as

$$\begin{aligned}
\omega_1(\rho,\phi)=&-\frac{\mathcal{L}(\rho)}{\pi^2\mathcal{D}_0\rho}\frac{\mathrm{d}}{\mathrm{d}\rho}\int_{\rho}^{a}\frac{t\mathrm{d}t}{\sqrt{t^2-\rho^2}}\mathcal{L}\left(\frac{1}{t^2}\right)\frac{\mathrm{d}}{\mathrm{d}t}\int_0^{t}\frac{\mathcal{L}(\rho_0)\mathcal{Q}(\rho_0,\phi)\rho_0\mathrm{d}\rho_0}{\sqrt{t^2-\rho_0^2}}\\
&-\frac{1}{\pi^2}\sum_{\substack{m=0\\(m,n,q)\neq(0,0,0)}}^{+\infty}\sum_{n=0}^{+\infty}\sum_{q=0}^{+\infty}\mathcal{D}_{mnq}\int_0^{2\pi}\int_0^{a}\mathcal{K}_1(\rho,s,\phi,\phi_0;c_{mnq})\omega_1(s,\phi_0)s\mathrm{d}s\mathrm{d}\phi_0,
\end{aligned}\tag{C.14}$$

where $\mathcal{K}_1(\rho,\rho_0,\phi,\phi_0;c_{mnq})$ is defined in Appendix D. In the presence of a constant term in $\mathcal{Q}(\rho,\phi)$, the first term of Eq. (C.14) exhibits a $1/\sqrt{a^2-\rho^2}$ weak singularity. To eliminate this weak singularity, we multiply both sides by $\sqrt{a^2-\rho^2}$ and introduce the scaled quantity $\omega_1^*:=\sqrt{a^2-\rho^2}\omega_1$, allowing us to define the operator $\mathcal{N}_1$ as

$$\begin{aligned}
\mathcal{N}_1[\omega_1^*]:=&-\frac{\mathcal{L}(\rho)\sqrt{a^2-\rho^2}}{\pi^2\mathcal{D}_0\rho}\frac{\mathrm{d}}{\mathrm{d}\rho}\int_{\rho}^{a}\frac{t\mathrm{d}t}{\sqrt{t^2-\rho^2}}\mathcal{L}\left(\frac{1}{t^2}\right)\frac{\mathrm{d}}{\mathrm{d}t}\int_0^{t}\frac{\mathcal{L}(\rho_0)\mathcal{Q}(\rho_0,\phi)\rho_0\mathrm{d}\rho_0}{\sqrt{t^2-\rho_0^2}}\\
&-\frac{\sqrt{a^2-\rho^2}}{\pi^2}\sum_{\substack{m=0\\(m,n,q)\neq(0,0,0)}}^{+\infty}\sum_{n=0}^{+\infty}\sum_{q=0}^{+\infty}\mathcal{D}_{mnq}\int_0^{2\pi}\int_0^{a}\mathcal{K}_1(\rho,\rho_0,\phi,\phi_0;c_{mnq})\frac{\omega_1^*(\rho_0,\phi_0)}{\sqrt{a^2-\rho_0^2}}\rho_0\mathrm{d}\rho_0\mathrm{d}\phi_0,
\end{aligned}\tag{C.15}$$

Here, $\mathcal{N}_1[\omega_1^*]$ is also a contraction operator, as presented in Appendix E, which indicates that ω_1^* can be obtained via $\lim_{k\to+\infty}\|(\omega_1^*)^{[k]}-\omega_1^*\|_\infty=0$. For instance, if we assume that $P(\rho,\phi)=0$ and $W(\rho,\phi)$ is a constant value d, leading to $\omega_2=0$ in this case. Substituting these results into Eq. (C.14) and disregarding the terms with integral kernels, we are able to calculate the zeroth approximation of $\omega_1^{[0]}$ as $d/\left(\pi^2\mathcal{D}_0\sqrt{a^2-\rho^2}\right)$, which represents the solution for the problem of a flat punch acting upon a half-space. Then, substituting the solution back into Eq. (C.14) enables us to acquire the first approximation

$$\begin{aligned}
\omega_1^{[1]}=&\frac{d}{\pi^2\mathcal{D}_0}\left\{\frac{1}{\sqrt{a^2-\rho^2}}\left[1-\frac{2}{\pi}\sum_{\substack{m=0\\(m,n,q)\neq(0,0,0)}}^{+\infty}\sum_{n=0}^{+\infty}\sum_{q=0}^{+\infty}\mathcal{D}_{mnq}\arctan\left[\sqrt{\frac{l_1(a,a,c_{mnq})}{l_2(a,a,c_{mnq})}}\right]\right]\right.\\
&-\frac{1}{\pi}\sum_{\substack{m=0\\(m,n,q)\neq(0,0,0)}}^{+\infty}\sum_{n=0}^{+\infty}\sum_{q=0}^{+\infty}\mathcal{D}_{mnq}\left[\frac{\sqrt{l_2^2(\rho,a,c_{mnq})-a^2}}{l_2^2(\rho,a,c_{mnq})-l_1^2(\rho,a,c_{mnq})}\operatorname{arctanh}\left\{\frac{2l_1^2(\rho,a,c_{mnq})\sqrt{a^2-\rho^2}}{[\rho^2+l_1^2(\rho,a,c_{mnq})]\sqrt{a^2-l_1^2(\rho,a,c_{mnq})}}\right\}\right.\\
&\left.\left.+\frac{\sqrt{a^2-l_1^2(\rho,a,c_{mnq})}}{l_2^2(\rho,a,c_{mnq})-l_1^2(\rho,a,c_{mnq})}\arctan\left\{\frac{2l_2^2(\rho,a,c_{mnq})\sqrt{a^2-\rho^2}}{[\rho^2+l_2^2(\rho,a,c_{mnq})]\sqrt{l_2^2(\rho,a,c_{mnq})-a^2}}\right\}\right]\right\}.
\end{aligned}\tag{C.16}$$

The analysis is then extended beyond the rigid substrate scenario considered in Appendix C to the case of a hyperelastic film of thickness c bonded to an elastic substrate and subjected to frictionless, non-adhesive thermoelastic contact with a rigid indenter. The corresponding boundary and interface conditions are expressed as

$$\begin{aligned}
&w_1^{\langle1\rangle}=W(\rho,\phi),\quad \frac{\partial\sigma_{z2}^{\langle1\rangle}}{\partial z}=P(\rho,\phi),\quad (\rho,\phi)\in S\\
&\sigma_{z1}^{\langle1\rangle}=0,\qquad \sigma_{z2}^{\langle1\rangle}=0,\qquad (\rho,\phi)\notin S\qquad\qquad \text{when } z=0\\
&\sigma_{\rho1}^{\langle1\rangle}=0,\qquad \sigma_{\phi1}^{\langle1\rangle}=0,\qquad (\rho,\phi)\in[0,+\infty)\times[0,2\pi]
\end{aligned}\tag{C.17}$$

and

$$\begin{aligned}
&w_1^{\langle1\rangle}=w_2^{\langle2\rangle},\quad \sigma_{z1}^{\langle1\rangle}=\sigma_{z1}^{\langle2\rangle},\quad \sigma_{\rho1}^{\langle1\rangle}=\sigma_{\rho1}^{\langle2\rangle}=0,\quad (\rho,\phi)\in[0,+\infty)\times[0,2\pi]\quad \text{when } z=c\\
&\sigma_{z2}^{\langle1\rangle}=\sigma_{z2}^{\langle2\rangle},\quad \frac{\partial\sigma_{z2}^{\langle1\rangle}}{\partial z}=\frac{\partial\sigma_{z2}^{\langle2\rangle}}{\partial z},\quad \sigma_{\phi1}^{\langle1\rangle}=\sigma_{\phi1}^{\langle2\rangle}=0,\quad (\rho,\phi)\in[0,+\infty)\times[0,2\pi]\quad \text{when } z=c
\end{aligned}\tag{C.18}$$

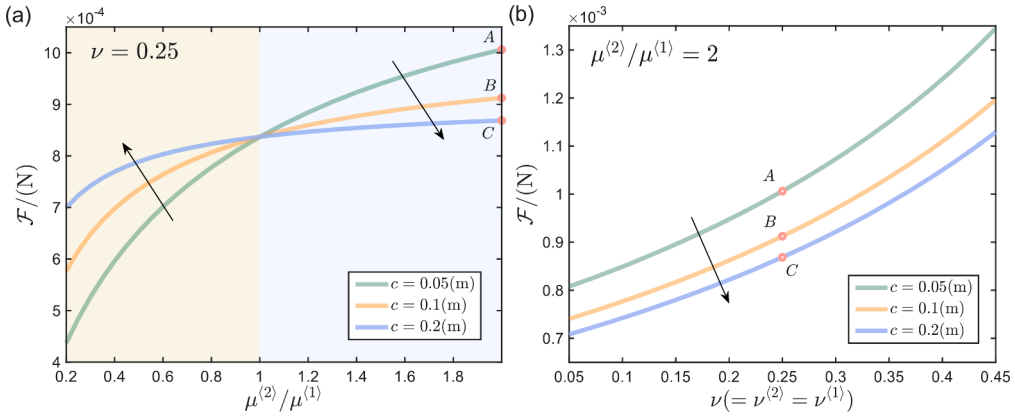


Fig. C.12. Effects of layer thickness and material parameters on the indentation response. (a) shows the influence of the shear modulus ratio on the incremental indentation force for different layer thicknesses. Yellow shading denotes a substrate that is softer compared to the film, whereas the blue shading denotes the opposite case. (b) shows the influence of Poisson's ratio on the incremental indentation force for different layer thicknesses. Points A, B, and C in (a) are matched with their counterparts in (b).

where the superscript $\langle\#\rangle$ distinguishes between the film ($j = 1$) and substrate ($j = 2$). In the film and substrate, we may take

$$\begin{aligned}
&\Psi_0^{\langle 1\rangle} = 0,\\
&\Psi_k^{\langle 1\rangle} = \sum_{i=1}^{2}\left\{\hat{H}_i(\rho,\phi,z_k^{\langle 1\rangle}) + \sum_{m=0}^{+\infty}\sum_{n=0}^{+\infty}\sum_{q=0}^{+\infty}[\varsigma_{ki\langle +\rangle\langle 1\rangle}^{\{mnq\}}\hat{H}_i(\rho,\phi,c_{mnq}^{\langle 1\rangle}+z_k^{\langle 1\rangle}) + \varsigma_{ki\langle -\rangle\langle 1\rangle}^{\{mnq\}}\hat{H}_i(\rho,\phi,c_{mnq}^{\langle 1\rangle}-z_k^{\langle 1\rangle})]\right\},
\end{aligned} \tag{C.19}$$

for $k = 1, 2, 3$, and

$$\begin{aligned}
&\Psi_0^{\langle 2\rangle} = 0,\\
&\Psi_k^{\langle 2\rangle} = \sum_{i=1}^{2}\sum_{m=0}^{+\infty}\sum_{n=0}^{+\infty}\sum_{q=0}^{+\infty}[\varsigma_{ki\langle 2\rangle}^{\{mnq\}}\hat{H}_i(\rho,\phi,z_k^{\langle 2\rangle}-c_k^{\langle 2\rangle}+c_{mnq}^{\langle 1\rangle})],
\end{aligned} \tag{C.20}$$

respectively, where $z_k^{\langle j\rangle} = s_k^{\langle j\rangle}z$, $c_k^{\langle j\rangle} = s_k^{\langle j\rangle}c$, and $c_{mnq}^{\langle j\rangle} = mc_1{}^{\langle j\rangle} + nc_2{}^{\langle j\rangle} + qc_3{}^{\langle j\rangle}$; $\varsigma_{ki\langle j\rangle}^{\{mnq\}}$ and $\varsigma_{ki\langle j\rangle}^{\{mnq\}}$ are coefficients in the film ($j = 1$) and the substrate ($j = 2$) for combination of potential functions, respectively; $\hat{H}_i$ have the same form as in Eq. (17). The remaining procedure of the derivation follows that presented above and is omitted here for brevity. It is found that a decrease in layer thickness amplifies the impact of substrate properties on the indentation behavior of the film. In an elastic substrate, for instance, the indentation response is sensitive to the substrate to film shear modulus ratio and Poisson's ratio as the layer thickness varies. Nevertheless, the layer thickness has a minor influence on the rate of change of the incremental indentation force, as illustrated in Fig. C.12. In panel (a), condition $\mu^{\langle 2\rangle}/\mu^{\langle 1\rangle} \to +\infty$ corresponds to the limiting case of a rigid substrate solution, whereas condition $\mu^{\langle 2\rangle}/\mu^{\langle 1\rangle} \to 1$ corresponds to the half-space solution.

Appendix D. Essential integrals

The interchangeability of s and ρ_0 allows us to express

$$\frac{1}{\sqrt{s^2+\rho_0^2-2\,s\rho_0\cos(\phi-\phi_0)+z^2}} = \frac{2}{\pi}\int_0^{\rho_0}\frac{\mathcal{G}\left[\frac{l_1^2(y,s,z)}{\rho_0 s},\phi-\phi_0\right]}{\sqrt{s^2-l_1^2(y,s,z)}\sqrt{\rho_0^2-y^2}}\frac{\partial l_1(y,s,z)}{\partial y}\mathrm{d}y, \tag{D.1}$$

from which we have

$$\begin{aligned}
&\int_\rho^a\frac{\mathrm{d}x}{\sqrt{x^2-\rho^2}}\int_0^x\frac{\rho_0\mathrm{d}\rho_0}{\sqrt{x^2-\rho_0^2}}\mathcal{L}\left(\frac{\rho\rho_0}{x^2}\right)\int_0^{2\pi}\int_0^a\frac{\omega_2(s,\phi_0)s\mathrm{d}s\mathrm{d}\phi_0}{\sqrt{s^2+\rho_0^2-2\,s\rho_0\cos(\phi-\phi_0)+z^2}}\\
&=\int_0^{2\pi}\int_0^a\int_\rho^a\frac{\mathrm{d}x}{\sqrt{x^2-\rho^2}}\int_{y=0}^{y=x}\frac{\mathcal{G}\left[\frac{l_1^2(y,s,z)\rho}{sx^2},\phi-\phi_0\right]\mathrm{d}l_1(y,s,z)}{\sqrt{s^2-l_1^2(y,s,z)}}\omega_2(s,\phi_0)s\mathrm{d}s\mathrm{d}\phi_0.
\end{aligned} \tag{D.2}$$

In view of the integral satisfying

$$\int_{y=0}^{y=x} \frac{\mathcal{G}\left[\frac{l_1^2(y,s,z)\rho}{sx^2}, \phi-\phi_0\right] \mathrm{d}l_1(y,s,z)}{\sqrt{s^2-l_1^2(y,s,z)}} = \left\{ -\arctan\left[\frac{l_1(x,s,z)}{\sqrt{s^2-l_1^2(x,s,z)}}\right] + 2\Re\left[\operatorname{arctanh}\left(\frac{l_1(x,s,z)\sqrt{s\rho \mathrm{e}^{-\mathrm{i}(\phi-\phi_0)}-x^2}}{x\sqrt{s^2-l_1^2(x,s,z)}}\right)\frac{x}{\sqrt{s\rho \mathrm{e}^{-\mathrm{i}(\phi-\phi_0)}-x^2}}\right]\right\} \tag{D.3}$$

and

$$\begin{aligned}
&\frac{\partial}{\partial z}\int_{\rho}^{a}\frac{\mathrm{d}x}{\sqrt{x^2-\rho^2}}\left\{2\Re\left[\operatorname{arctanh}\left(\frac{l_1(x,s,z)\sqrt{s\rho \mathrm{e}^{-\mathrm{i}(\phi-\phi_0)}-x^2}}{x\sqrt{s^2-l_1^2(x,s,z)}}\right)\frac{x}{\sqrt{s\rho \mathrm{e}^{-\mathrm{i}(\phi-\phi_0)}-x^2}}\right]-\arctan\left[\frac{l_1(x,s,z)}{\sqrt{s^2-l_1^2(x,s,z)}}\right]\right\}\\
&=\int_{x=\rho}^{x=a}\frac{\mathrm{d}l_1(x,s,z)}{\sqrt{[s^2-l_1^2(x,s,z)][l_1^2(x,s,z)-\rho^2]+z^2l_1^2(x,s,z)}}\frac{zl_1(x,s,z)}{\sqrt{s^2-l_1^2(x,s,z)}}\times\\
&\left\{\frac{1}{\sqrt{s^2+z^2-l_1^2(x,s,z)}}-2\Re\left[\frac{s\sqrt{s^2+z^2-l_1^2(x,s,z)}}{s[s^2+z^2-l_1^2(x,s,z)]-\rho[s^2-l_1^2(x,s,z)]\mathrm{e}^{-\mathrm{i}(\phi-\phi_0)}}\right]\right\},
\end{aligned} \tag{D.4}$$

the integral presented in Eq. (D.4) can be evaluated by dividing it into two parts, yielding

$$\begin{aligned}
&\int_{x=\rho}^{x=a}\frac{\mathrm{d}l_1(x,s,z)}{\sqrt{[s^2-l_1^2(x,s,z)][l_1^2(x,s,z)-\rho^2]+z^2l_1^2(x,s,z)}}\frac{zl_1(x,s,z)}{\sqrt{s^2-l_1^2(x,s,z)}}\frac{1}{\sqrt{s^2+z^2-l_1^2(x,s,z)}}\\
&=-\frac{\mathrm{i}}{l_2(\rho,s,z)}\widehat{F}\left[\arcsin\left(\sqrt{\frac{l_2^2(\rho,s,z)-l_2^2(a,s,z)}{l_2^2(\rho,s,z)-l_1^2(\rho,s,z)}}\right),\frac{l_2^2(\rho,s,z)-l_1^2(\rho,s,z)}{l_2^2(\rho,s,z)}\right]
\end{aligned} \tag{D.5}$$

and

$$\begin{aligned}
&\int_{x=\rho}^{x=a}\frac{\mathrm{d}l_1(x,s,z)}{\sqrt{[s^2-l_1^2(x,s,z)][l_1^2(x,s,z)-\rho^2]+z^2l_1^2(x,s,z)}}\frac{zl_1(x,s,z)}{\sqrt{s^2-l_1^2(x,s,z)}}\frac{s\sqrt{s^2+z^2-l_1^2(x,s,z)}}{s[s^2+z^2-l_1^2(x,s,z)]-\rho[s^2-l_1^2(x,s,z)]\mathrm{e}^{-\mathrm{i}(\phi-\phi_0)}}\\
&=\frac{\mathrm{i}}{l_2(\rho,s,z)}\left\{-\widehat{F}\left[\arcsin\left(\sqrt{\frac{l_2^2(\rho,s,z)-l_2^2(a,s,z)}{l_2^2(\rho,s,z)-l_1^2(\rho,s,z)}}\right),\frac{l_2^2(\rho,s,z)-l_1^2(\rho,s,z)}{l_2^2(\rho,s,z)}\right]\right.\\
&\left.+\frac{s\rho}{s\rho-l_2^2(\rho,s,z)\mathrm{e}^{\mathrm{i}(\phi-\phi_0)}}\widehat{\Pi}\left[\frac{l_2^2(\rho,s,z)-l_1^2(\rho,s,z)}{l_2^2(\rho,s,z)-s\rho\mathrm{e}^{-\mathrm{i}(\phi-\phi_0)}};\arcsin\left(\sqrt{\frac{l_2^2(\rho,s,z)-l_2^2(a,s,z)}{l_2^2(\rho,s,z)-l_1^2(\rho,s,z)}}\right),\frac{l_2^2(\rho,s,z)-l_1^2(\rho,s,z)}{l_2^2(\rho,s,z)}\right]\right\},
\end{aligned} \tag{D.6}$$

where $\Re[\#]$ is the real part of #; $\widehat{F}(\phi,k)$, $\widehat{E}(\phi,k)$, and $\widehat{\Pi}(n;\phi,k)$ are the incomplete elliptic integral of the first, second, and third kinds, respectively. Subsequently, differentiating the resulting inner functions once with respect to z allows the kernel $\mathcal{K}_2(\rho,s,\phi,\phi_0;c_{mnq})$ in Eq. (C.9) to be expressed as

$$\begin{aligned}
\mathcal{K}_2=&-\lim_{z\to c_{mnq}}\frac{\partial}{\partial z}\left\{\frac{\mathrm{i}}{l_2(\rho,s,z)}\widehat{F}\left[\arcsin\left(\sqrt{\frac{l_2^2(\rho,s,z)-l_2^2(a,s,z)}{l_2^2(\rho,s,z)-l_1^2(\rho,s,z)}}\right),\frac{l_2^2(\rho,s,z)-l_1^2(\rho,s,z)}{l_2^2(\rho,s,z)}\right]\right.\\
&+2\Re\left[\frac{\mathrm{i}}{l_2(\rho,s,z)}\left\{-\widehat{F}\left[\arcsin\left(\sqrt{\frac{l_2^2(\rho,s,z)-l_2^2(a,s,z)}{l_2^2(\rho,s,z)-l_1^2(\rho,s,z)}}\right),\frac{l_2^2(\rho,s,z)-l_1^2(\rho,s,z)}{l_2^2(\rho,s,z)}\right]\right.\right.\\
&\left.\left.\left.+\frac{s\rho}{s\rho-l_2^2(\rho,s,z)\mathrm{e}^{\mathrm{i}(\phi-\phi_0)}}\widehat{\Pi}\left[\frac{l_2^2(\rho,s,z)-l_1^2(\rho,s,z)}{l_2^2(\rho,s,z)-s\rho\mathrm{e}^{-\mathrm{i}(\phi-\phi_0)}};\arcsin\left(\sqrt{\frac{l_2^2(\rho,s,z)-l_2^2(a,s,z)}{l_2^2(\rho,s,z)-l_1^2(\rho,s,z)}}\right),\frac{l_2^2(\rho,s,z)-l_1^2(\rho,s,z)}{l_2^2(\rho,s,z)}\right]\right\}\right]\right\}.
\end{aligned} \tag{D.7}$$

where

$$\begin{aligned}
&\frac{\partial}{\partial z}\left\{\frac{\mathrm{i}}{l_2(\rho,s,z)}\widehat{F}\left[\arcsin\left(\sqrt{\frac{l_2^2(\rho,s,z)-l_2^2(a,s,z)}{l_2^2(\rho,s,z)-l_1^2(\rho,s,z)}}\right),\frac{l_2^2(\rho,s,z)-l_1^2(\rho,s,z)}{l_2^2(\rho,s,z)}\right]\right\}\\
&=\frac{\mathrm{i}}{l_1(\rho)l_2(\rho)[l_1^2(\rho)-l_2^2(\rho)]\sqrt{[l_1^2(\rho)-l_2^2(a)][l_2^2(a)-l_2^2(\rho)]}}\left\{\frac{\partial l_2(\rho)}{\partial z}l_1(\rho)l_2(a)[l_2^2(a)-l_1^2(\rho)]\right.\\
&+\frac{\partial l_2(a)}{\partial z}l_1(\rho)l_2(\rho)[l_1^2(\rho)-l_2^2(\rho)]+\frac{\partial l_1(\rho)}{\partial z}l_2(a)l_2(\rho)[l_2^2(\rho)-l_2^2(a)]\\
&+\sqrt{[l_1^2(\rho)-l_2^2(a)][l_2^2(a)-l_2^2(\rho)]}\left\{l_2(\rho)\left[\frac{\partial l_2(\rho)}{\partial z}l_1(\rho)-\frac{\partial l_1(\rho)}{\partial z}l_2(\rho)\right]\widehat{E}\left[\arcsin\left(\sqrt{\frac{l_2^2(\rho)-l_2^2(a)}{l_2^2(\rho)-l_1^2(\rho)}}\right),1-\frac{l_1^2(\rho)}{l_2^2(\rho)}\right]\right.\\
&\left.\left.+l_1(\rho)\left[\frac{\partial l_1(\rho)}{\partial z}l_1(\rho)-\frac{\partial l_2(\rho)}{\partial z}l_2(\rho)\right]\widehat{F}\left[\arcsin\left(\sqrt{\frac{l_2^2(\rho)-l_2^2(a)}{l_2^2(\rho)-l_1^2(\rho)}}\right),1-\frac{l_1^2(\rho)}{l_2^2(\rho)}\right]\right\}\right\},
\end{aligned}\tag{D.8}$$

and

$$\begin{aligned}
&\frac{\partial}{\partial z}\left\{\frac{\mathrm{i}}{l_2(\rho,s,z)}\frac{s\rho}{s\rho-l_2^2(\rho,s,z)\mathrm{e}^{\mathrm{i}(\phi-\phi_0)}}\widehat{\Pi}\left[\frac{l_2^2(\rho,s,z)-l_1^2(\rho,s,z)}{l_2^2(\rho,s,z)-s\rho\mathrm{e}^{-\mathrm{i}(\phi-\phi_0)}};\arcsin\left(\sqrt{\frac{l_2^2(\rho,s,z)-l_2^2(a,s,z)}{l_2^2(\rho,s,z)-l_1^2(\rho,s,z)}}\right),\frac{l_2^2(\rho,s,z)-l_1^2(\rho,s,z)}{l_2^2(\rho,s,z)}\right]\right\}\\
&=\mathrm{i}\mathrm{e}^{\mathrm{i}\phi_0}s\rho\sqrt{[l_1^2(\rho)-l_2^2(a)][l_2^2(a)-l_2^2(\rho)]}\left[\frac{\frac{\partial l_1(\rho)}{\partial z}l_2(a)}{l_1(\rho)[l_2^2(a)-l_1^2(\rho)][l_1^2(\rho)-l_2^2(\rho)]\left[\mathrm{e}^{\mathrm{i}\phi}l_1^2(\rho)-\mathrm{e}^{\mathrm{i}\phi_0}s\rho\right]}\right.\\
&\left.+\frac{\frac{\partial l_2(a)}{\partial z}}{[l_2^2(a)-l_2^2(\rho)][l_1^2(\rho)-l_2^2(a)]\left[\mathrm{e}^{\mathrm{i}\phi}l_2^2(a)-\mathrm{e}^{\mathrm{i}\phi_0}s\rho\right]}+\frac{\frac{\partial l_2(\rho)}{\partial z}l_2(a)}{l_2(\rho)[l_2^2(a)-l_2^2(\rho)][l_2^2(\rho)-l_1^2(\rho)]\left[\mathrm{e}^{\mathrm{i}\phi}l_2^2(\rho)-\mathrm{e}^{\mathrm{i}\phi_0}s\rho\right]}\right]\\
&+\frac{\mathrm{i}\mathrm{e}^{\mathrm{i}\phi_0}s\rho}{l_1(\rho)l_2(\rho)[l_1^2(\rho)-l_2^2(\rho)]\left[\mathrm{e}^{\mathrm{i}\phi}l_1^2(\rho)-\mathrm{e}^{\mathrm{i}\phi_0}s\rho\right]\left[\mathrm{e}^{\mathrm{i}\phi}l_2^2(\rho)-\mathrm{e}^{\mathrm{i}\phi_0}s\rho\right]^2}\left\{l_2(\rho)\left[\mathrm{e}^{\mathrm{i}\phi}l_2^2(\rho)-\mathrm{e}^{\mathrm{i}\phi_0}s\rho\right]\left[\mathrm{e}^{\mathrm{i}\phi}\left(\frac{\partial l_2(\rho)}{\partial z}l_1^3(\rho)-\frac{\partial l_1(\rho)}{\partial z}l_2^3(\rho)\right)\right.\right.\\
&\left.-\mathrm{e}^{\mathrm{i}\phi_0}s\rho\left(\frac{\partial l_2(\rho)}{\partial z}l_1(\rho)-\frac{\partial l_1(\rho)}{\partial z}l_2(\rho)\right)\right]\widehat{E}\left[\arcsin\left(\sqrt{\frac{l_2^2(\rho)-l_2^2(a)}{l_2^2(\rho)-l_1^2(\rho)}}\right),1-\frac{l_1^2(\rho)}{l_2^2(\rho)}\right]+l_1(\rho)\left[\mathrm{e}^{\mathrm{i}\phi}l_2^2(\rho)-\mathrm{e}^{\mathrm{i}\phi_0}s\rho\right]\times\\
&\left[-\mathrm{e}^{\mathrm{i}\phi}l_1(\rho)l_2(\rho)\left(\frac{\partial l_2(\rho)}{\partial z}l_1(\rho)-\frac{\partial l_1(\rho)}{\partial z}l_2(\rho)\right)+\mathrm{e}^{\mathrm{i}\phi_0}s\rho\left(-\frac{\partial l_1(\rho)}{\partial z}l_1(\rho)+\frac{\partial l_2(\rho)}{\partial z}l_2(\rho)\right)\right]\widehat{F}\left[\arcsin\left(\sqrt{\frac{l_2^2(\rho)-l_2^2(a)}{l_2^2(\rho)-l_1^2(\rho)}}\right),1-\frac{l_1^2(\rho)}{l_2^2(\rho)}\right]\\
&+l_1(\rho)\mathrm{e}^{\mathrm{i}\phi}[l_1^2(\rho)-l_2^2(\rho)]\left[\mathrm{e}^{\mathrm{i}\phi}l_1(\rho)l_2(\rho)\left(\frac{\partial l_2(\rho)}{\partial z}l_1(\rho)+\frac{\partial l_1(\rho)}{\partial z}l_2(\rho)\right)-\mathrm{e}^{\mathrm{i}\phi_0}s\rho\left(\frac{\partial l_1(\rho)}{\partial z}l_1(\rho)+\frac{\partial l_2(\rho)}{\partial z}l_2(\rho)\right)\right]\times\\
&\left.\left.\widehat{\Pi}\left[\frac{l_2^2(\rho)-l_1^2(\rho)}{l_2^2(\rho)-s\rho\mathrm{e}^{-\mathrm{i}(\phi-\phi_0)}};\arcsin\left(\sqrt{\frac{l_2^2(\rho)-l_2^2(a)}{l_2^2(\rho)-l_1^2(\rho)}}\right),1-\frac{l_1^2(\rho)}{l_2^2(\rho)}\right]\right\},
\end{aligned}\tag{D.9}$$

with $\frac{\partial l_1(\rho)}{\partial z}=-\frac{zl_1(\rho,s,z)}{l_2^2(\rho,s,z)-l_1^2(\rho,s,z)}$ and $\frac{\partial l_2(\rho)}{\partial z}=\frac{zl_2(\rho,s,z)}{l_2^2(\rho,s,z)-l_1^2(\rho,s,z)}$.

Using the solutions to Abel integral equations, the inversion of Eq. (C.13) is performed by sequentially applying $\mathcal{L}\left(\frac{1}{t}\right)\frac{\mathrm{d}}{\mathrm{d}t}\int_0^t\frac{\rho\mathrm{d}\rho}{\sqrt{t^2-\rho^2}}\mathcal{L}(\rho)$ and $\mathcal{L}(r)\frac{\mathrm{d}}{\mathrm{d}r}\int_r^a\frac{t\mathrm{d}t}{\sqrt{t^2-r^2}}\mathcal{L}\left(\frac{1}{t}\right)$, which leads to

$$\begin{aligned}
&\omega_1(r,\phi)+\frac{1}{\pi^2}\sum_{\substack{m=0\\(m,n,q)\neq(0,0,0)}}^{+\infty}\sum_{n=0}^{+\infty}\sum_{q=0}^{+\infty}\mathcal{D}_{mnq}\int_0^{2\pi}\int_0^a\left\{-\frac{\mathcal{L}(r)}{r}\frac{\mathrm{d}}{\mathrm{d}r}\int_r^a\frac{t\mathrm{d}t}{\sqrt{t^2-r^2}}\frac{\frac{\partial l_1(t,\rho_0,c_{mnq})}{\partial t}\mathcal{G}\left[\frac{\rho_0}{l_2^2(t,\rho_0,c_{mnq})},\phi-\phi_0\right]}{\sqrt{\rho_0^2-l_1^2(t,\rho_0,c_{mnq})}}\right\}\omega_1(\rho_0,\phi_0)\rho_0\mathrm{d}\rho_0\mathrm{d}\phi_0\\
&=-\frac{\mathcal{L}(r)}{\pi^2 r}\frac{\mathrm{d}}{\mathrm{d}r}\int_r^a\frac{t\mathrm{d}t}{\sqrt{t^2-r^2}}\mathcal{L}\left(\frac{1}{t^2}\right)\frac{\mathrm{d}}{\mathrm{d}t}\int_0^t\frac{\mathcal{L}(\rho)\mathcal{Q}(\rho,\phi)\rho\mathrm{d}\rho}{\mathcal{D}_0\sqrt{t^2-\rho^2}},
\end{aligned}\tag{D.10}$$

where

$$\begin{aligned}\mathcal{K}_1(r,\rho_0,\phi,\phi_0;c_{mnq}) &:= -\frac{\mathcal{L}(r)}{r}\frac{\mathrm{d}}{\mathrm{d}r}\int_r^a \frac{t\mathrm{d}t}{\sqrt{t^2-r^2}}\frac{\frac{\partial l_1(t,\rho_0,c_{mnq})}{\partial t}\mathcal{G}\left[\frac{\rho_0}{l_2^2(t,\rho_0,c_{mnq})},\phi-\phi_0\right]}{\sqrt{\rho_0^2-l_1^2(t,\rho_0,c_{mnq})}}\\ &= \frac{c_{mnq}}{\left(\sqrt{r^2+\rho_0^2-2r\rho_0\cos(\phi-\phi_0)+c_{mnq}^2}\right)^3}\\ &\times\left[\frac{a\sqrt{r^2+\rho_0^2-2r\rho_0\cos(\phi-\phi_0)+c_{mnq}^2}}{\sqrt{a^2-l_1^2(a,\rho_0,c_{mnq})}\sqrt{a^2-r^2}}+\arctan\left(\frac{\sqrt{a^2-l_1^2(a,\rho_0,c_{mnq})}\sqrt{a^2-r^2}}{a\sqrt{r^2+\rho_0^2-2r\rho_0\cos(\phi-\phi_0)+c_{mnq}^2}}\right)\right].\end{aligned} \tag{D.11}$$

Appendix E. Contraction operator

In order to prove that $\mathcal{N}_1$ and $\mathcal{N}_2$ are contraction mappings, we first evaluate two key integrals. The integral $\int_0^{2\pi}\int_0^a \mathcal{K}_2(\rho,s,\phi,\phi_0;c_{mnq})s\mathrm{d}s\mathrm{d}\phi_0$ is obtained as

$$\begin{aligned}&\lim_{z\to c_{mnq}}\frac{\partial^2}{\partial z^2}\int_0^{2\pi}\int_0^a\int_\rho^a\frac{\mathrm{d}x}{\sqrt{x^2-\rho^2}}\int_{y=0}^{y=x}\frac{\mathcal{G}\left[\frac{l_1^2(y,s,z)\rho}{sx^2},\phi-\phi_0\right]\mathrm{d}l_1(y,s,z)}{\sqrt{s^2-l_1^2(y,s,z)}}s\mathrm{d}s\mathrm{d}\phi_0\\ &=-2\pi\lim_{z\to c_{mnq}}\frac{\partial}{\partial z}\int_0^a\int_{x=\rho}^{x=a}\frac{\mathrm{d}l_1(x,s,z)}{\sqrt{[s^2-l_1^2(x,s,z)][l_1^2(x,s,z)-\rho^2]+z^2l_1^2(x,s,z)}}\frac{zl_1(x,s,z)}{\sqrt{s^2-l_1^2(x,s,z)}\sqrt{s^2+z^2-l_1^2(x,s,z)}}s\mathrm{d}s\\ &=2\pi\int_{x=\rho}^{x=a}\frac{l_1(x,a,c_{mnq})\sqrt{a^2-l_1^2(x,a,c_{mnq})}}{\sqrt{[l_1^2(x,a,c_{mnq})-\rho^2][a^2-l_1^2(x,a,c_{mnq})]+c_{mnq}^2l_1^2(x,a,c_{mnq})}}\frac{\mathrm{d}l_1(x,a,c_{mnq})}{\sqrt{a^2+z^2-l_1^2(x,a,c_{mnq})}}\\ &=-\frac{2\pi\mathrm{i}c_{mnq}}{l_2(\rho,a,c_{mnq})}\left\{\widehat{F}\left[\arcsin\left(\sqrt{\frac{l_2^2(\rho,a,c_{mnq})-\rho^2l_1^2(a,a,c_{mnq})/a^2}{l_2^2(\rho,a,c_{mnq})-l_1^2(\rho,a,c_{mnq})}}\right),\frac{l_2^2(\rho,a,c_{mnq})-l_1^2(\rho,a,c_{mnq})}{l_2^2(\rho,a,c_{mnq})}\right]+\frac{\rho^2}{[l_2^2(\rho,a,c_{mnq})-\rho^2]}\right.\\ &\left.\times\widehat{\Pi}\left[\frac{l_2^2(\rho,a,c_{mnq})-l_1^2(\rho,a,c_{mnq})}{l_2^2(\rho,a,c_{mnq})-\rho^2};\arcsin\left(\sqrt{\frac{l_2^2(\rho,a,c_{mnq})-\rho^2l_1^2(a,a,c_{mnq})/a^2}{l_2^2(\rho,a,c_{mnq})-l_1^2(\rho,a,c_{mnq})}}\right),\frac{l_2^2(\rho,a,c_{mnq})-l_1^2(\rho,a,c_{mnq})}{l_2^2(\rho,a,c_{mnq})}\right]\right\},\end{aligned} \tag{E.1}$$

while $\int_0^{2\pi}\int_0^a \mathcal{K}_1(\rho,\rho_0,\phi,\phi_0;c_{mnq})\frac{\rho_0\mathrm{d}\rho_0\mathrm{d}\phi_0}{\sqrt{a^2-\rho_0^2}}$ is derived as

$$\begin{aligned}&\int_0^{2\pi}\int_0^a\frac{c_{mnq}}{\left[\sqrt{\rho^2+\rho_0^2-2\rho\rho_0\cos(\phi-\phi_0)+c_{mnq}^2}\right]^3}\left\{\frac{a\sqrt{\rho^2+\rho_0^2-2\rho\rho_0\cos(\phi-\phi_0)+c_{mnq}^2}}{\sqrt{a^2-l_1^2(\rho_0,a,c_{mnq})}\sqrt{a^2-\rho^2}}\right.\\ &\left.+\arctan\left[\frac{\sqrt{a^2-l_1^2(\rho_0,a,c_{mnq})}\sqrt{a^2-\rho^2}}{a\sqrt{\rho^2+\rho_0^2-2\rho\rho_0\cos(\phi-\phi_0)+c_{mnq}^2}}\right]\frac{\rho_0\mathrm{d}\rho_0\mathrm{d}\phi_0}{\sqrt{a^2-\rho_0^2}}\right\}=\frac{2\pi}{\sqrt{a^2-\rho^2}}\arctan\left[\sqrt{\frac{l_1(a,a,c_{mnq})}{l_2(a,a,c_{mnq})}}\right]\\ &+\frac{\pi\sqrt{l_2^2(\rho,a,c_{mnq})-a^2}}{l_2^2(\rho,a,c_{mnq})-l_1^2(\rho,a,c_{mnq})}\operatorname{arctanh}\left\{\frac{2l_1^2(\rho,a,c_{mnq})\sqrt{a^2-\rho^2}}{[\rho^2+l_1^2(\rho,a,c_{mnq})]\sqrt{a^2-l_1^2(\rho,a,c_{mnq})}}\right\}\\ &+\frac{\pi\sqrt{a^2-l_1^2(\rho,a,c_{mnq})}}{l_2^2(\rho,a,c_{mnq})-l_1^2(\rho,a,c_{mnq})}\arctan\left\{\frac{2l_2^2(\rho,a,c_{mnq})\sqrt{a^2-\rho^2}}{[\rho^2+l_2^2(\rho,a,c_{mnq})]\sqrt{l_2^2(\rho,a,c_{mnq})-a^2}}\right\}.\end{aligned} \tag{E.2}$$

From Eqs. (C.14) and (C.15), it follows that for any $\omega_1^*\in C(\mathscr{D})$, the integral operator $\mathcal{N}_1: C(\mathscr{D})\to C(\mathscr{D})$, where $\mathscr{D}=[0,a]\times[0,2\pi]$. Introducing the supremum norm $\|\omega_1^*(\rho,\phi)\|_\infty=\sup_{(\rho,\phi)\in\mathscr{D}}|\omega_1^*(\rho,\phi)|$ and the induced metric $d_k[\omega_1^*-(\omega_1^*)^{[k]}]=\|\omega_1^*-(\omega_1^*)^{[k]}\|_\infty$, the

condition for uniform convergence is $\lim_{k\to\infty}\|\omega_1^* - (\omega_1^*)^{[k]}\|_\infty = 0$. The integral operator $\mathcal{N}_1$ admits the estimate

$$
\begin{aligned}
|\mathcal{N}_1[\omega_1^*] - \mathcal{N}_1[(\omega_1^*)^{[k]}]| &= \left| \sum_{\substack{m=0\\(m,n,q)\neq(0,0,0)}}^{+\infty}\sum_{n=0}^{+\infty}\sum_{q=0}^{+\infty} \frac{\mathcal{D}_{mnq}}{\pi^2} \iint_{\mathscr{D}} \mathcal{K}_1(\rho,\rho_0,\phi,\phi_0;c_{mnq}) \frac{\sqrt{a^2-\rho^2}}{\sqrt{a^2-\rho_0^2}} [\omega_1^*(\rho_0,\phi_0) - (\omega_1^*)^{[k]}(\rho_0,\phi_0)] \mathrm{d}S \right| \\
&\leqslant \sum_{\substack{m=0\\(m,n,q)\neq(0,0,0)}}^{+\infty}\sum_{n=0}^{+\infty}\sum_{q=0}^{+\infty} \left| \frac{\mathcal{D}_{mnq}}{\pi^2} \iint_{\mathscr{D}} \mathcal{K}_1(\rho,\rho_0,\phi,\phi_0;c_{mnq}) \frac{\sqrt{a^2-\rho^2}}{\sqrt{a^2-\rho_0^2}} [\omega_1^*(\rho_0,\phi_0) - (\omega_1^*)^{[k]}(\rho_0,\phi_0)] \mathrm{d}S \right| \\
&\leqslant \sum_{\substack{m=0\\(m,n,q)\neq(0,0,0)}}^{+\infty}\sum_{n=0}^{+\infty}\sum_{q=0}^{+\infty} \frac{|\mathcal{D}_{mnq}|}{\pi^2} \iint_{\mathscr{D}} |\mathcal{K}_1(\rho,\rho_0,\phi,\phi_0;c_{mnq})| \left| \frac{\sqrt{a^2-\rho^2}}{\sqrt{a^2-\rho_0^2}} \right| |\omega_1^*(\rho_0,\phi_0) - (\omega_1^*)^{[k]}(\rho_0,\phi_0)| \mathrm{d}S \\
&= \sum_{\substack{m=0\\(m,n,q)\neq(0,0,0)}}^{+\infty}\sum_{n=0}^{+\infty}\sum_{q=0}^{+\infty} \frac{|\mathcal{D}_{mnq}|}{\pi^2} \iint_{\mathscr{D}} \mathcal{K}_1(\rho,\rho_0,\phi,\phi_0;c_{mnq}) \frac{\sqrt{a^2-\rho^2}}{\sqrt{a^2-\rho_0^2}} |\omega_1^*(\rho_0,\phi_0) - (\omega_1^*)^{[k]}(\rho_0,\phi_0)| \mathrm{d}S \\
&\leqslant \sum_{\substack{m=0\\(m,n,q)\neq(0,0,0)}}^{+\infty}\sum_{n=0}^{+\infty}\sum_{q=0}^{+\infty} \frac{|\mathcal{D}_{mnq}|}{\pi^2} \iint_{\mathscr{D}} \mathcal{K}_1(\rho,\rho_0,\phi,\phi_0;c_{mnq}) \frac{\sqrt{a^2-\rho^2}}{\sqrt{a^2-\rho_0^2}} \|\omega_1^*(\rho_0,\phi_0) - (\omega_1^*)^{[k]}(\rho_0,\phi_0)\|_\infty \mathrm{d}S \\
&= \|\omega_1^*(\rho_0,\phi_0) - (\omega_1^*)^{[k]}(\rho_0,\phi_0)\|_\infty \sum_{\substack{m=0\\(m,n,q)\neq(0,0,0)}}^{+\infty}\sum_{n=0}^{+\infty}\sum_{q=0}^{+\infty} \frac{|\mathcal{D}_{mnq}|}{\pi^2} \iint_{\mathscr{D}} \mathcal{K}_1(\rho,\rho_0,\phi,\phi_0;c_{mnq}) \frac{\sqrt{a^2-\rho^2}}{\sqrt{a^2-\rho_0^2}} \mathrm{d}S \\
&\leqslant \epsilon \|\omega_1^*(\rho_0,\phi_0) - (\omega_1^*)^{[k]}(\rho_0,\phi_0)\|_\infty .
\end{aligned}
\tag{E.3}
$$

If the supremum of the left-hand side satisfies $\sup_{(\rho,\phi)\in\mathscr{D}} |\mathcal{N}_1[\omega_1^*] - \mathcal{N}_1[(\omega_1^*)^{[k]}]| \leqslant \epsilon \|\omega_1^* - (\omega_1^*)^{[k]}\|_\infty$ with $\epsilon < 1$, the operator $\mathcal{N}_1$ is a contraction mapping in accordance with the Banach-Caccioppoli theorem (Jachymski et al., 2024). Since $C(\mathscr{D})$ is complete under the supremum norm, a unique solution $\omega_1^* \in C(\mathscr{D})$ exists for the integral equation. For any initial guess $(\omega_1^*)^{[0]}$, the sequence generated by the iterative scheme $(\omega_1^*)^{[k+1]} = \mathcal{N}_1[(\omega_1^*)^{[k]}]$ converges uniformly to ω_1^*, which is precisely the fixed point of $\mathcal{N}_1$ satisfying $\omega_1^* = \mathcal{N}_1[\omega_1^*]$. Besides, we obtain $\|(\omega_1^*)^{[k]} - \omega_1^*\| \leqslant \frac{\epsilon^k}{1-\epsilon}\|(\omega_1^*)^{[1]} - (\omega_1^*)^{[0]}\| (k \geqslant 0)$ for the *a priori* error estimate, and $\|(\omega_1^*)^{[k]} - \omega_1^*\| \leqslant \frac{1}{1-\epsilon}\|(\omega_1^*)^{[k+1]} - (\omega_1^*)^{[k]}\| (k \geqslant 0)$ for the *a posteriori* counterpart.

From Eq. (E.2), the series of continuous functions $\left\{ \frac{|\mathcal{D}_{mnq}|}{\pi^2} \iint_{\mathscr{D}} \mathcal{K}_1(\rho,\rho_0,\phi,\phi_0;c_{mnq}) \frac{\sqrt{a^2-\rho^2}}{\sqrt{a^2-\rho_0^2}} \mathrm{d}S \right\}$ converges uniformly, which implies that the function $\sum_{\substack{m=0\\(m,n,q)\neq(0,0,0)}}^{+\infty}\sum_{n=0}^{+\infty}\sum_{q=0}^{+\infty} \frac{|\mathcal{D}_{mnq}|}{\pi^2} \iint_{\mathscr{D}} \mathcal{K}_1(\rho,\rho_0,\phi,\phi_0;c_{mnq}) \frac{\sqrt{a^2-\rho^2}}{\sqrt{a^2-\rho_0^2}} \mathrm{d}S$ presented in Eq. (E.3) is continuous. Since $\lim_{c\to 0} \iint_{\mathscr{D}} \mathcal{K}_1(\rho,\rho_0,\phi,\phi_0;c_{mnq}) \frac{\sqrt{a^2-\rho^2}}{\sqrt{a^2-\rho_0^2}} \mathrm{d}S = 0$, and the function is continuous, there exists a constant $c \in \mathbb{R}^+$ such that $\sum_{\substack{m=0\\(m,n,q)\neq(0,0,0)}}^{+\infty}\sum_{n=0}^{+\infty}\sum_{q=0}^{+\infty} \frac{|\mathcal{D}_{mnq}|}{\pi^2} \iint_{\mathscr{D}} \mathcal{K}_1(\rho,\rho_0,\phi,\phi_0;c_{mnq}) \frac{\sqrt{a^2-\rho^2}}{\sqrt{a^2-\rho_0^2}} \mathrm{d}S < \epsilon < 1$. We can also verify that $\lim_{c\to+\infty} \iint_{\mathscr{D}} \mathcal{K}_1(\rho,\rho_0,\phi,\phi_0;c_{mnq}) \frac{\sqrt{a^2-\rho^2}}{\sqrt{a^2-\rho_0^2}} \mathrm{d}S = 0$, which corresponds to the classical half-space case. Similarly, the series of functions involving the kernel $\mathcal{K}_2$ can be proved concerning Eq. (E.1) and $\lim_{c\to+\infty} \iint_{\mathscr{D}} \mathcal{K}_2(\rho,s,\phi,\phi_0;c_{mnq}) \mathrm{d}S = 0$.

Appendix F. Indentation on a wavy surface induced by surface instability

Experimental evidence demonstrates that surface instability and self-assembly in soft materials, such as polymers, enable the generation of tunable micro and nanoscale patterns with a regular periodicity. These patterns can be replicated and transferred, enabling pattern transfer printing. A notable example is the work of Chou and Zhuang (1999) on nanoimprint lithography, where a flat rigid punch moving vertically toward a polymethylmethacrylate (PMMA) thin film induced the formation of a regular micropillar array on the film surface. This discovery led to lithographically induced self-assembly (LISA), which has become an efficient method for fabricating surface patterns on thin films. The LISA technique has prompted a wealth of theoretical, numerical, and experimental studies for modulating surface topography (Sharma and Khanna, 1998; Schäffer et al., 2000; Huang et al., 2008).

This section focuses on a simple computational exploration of the coupling between waviness arising from surface instability in a hyperelastic material and the contact behavior with a rigid indenter. When the temperature increment is assumed to be uniform over the whole field, the contribution of this increment in Eq. (6) allows us to neglect the thermal variables in the hyperelastic half-space. As derived in Section 5 of Chen et al. (2026), an axisymmetric nontrivial solution exists, consisting of Bessel functions and decaying exponential functions, which corresponds to the assumption in Section 4. Under the total Lagrangian framework, we may establish

the total potential energy as

$$\Pi(\mathbf{U}) := \Pi_{\text{int}}(\mathbf{U}) + \Pi_{\text{ext}}(\mathbf{U}) = \int_{\mathcal{B}_r} \Omega(\mathbf{F}_e)\mathrm{d}V - \int_{\partial\mathcal{B}_r^\sigma} \mathbf{t}_A \cdot \mathbf{U}\mathrm{d}A, \tag{F.1}$$

the first variation of which is expressed as

$$\begin{aligned}\delta_1\Pi(\mathbf{U}) &:= \frac{\mathrm{d}}{\mathrm{d}\epsilon_1}\Pi(\mathbf{U}+\epsilon_1\delta_1\mathbf{U})\Big|_{\epsilon_1=0}\\ &= \int_{\mathcal{B}_r} \frac{\partial\Omega(\mathbf{F}_e)}{\partial\mathbf{F}_e}\cdot\cdot\,\mathrm{Grad}\,\delta_1\mathbf{U}\mathrm{d}V - \int_{\partial\mathcal{B}_r^\sigma}\mathbf{t}_A\cdot\delta_1\mathbf{U}\mathrm{d}A \qquad \forall\delta_1\mathbf{U}\in\mathcal{U}_0\\ &= \int_{\mathcal{B}_r}\mathbf{S}_e\cdot\cdot\,\mathrm{sym}\left(\mathbf{F}_e^{\mathrm{T}}\cdot\mathrm{Grad}\,\delta_1\mathbf{U}\right)\mathrm{d}V - \int_{\partial\mathcal{B}_r^\sigma}\mathbf{t}_A\cdot\delta_1\mathbf{U}\mathrm{d}A,\end{aligned} \tag{F.2}$$

where $\mathcal{U}_0 := \{\delta_1\mathbf{U} : \mathcal{B}_r \to \mathbb{R}^3 | \delta_1\mathbf{U} = \mathbf{0}\ \text{on}\ \partial\mathcal{B}_r^u\}$ is the space of displacement variation that is kinematically admissible and $\mathrm{sym}\left(\mathbf{F}_e^{\mathrm{T}}\cdot\mathrm{Grad}\,\delta_1\mathbf{U}\right)$ is the variation of the Green -Lagrange strain $\delta_1\boldsymbol{\epsilon}_{\text{GL}}$, with $\mathrm{sym}(\#) := \left(\#+\#^{\mathrm{T}}\right)/2$. To solve the nonlinear Eq. (F.2) through Newton-Raphson method, we consider the second variation of the total potential energy

$$\begin{aligned}\delta_2\delta_1\Pi(\mathbf{U}) &= \frac{\mathrm{d}}{\mathrm{d}\epsilon_2}\delta_1\Pi(\mathbf{U}+\epsilon_2\delta_2\mathbf{U})\Big|_{\epsilon_2=0}\\ &= \int_{\mathcal{B}_r}\mathrm{Grad}\,\delta_1\mathbf{U}\cdot\cdot\frac{\partial^2\Omega(\mathbf{F}_e)}{\partial\mathbf{F}_e\partial\mathbf{F}_e}\cdot\cdot\,\mathrm{Grad}\,\delta_2\mathbf{U}\mathrm{d}V\\ &= \int_{\mathcal{B}_r}\left\{\mathrm{sym}\left(\mathbf{F}_e^{\mathrm{T}}\cdot\mathrm{Grad}\,\delta_1\mathbf{U}\right)\cdot\cdot\,4\frac{\partial^2\Omega}{\partial\mathbf{C}_e\partial\mathbf{C}_e}\cdot\cdot\,\mathrm{sym}\left(\mathbf{F}_e^{\mathrm{T}}\cdot\mathrm{Grad}\,\delta_2\mathbf{U}\right) + \mathbf{S}_e\cdot\cdot\left[(\mathrm{Grad}\,\delta_1\mathbf{U})^{\mathrm{T}}\cdot(\mathrm{Grad}\,\delta_2\mathbf{U})\right]\right\}\mathrm{d}V.\end{aligned} \tag{F.3}$$

Therefore, we can solve

$$\delta_2\delta_1\Pi = -(\delta_1\Pi_{\text{int}} + \delta_1\Pi_{\text{ext}}) \tag{F.4}$$

for the displacement field under applied loads. The domain is then discretized, and isoparametric interpolation is performed to describe the position and displacement vectors as $\mathbf{X}^e(\boldsymbol{\iota}) = \sum_{\mathfrak{n}=1}^{n_{\text{node}}}\mathfrak{N}_{\mathfrak{n}}(\boldsymbol{\iota})\mathbf{X}_{\mathfrak{n}}^e$ and $\mathbf{U}^e(\boldsymbol{\iota}) = \sum_{\mathfrak{n}=1}^{n_{\text{node}}}\mathfrak{N}_{\mathfrak{n}}(\boldsymbol{\iota})\mathbf{U}_{\mathfrak{n}}^e$, respectively, where $\iota_k \in [-1,1](k=1,2,3)$. $\mathfrak{N}_{\mathfrak{n}}$ denotes the shape function for the $\mathfrak{n}$-th node among a total of n_{node} nodes. $\mathbf{X}_{\mathfrak{n}}^e$ and $\mathbf{U}_{\mathfrak{n}}^e$ are the position and displacement vectors at the $\mathfrak{n}$-th node, respectively. Thus, the position vector in B^{Π} takes the form of $\mathscr{I}^{\mathrm{T}}\mathbf{x}^e = \mathbf{X}^e + \mathbf{U}^e = \sum_{\mathfrak{n}=1}^{n_{\text{node}}}\mathfrak{N}_{\mathfrak{n}}(\boldsymbol{\iota})(\mathbf{X}_{\mathfrak{n}}^e + \mathbf{U}_{\mathfrak{n}}^e)$. With $\partial\mathfrak{N}_{\mathfrak{n}}/\partial\mathbf{X} = \mathbf{J}^{-1}\partial\mathfrak{N}_{\mathfrak{n}}/\partial\boldsymbol{\iota}$ and the Jacobian matrix $\mathbf{J} = \partial\mathbf{X}/\partial\boldsymbol{\iota}$, the components of Green -Lagrange strain can be formed by the linear and nonlinear components with respect to $\mathbf{U}^e$ as $[\varepsilon_{\text{GL}}^e]_{\alpha\beta} = \left(\left[\mathrm{C}_e^e\right]_{\alpha\beta} - \delta_{\alpha\beta}\right)/2 = \left(\mathrm{U}_{\alpha\mathfrak{n}}^e\mathfrak{N}_{\mathfrak{n},\beta} + \mathrm{U}_{\beta\mathfrak{n}}^e\mathfrak{N}_{\mathfrak{n},\alpha} + \mathrm{U}_{\alpha\mathfrak{n}}^e\mathrm{U}_{\beta\mathfrak{m}}^e\mathfrak{N}_{\mathfrak{n},\gamma}\mathfrak{N}_{\mathfrak{m},\gamma}\right)/2$, where $\mathfrak{m},\mathfrak{n} = 1,\ldots,n_{\text{node}}$. Substituting $\mathbf{U}^e$ and $\boldsymbol{\varepsilon}_{\text{GL}}^e$ into Eqs. (F.2) and (F.3), Eq. (F.4) can be expressed as

$$\begin{aligned}&\int_{\mathcal{B}_r}\left\{\frac{\partial^2\Omega}{\partial\left[\mathrm{C}_e\right]_{\alpha\beta}\partial\left[\mathrm{C}_e\right]_{\eta\mu}}\Big|_{\mathbf{C}_e=\mathbf{C}_e^e}\left[\delta_1\mathrm{U}_{\alpha\mathfrak{n}}^e\mathfrak{N}_{\mathfrak{n},\beta} + \delta_1\mathrm{U}_{\beta\mathfrak{n}}^e\mathfrak{N}_{\mathfrak{n},\alpha} + \delta_1\mathrm{U}_{\alpha\mathfrak{n}}^e\mathrm{U}_{\beta\mathfrak{m}}^e\mathfrak{N}_{\mathfrak{n},\gamma}\mathfrak{N}_{\mathfrak{m},\gamma} + \mathrm{U}_{\alpha\mathfrak{n}}^e\delta_1\mathrm{U}_{\beta\mathfrak{m}}^e\mathfrak{N}_{\mathfrak{n},\gamma}\mathfrak{N}_{\mathfrak{m},\gamma}\right]\times\right.\\ &\left.\left[\delta_2\mathrm{U}_{\eta\mathfrak{p}}^e\mathfrak{N}_{\mathfrak{p},\mu} + \delta_2\mathrm{U}_{\mu\mathfrak{p}}^e\mathfrak{N}_{\mathfrak{p},\eta} + \delta_2\mathrm{U}_{\eta\mathfrak{p}}^e\mathrm{U}_{\mu\mathfrak{q}}^e\mathfrak{N}_{\mathfrak{p},\lambda}\mathfrak{N}_{\mathfrak{q},\lambda} + \mathrm{U}_{\eta\mathfrak{p}}^e\delta_2\mathrm{U}_{\mu\mathfrak{q}}^e\mathfrak{N}_{\mathfrak{p},\lambda}\mathfrak{N}_{\mathfrak{q},\lambda}\right] + 2\frac{\partial\Omega}{\partial\left[\mathrm{C}_e\right]_{\alpha\beta}}\Big|_{\mathbf{C}_e=\mathbf{C}_e^e}\delta_1\mathrm{U}_{\gamma\mathfrak{n}}^e\mathfrak{N}_{\mathfrak{n},\alpha}\delta_2\mathrm{U}_{\gamma\mathfrak{m}}^e\mathfrak{N}_{\mathfrak{m},\beta}\right\}\mathrm{d}V\\ &= \int_{\partial\mathcal{B}_r^\sigma}\left[\mathrm{t}_A\right]_\alpha\mathfrak{N}_{\mathfrak{n}}\delta_1\mathrm{U}_{\alpha\mathfrak{n}}^e\mathrm{d}A - \int_{\mathcal{B}_r}\frac{\partial\Omega}{\partial\left[\mathrm{C}_e\right]_{\alpha\beta}}\Big|_{\mathbf{C}_e=\mathbf{C}_e^e}\left[\delta_1\mathrm{U}_{\alpha\mathfrak{n}}^e\mathfrak{N}_{\mathfrak{n},\beta} + \delta_1\mathrm{U}_{\beta\mathfrak{n}}^e\mathfrak{N}_{\mathfrak{n},\alpha} + \delta_1\mathrm{U}_{\alpha\mathfrak{n}}^e\mathrm{U}_{\beta\mathfrak{m}}^e\mathfrak{N}_{\mathfrak{n},\gamma}\mathfrak{N}_{\mathfrak{m},\gamma} + \mathrm{U}_{\alpha\mathfrak{n}}^e\delta_1\mathrm{U}_{\beta\mathfrak{m}}^e\mathfrak{N}_{\mathfrak{n},\gamma}\mathfrak{N}_{\mathfrak{m},\gamma}\right]\mathrm{d}V,\end{aligned} \tag{F.5}$$

where $\mathfrak{m},\mathfrak{n},\mathfrak{p},\mathfrak{q} = 1,\ldots,n_{\text{node}}$ and $\alpha,\beta,\gamma,\eta,\lambda,\mu = 1,2,3$. Given that $\delta_1\mathbf{U}\in\mathcal{U}_0$, we may collect the coefficients of $\delta_1\mathrm{U}_{\alpha\mathfrak{n}}^e$ on both sides of Eq. (F.5) for all $3n_{\text{node}}$ nodes and set each coefficient to zero. As a result, we obtain $3n_{\text{node}}$ equations expressed in terms of $\delta_2\mathrm{U}_{\alpha\mathfrak{n}}^e$. We then flatten $\delta_2\mathrm{U}_{\alpha\mathfrak{n}}^e$, originally of dimension $3\times n_{\text{node}}$, into a vector of dimension $3n_{\text{node}}\times 1$ following the nodal ordering. Consequently, the equations can be expressed in a compact form $\mathbf{K}^e(\mathbf{U}^e)\delta_2\mathbf{U}_{\text{flat}}^e = -\mathbf{R}^e(\mathbf{U}^e)$, involving the element tangent stiffness matrix $\mathbf{K}^e$, the variation of flattened element nodal displacement vector $\delta_2\mathbf{U}_{\text{flat}}^e$, and the element residual vector $\mathbf{R}^e$. As shown in Eq. (F.3), the tangent stiffness matrix consists of the material stiffness matrix $\mathbf{K}_{\text{mat}}^e$, which arises from the first term, and the geometric stiffness matrix $\mathbf{K}_{\text{geo}}^e$, which originates from the second term. Global assembly is then performed node by node. We first prescribe a reference load $\mathbf{t}_{A0}$ and solve the nonlinear stationary problem $[\mathbf{K}_{\text{mat}} + \mathbf{K}_{\text{geo}}(\mathbf{S}_{e0})]\delta_2\mathbf{U}_{0\,\text{flat}} = -\mathbf{R}(\mathbf{U}_0;\mathbf{t}_{A0})$. With boundary conditions enforced, the iteration $\mathbf{U}_0^{[k+1]} = \mathbf{U}_0^{[k]} + \delta_2\mathbf{U}_0$ is carried out until convergence. Under the proportional loading hypothesis, the geometric stiffness matrix obtained from the stationary problem is then employed to solve the linearized buckling problem $[(\mathbf{K}_{\text{mat}} + \mathbf{K}_{\text{geo}}(\mathbf{U}_0)) + (\mathcal{Y}-1)\mathbf{K}_{\text{geo}}(\mathbf{U}_0)]\hat{\boldsymbol{\Phi}} = \mathbf{0}$. Consequently, the critical load factor $\mathcal{Y}$ and the normalized buckling mode $\hat{\boldsymbol{\Phi}}$ are obtained. When the prescribed reference load exceeds the buckling load, the resulting critical load factor $\mathcal{Y}$ falls below 1. We subsequently reshape the normalized buckling mode $\hat{\boldsymbol{\Phi}}$ into nodal displacement $\mathbf{U}_{\text{imp}}$. Multiplying by a scale factor $\mathfrak{w}$, we apply these displacements as a pre-imposed buckling imperfection to the configuration $\mathcal{B}_r$. This yields a new configuration $\mathcal{B}_{\text{imp}}$, whose position vector is expressed as $\widehat{\mathscr{I}^{\mathrm{T}}}\mathbf{X}_{\text{imp}} = \mathbf{X} + \mathfrak{w}\hat{\mathbf{U}}_{\text{imp}}$, where $\hat{\mathbf{U}}_{\text{imp}}$ is the analytical displacement induced by the buckling imperfection. The deformation gradient tensor is then given by $\mathbf{F} = \partial\mathbf{x}/\partial\mathbf{X} = (\partial\mathbf{x}/\partial\mathbf{X}_{\text{imp}})(\partial\mathbf{X}_{\text{imp}}/\partial\mathbf{X}) = \mathbf{F}_{\text{post}}\cdot\mathbf{F}_{\text{imp}}$. Hence, the subsequent contact analysis can be performed on this configuration using an augmented Lagrangian functional $\mathfrak{L}_{\text{ALM}}$ constructed identically to that described in the caption of Fig. 4.

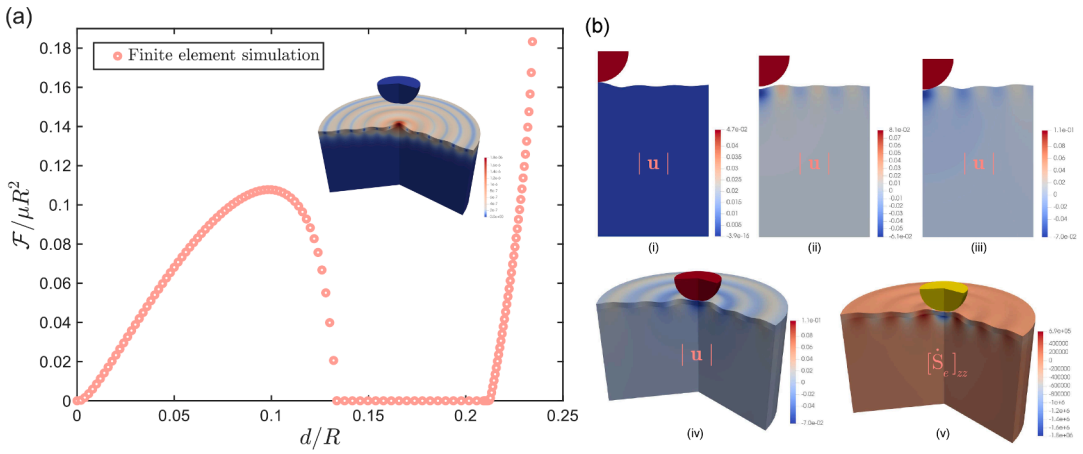


Fig. F.13. The interplay between surface instability of the hyperelastic cylinder and contact with a spherical rigid indenter. (a) presents non-dimensional relations between the non-adhesive contact force and indentation depth, and (b) shows the post-contact distribution of the incremental displacement $|\mathbf{u}|$ and the second Piola-Kirchhoff stress $[\mathrm{S}_e]_{zz}$ when $d = 0.0758$ (m). The finite element result in (a) displays the surface instability morphology before contact, where $\mathcal{Y} = 0.97799$. To enhance visibility of the pattern, the instability mode is scaled up by 2×10^4, and a 0.75π (rad) cut is made through the cylinder to expose the internal displacement field. The coating and substrate are modeled as neoHookean solids with shear moduli $\mu_1 = 10$(MPa) and $\mu_2 = 1$(MPa), respectively, and a common Poisson's ratio $\nu = 0.49$.

To investigate the influence of surface instability on contact in the absence of adhesion, we present a simple numerical example. A hyperelastic cylinder of radius 1 (m) and height 1 (m) is radially pre-compressed such that $\lambda_1 = 0.9$, while the axial direction is left free. A buckling imperfection with a scale factor of $\mathfrak{w} = 1 \times 10^2$ is introduced into the reference configuration. After fixing the bottom surface, a rigid spherical indenter of radius $R = 0.25$ (m) is pressed onto the top surface. Fig. F.13 illustrates the resulting interaction between surface instability of the cylinder and the indenter. Panel (a) reveals that instability-induced waviness introduces discontinuities into the indentation response. An abrupt transition between different instability modes causes the wavy surface that is initially in non-adhesive contact with the indenter to suddenly detach. After thesnap-through, post-indentation brings the indenter back into contact with the newly formed surface. Panel (b) reveals that, upon re-establishing contact after the snap-through, the contact initiates not at the apex of the spherical indenter but at its flank, owing to the surface waviness; consequently, an annular contact zone is formed.

Appendix G. Nomenclature

$(x, y, z);(\rho, \phi, z)$	Cartesian and cylindrical coordinate systems
$\mathcal{B}_r$, $\mathcal{B}^{\mathrm{II}}$, $\mathcal{B}_c$	Reference, initial, and current configurations
$\mathcal{B}_\theta$, $\mathcal{B}^{\mathrm{I}}$	Virtual stress-free and globally compatible configurations
$\mathcal{B}_{\mathrm{imp}}$	Configuration with buckling imperfection
$\mathbf{N}$, $\mathbf{n}$, $\tilde{\mathbf{n}}$	Outward unit normal vectors of $\partial\mathcal{B}_r$, $\partial\mathcal{B}^{\mathrm{II}}$, and $\partial\mathcal{B}_c$
$\mathbf{X}$, $\mathbf{x}$, $\tilde{\mathbf{x}}$	Material point position vectors in $\mathcal{B}_r$, $\mathcal{B}^{\mathrm{II}}$, and $\mathcal{B}_c$
$\mathbf{X}_{\mathrm{imp}}$	Material point position vector in $\mathcal{B}_{\mathrm{imp}}$
$\{\boldsymbol{E}^r_\alpha\}$, $\{\boldsymbol{E}^\theta_s\}$, $\{\boldsymbol{e}_i\}$, $\{\tilde{\boldsymbol{e}}_n\}$	Bases in $\mathcal{B}_r$, $\mathcal{B}_\theta$, $\mathcal{B}^{\mathrm{II}}$, and $\mathcal{B}_c$
$\chi : \mathbf{X} \mapsto \mathbf{x}$	Mapping of material point position vectors between $\mathcal{B}_r$ and $\mathcal{B}^{\mathrm{II}}$
$\mathbf{F} = \mathrm{Grad}\,\chi = \mathbf{F}_e\mathbf{F}_\theta$	Deformation gradient and its decomposition into thermal and elastic contributions
$\mathbf{F}_{\mathrm{imp}}$, $\mathbf{F}_{\mathrm{post}}$	Buckling and post buckling deformation gradients
$\mathbf{b} = \mathbf{F}\mathbf{F}^{\mathrm{T}}$, $\mathbf{b}_e$, $\mathbf{C} = \mathbf{F}^{\mathrm{T}}\mathbf{F}$, $\mathbf{C}_e$	Left and right Cauchy-Green deformation tensors and their elastic contributions
$\mathrm{d}\check{\boldsymbol{A}}$, $\mathrm{d}\check{\boldsymbol{a}}$	Surface elements in the reference ($\mathcal{B}_r$) and initial ($\mathcal{B}^{\mathrm{II}}$) configurations
$\mathrm{d}V$, $\mathrm{d}v$	Volume elements in the reference ($\mathcal{B}_r$) and initial ($\mathcal{B}^{\mathrm{II}}$) configurations
$J = \det\mathbf{F} = J_e J_\theta$	Volume ratio and its decomposition into thermal and elastic contributions
Grad, Div	Gradient and divergence operators in the reference configuration $\mathcal{B}_r$
grad, div	Gradient and divergence operators in the initial configuration $\mathcal{B}^{\mathrm{II}}$
$\mathbf{T}$, $\mathbf{T}_e$, $\mathbf{S}$, $\mathbf{S}_e$	The nominal and second Piola-Kirchhoff stress tensors and their elastic contributions
$\boldsymbol{\tau} = J^{-1}\mathbf{F}\mathbf{T}$	Cauchy stress tensor
$\tilde{\mathbf{T}}$, $\tilde{\mathbf{F}}$, $\tilde{J}$	The nominal stress tensor, deformation gradient, and volume ratio in $\mathcal{B}_c$
$\mathbf{F}^{\mathrm{I}}_e$, $\mathbf{F}^{\mathrm{II}}_e$	The deformation gradients from $\mathcal{B}_\theta$ to $\mathcal{B}^{\mathrm{I}}$ and from $\mathcal{B}^{\mathrm{I}}$ to $\mathcal{B}^{\mathrm{II}}$

$\boldsymbol{\kappa}$	Coefficient of thermal expansion
ζ	Thermal conductivity
Θ, Θ_{ref}	Temperature and its reference counterpart
$\mathbf{t}_A$, $\mathbf{t}_a$	Surface traction on $\partial\mathcal{B}_r$ and $\partial\mathcal{B}^{\text{II}}$
$\Omega(\mathbf{F}_e)$	Energy density function per reference volume
$I_m(\mathbf{C}_e)$	Invariants ($m = 1, 2, 3$)
Ω_m, Ω_{mn}	Partial derivatives of $\Omega(\mathbf{F}_e)$ ($\Omega_m = \partial\Omega/\partial I_m$ and $\Omega_{mn} = \partial^2\Omega/\partial I_m \partial I_n$)
$\hat{\mathbb{I}}$, $\bar{\mathbb{I}}$, $\mathbb{I}$	Identity tensors in $\mathcal{B}_r$, $\mathcal{B}_\theta$, and $\mathcal{B}^{\text{II}}$
$\overline{\mathscr{I}}$, $\widetilde{\mathscr{I}}$, $\mathscr{I}$	Two-point identity tensors ($\overline{\mathscr{I}} = \delta_{a\alpha}\boldsymbol{E}_a^\theta \otimes \boldsymbol{E}_\alpha^r$, $\widetilde{\mathscr{I}} = \delta_{ni}\tilde{\boldsymbol{e}}_n \otimes \boldsymbol{e}_i$, and $\mathscr{I} = \delta_{i\alpha}\boldsymbol{e}_i \otimes \boldsymbol{E}_\alpha^r$)
$\widehat{\mathscr{I}}$	Two-point identity tensor between $\mathcal{B}_r$ and $\mathcal{B}_{\text{imp}}$
$\mathbf{u} = \dot{\mathbf{x}}$	Incremental deformation
$\dot{\mathbf{F}} = \left(\widetilde{\mathscr{I}}^{\mathrm{T}}\tilde{\mathbf{F}} - \mathbf{F}\right)$, $\dot{\mathbf{F}}_\theta$, $\dot{\mathbf{F}}_e$	Incremental deformation gradient and its thermal and elastic contributions
$\mathbf{L} = \dot{\mathbf{F}}\mathbf{F}^{-1} = \operatorname{grad}\mathbf{u} = \mathbf{L}_e + \mathbf{F}_e\mathbf{L}_\theta\mathbf{F}_e^{-1}$	Displacement gradient tensor and its thermal and elastic contributions
$\dot{\mathbf{T}}$, $\dot{\mathbf{T}}_0 = J^{-1}\mathbf{F}\dot{\mathbf{T}}$	The incremental nominal stress tensor and its push-forward version
$\dot{\mathbf{S}}$	The second incremental Piola-Kirchhoff stress tensor
$\dot{J}$, $\dot{J}_\theta$, $\dot{J}_e$	Incremental volume ratio and its thermal and elastic contributions
$\dot{\Theta}$	Incremental temperature
$\overset{\star}{\mathbf{T}}_0$	Objective stress rate of the push-forward version of the nominal stress tensor
$\mathbf{A}_0$, $\mathbf{M}_0$	Instantaneous material tensors of the 4th- and 2nd-order
$\dot{\mathbf{t}}_A$, $\dot{\mathbf{t}}_a$	Incremental surface traction on $\partial\mathcal{B}_r$ and $\partial\mathcal{B}^{\text{II}}$
λ_i	Pre-stretches (diagonal element of $\mathbf{F}$ where $i = 1, 3$)
Δ	Two-dimensional Laplacian
Φ_0, Ψ_0	Displacement functions
$\mathfrak{D}$, $\mathfrak{D}^\dagger$	Operator matrix and its adjugate
$\mathfrak{D}_{ij}^\dagger$	Cofactor of $\mathfrak{D}$ ($i, j = 1, 2, 3$)
$\xi_k^{(i)}$, Ψ_k	Quasi-harmonic functions ($i, k = 1, 2, 3$)
$\hbar_i$, s_k^2	Coefficients and roots of the biquadratic equation ($i = 0, 1, 2$; $k = 1, 2$) [Appendix A]
$z_k = s_k z$	Equivalent axial coordinate component ($k = 0, 1, 2, 3$)
α_k, β_k, γ_{jk}, ϖ_{jk}	Coefficients for combination of quasi-harmonic functions
w_1, σ_{zj}, $\sigma_{\rho i}$, $\sigma_{\phi i}$, $\sigma_{\rho t}$, $\sigma_{\phi t}$, σ_{zt}	Equivalent mechanical and thermal variables [Eqs. (14) and (15)]
S, a	Contact area and its radius in $\mathcal{B}_c$
d, $d^\natural$	Indentation depth and its counterpart considering indenter profile and adhesion
$f(\rho, \phi)$	Indenter profile function
ϑ	Half of the apex angle of a conical indenter
R	Radius of a spherical indenter
$W(\rho, \phi)$, $\check{P}(\rho, \phi)$, $P(\rho, \phi)$, $Q(\rho, \phi)$	Prescribed incremental axial surface displacement, heat flux, equivalent heat flux, and temperature on S
H_i, $\hat{H}_i$	Single layer potentials ($i = 1, 2$)
ω_i	Densities ($i = 1, 2$)
ς_{ki}, $\varsigma_{ki(\pm)}^{\{mnq\}}$, $\varsigma_{ki(\pm)\langle j\rangle}^{\{mnq\}}$, $\varsigma_{ki\langle j\rangle}^{\{mnq\}}$	Coefficients for combination of potentials ($k = 1, 2, 3$; $i = 1, 2$; $j = 1, 2$)
δ_{ji}	Kronecker delta
$l_1(\#)$, $l_2(\#)$	Equivalent radial coordinate components
$g(\#)$	Inverse of $l_1(\#)$ or $l_2(\#)$
$\mathcal{L}(\#)$	Poisson operator
$\mathcal{G}(\#, \#)$	Kernel in $\mathcal{L}(\#)$
$\mathcal{F}(\#)$, $\mathcal{F}^\natural(\#)$	Incremental indentation force and its counterpart considering indenter profile and adhesion
Λ, μ, ν	Dimensionless coefficient, shear modulus, and Poisson's ratio for a neoHookean material
$\mathfrak{L}_{\text{ALM}}(\mathbf{u}, \varrho)$	Augmented Lagrangian functional
Γ_c	Contact boundary
$\Pi(\#)$, $\Pi_{\text{int}}(\#)$, $\Pi_{\text{ext}}(\#)$	Total potential energy together with its internal and external contributions
$\langle\#\rangle_\pm$	Macaulay brackets
$\breve{g}_n(\mathbf{u})$	Normal gap
ϱ	Contact pressure multiplier
J	Penalty parameter
c, c_k, $c_{mnq} = mc_1 + nc_2 + qc_3$	Thickness and equivalent thickness of a hyperelastic film
$\mathcal{R}_0$, $\mathcal{R}_{mnq}$, $\mathcal{D}_0$, $\mathcal{D}_{mnq}$	Equivalent coefficients for combination of quasi-harmonic functions
$\mathcal{P}(\rho, \phi)$, $\mathcal{Q}(\rho, \phi)$, $\mathcal{W}(\rho, \phi)$	Equivalent external loadings
z_*	Shifted axial coordinate component
$\mathcal{K}_1$, $\mathcal{K}_2$	Kernels in Fredholm integral equation of the second kind

$\mathcal{N}_1[\#]$, $\mathcal{N}_2[\#]$	Contraction operators
$\omega_i^{[n]}$	The n-th approximation of density ω_i
$\omega_1^* = \omega_1\sqrt{a^2-\rho^2}$	Scaled density
Υ, ℓ	Amplitude of the waviness and its wavelength
$\mathfrak{V}$	Radial characteristic wavenumber
$\mathrm{M}(\rho)$	Function describing small scale surface topography
$\mathrm{N}(\rho)$	Transform of $\mathrm{M}(\rho)$
$\widehat{H}_v(\#)$	Struve function of the first kind
$\widehat{J}_v(\#)$	Bessel function of the first kind
${}_2\hat{F}_1(\#,\#;\#;\#)$	Gauss hypergeometric function
$\Gamma(\#)$	Gamma function
$\widehat{F}(\#,\#)$, $\widehat{E}(\#,\#)$, $\widehat{\Pi}(\#;\#,\#)$	Incomplete elliptic integral of the first, second, and third kinds
$\widehat{E}(\#)$	Complete elliptic integral of the second kind
$\hat{G}^{m,n}_{p,q}(z\vert^{a_1,\ldots,a_p}_{b_1,\ldots,b_q})$	Meijer G-function
$\vert\mathcal{F}_{\mathrm{JKR}}\vert$	Magnitude of the classical JKR maximum pull-off force
K_{I}	Incremental stress intensity factor
$\mathcal{E}_i(\#)$	Kernels in the densities ω_i $(i=1,2)$
G	Incremental energy release rate
δa, $\delta\rho$	Infinitesimal decrease in the contact radius and increment in the radial coordinate
$[\![w_1]\!]$	Incremental surface displacement discontinuity
η, η_{eff}	Work of adhesion and its effective counterpart
$\mathcal{A}$, $\mathcal{A}_p$	Actual and projected contact area
$\mathscr{F}[\#]$	Fourier transform
ξ	Variable in frequency domain
$\mathcal{O}(\#)$	Landau symbol
α_{KLJ}	Parameter for JKR adhesion
$\mathrm{Envelope}[\#]$	Envelope function
δ_1, δ_2	The first and second variations
$\mathcal{U}_0$	Space of displacement variation that is kinematically admissible
$\boldsymbol{\varepsilon}_{\mathrm{GL}}$	Green-Lagrange strain
$\mathrm{sym}(\#)$	Symmetric part of #
$\mathfrak{N}_{\mathfrak{n}}$	Shape function for the $\mathfrak{n}$-th node
$(\iota_1,\iota_2,\iota_3)$	Natural coordinates $(\iota_k\in[-1,1])$
$\mathbf{X}^e$, $\mathbf{X}^e_{\mathfrak{n}}$, $\mathbf{U}^e$, $\mathbf{U}^e_{\mathfrak{n}}$	Element position and displacement vectors together with their $\mathfrak{n}$-th node counterparts
$\mathbf{J}$	Jacobian matrix
$\mathbf{K}^e$, $\mathbf{R}^e$	Element tangent stiffness matrix and element residual vector
$\mathbf{K}_{\mathrm{mat}}$, $\mathbf{K}_{\mathrm{geo}}$	Material and geometric stiffness matrix
$\delta_2\mathbf{U}^e_{\mathrm{flat}}$	Variation of flattened element nodal displacement vector
$\mathcal{Y}$	Critical load factor
$\hat{\mathbf{\Phi}}$	Normalized buckling mode
$\mathbf{U}_{\mathrm{imp}}$, $\hat{\mathbf{U}}_{\mathrm{imp}}$	Nodal and analytical displacement induced by buckling imperfection
$\mathfrak{w}$	Buckling imperfection scale factor
$\hat{\kappa}_i$	Equivalent coefficient of thermal expansion $(i=1,3)$
$\mathcal{H}(\#)$, $\mathcal{T}_{k+j}=k+j-3\mathcal{H}(k+j-3)$	Heaviside step function and its modified counterpart
$\mathfrak{V}_n$	Shape parameters of an indenter
$\mathfrak{R}[\#]$, $\mathfrak{I}[\#]$	Real and imaginary part of #
$\mathscr{D}$	Domain $[0,a]\times[0,2\pi]$
$d_k(\#,\#)$	Metric
$\mathfrak{g}$	Dimensionless dissipation parameter
$\mathfrak{a}_\Theta$	Williams-Landel-Ferry factor at temperature Θ
$\check{v}_{\mathrm{ce}}$, $\check{v}_{\mathrm{in}}$	Velocities of the contact edge and the indenter
$a^\ddagger_{\mathrm{ref}}$, $d^\ddagger_{\mathrm{ref}}$	Non-dimensional reference contact radius and indentation depth
$\#^{\langle j\rangle}$	Physical quantities and coefficients prescribed in the film $(j=1)$ and substrate $(j=2)$
$\#^\ddagger$	Non-dimensional quantities
$\#^e$	Physical quantities in an element

$\#_{\text{env}}$	Envelope curves
$\#_0$	Reference quantities
$\|\|\#\|\|_\infty = \sup_{(\rho,\phi)} \|\#\|$	Supremum norm
$\boldsymbol{\Xi}_1 \cdot\cdot \boldsymbol{\Xi}_2$	$[\Xi_1]_{ij}[\Xi_2]_{ji}$
$\boldsymbol{\Xi}_1 \underset{2}{\circ} \boldsymbol{\Xi}_2$	$[\Xi_1]_{ij}[\Xi_2]_{ik}\boldsymbol{e}_k \otimes \boldsymbol{e}_j$
$\boldsymbol{\Xi}_1 \otimes \boldsymbol{\Xi}_2$	$[\Xi_1]_{ij}[\Xi_2]_{kl}\boldsymbol{e}_i \otimes \boldsymbol{e}_j \otimes \boldsymbol{e}_k \otimes \boldsymbol{e}_l$

References

Argatov, I.I., Lyashenko, I.A., Popov, V.L., 2023. Rate-dependent JKR-type decohesion of a cylindrical punch from an elastic substrate. Phys. Scr. 98 (5), 055905.
Barber, J.R., Ciavarella, M., 2000. Contact mechanics. Int. J. Solids Struct. 37 (1–2), 29–43.
Carlson, A., Bowen, A.M., Huang, Y., Nuzzo, R.G., Rogers, J.A., 2012. Transfer printing techniques for materials assembly and micro/nanodevice fabrication. Adv. Mater. 24 (39), 5284–5318.
Chen, L., Du, Y., Xu, R., Destrade, M., Lim, C.W., Chen, W., 2026. Fracture and crack-face stability of pre-deformed soft electroactive solids. J. Mech. Phys. Solids , 106772.
Chen, W., 2015a. Some recent advances in 3d crack and contact analysis of elastic solids with transverse isotropy and multifield coupling. Acta Mech. Sin. 31 (5), 601–626.
Chen, Y., 2015b. Applications of nanoimprint lithography/hot embossing: a review. Appl. Phys. a 121 (2), 451–465.
Chou, S.Y., Krauss, P.R., Renstrom, P.J., 1995. Imprint of sub-25 nm vias and trenches in polymers. Appl. Phys. Lett. 67 (21), 3114–3116.
Chou, S.Y., Zhuang, L., 1999. Lithographically induced self-assembly of periodic polymer micropillar arrays. J. Vac. Sci. Technol. B: Microelectron. Nanom. Struct. Process. Meas. Phenom. 17 (6), 3197–3202.
Ciavarella, M., 2016. On roughness-induced adhesion enhancement. J. Strain Anal. Eng. Des. 51 (7), 473–481.
Ciavarella, M., Papangelo, A., 2021. On the interaction of viscoelasticity and waviness in enhancing the pull-off force in sphere/flat contacts. Tribol. Lett. 69 (4), 127.
Derjaguin, B.V., Muller, V.M., Toporov, Y.P., 1975. Effect of contact deformations on the adhesion of particles. J. Colloid Interface Sci. 53 (2), 314–326.
Ding, H., Chen, B., Liang, J., 1996. General solutions for coupled equations for piezoelectric media. Int. J. Solids Struct. 33 (16), 2283–2298.
Dorfmann, L., Ogden, R.W., 2014. Nonlinear Theory of Electroelastic and Magnetoelastic Interactions. Vol. 1. Springer.
Dowaikh, M.A., Ogden, R.W., 1990. On surface waves and deformations in a pre-stressed incompressible elastic solid. IMA J. Appl. Math. 44 (3), 261–284.
Du, Y., Stewart, P., Hill, N.A., Yin, H., Penta, R., Köry, J., Luo, X., Ogden, R., 2023. Nonlinear indentation of second-order hyperelastic materials. J. Mech. Phys. Solids 171, 105139.
Fabrikant, V.I., 1989. Applications of Potential Theory in Mechanics: A Selection of New Results. Kluwer Academic Publishers, Dordrecht, Boston.
Fabrikant, V.I., 2004. Application of the generalized images method to contact problems for a transversely isotropic elastic layer. J. Strain Anal. Eng. Des. 39 (1), 55–70.
Fabrikant, V.I., 2011a. Contact problems for several transversely isotropic elastic layers on a smooth elastic half-space. Meccanica 46 (6), 1239–1263.
Fabrikant, V.I., 2011b. Numerical methods of solution of contact problems in layered media. Int. J. Comput. Methods Eng. Sci. Mech. 12 (2), 84–95.
Feng, Q., Chen, S., Liang, X., Yuan, W., Xu, Y., Wang, G., 2026. Statistical characteristic in contact response of random rough surface. J. Tribol. 148 (6), 061503.
Fuller, K., Tabor, D., 1975. The effect of surface roughness on the adhesion of elastic solids. Proceedings of the Royal Society of London. A. Mathematical and Physical Sciences 345 (1642), 327–342.
Greenwood, J.A., 2017. Reflections on and extensions of the fuller and tabor theory of rough surface adhesion. Tribol. Lett. 65 (4), 159.
Guduru, P.R., 2007. Detachment of a rigid solid from an elastic wavy surface: theory. J. Mech. Phys. Solids 55 (3), 445–472.
Guo, L.J., 2007. Nanoimprint lithography: methods and material requirements. Adv. Mater. 19 (4), 495–513.
Hertz, H., 1882. On the contact of elastic solids. Zeitschrift für Reine und Angewandte. Mathematik 92, 156–171.
Heyden, S., Bain, N., 2024. From a distance: shuttleworth revisited. Soft Matter 20 (28), 5592–5597.
Huang, G.-Y., He, J.-S., Ma, Z.-Y., 2026. A brief review of models for adhesive contact at the single-asperity level. Acta Mech. Solida Sin. , 1–10.
Huang, S., Li, B., Feng, X., 2008. Three-dimensional analysis of spontaneous surface instability and pattern formation of thin soft films. J. Appl. Phys. 103 (8).
Huang, Y., Xia, G., Zhou, W., Chen, W., 2016. On the green's functions for a two-phase soft electroactive medium subjected to biasing fields. Eng. Anal. Bound. Elem. 64, 137–149.
Jachymski, J., Jóźwik, I., Terepeta, M., 2024. The banach fixed point theorem: selected topics from its hundred-year history. Revista de la Real Academia de Ciencias Exactas, Físicas y Naturales. Serie A. Matemáticas 118 (4), 140.
Jesse, S., Nikiforov, M.P., Germinario, L.T., Kalinin, S.V., 2008. Local thermomechanical characterization of phase transitions using band excitation atomic force acoustic microscopy with heated probe. Appl. Phys. Lett. 93 (7).
Johnson, K.L., 1982. One hundred years of hertz contact. Proc. Inst. Mech. Eng. 196 (1), 363–378.
Johnson, K.L., 1995. The adhesion of two elastic bodies with slightly wavy surfaces. Int. J. Solids Struct. 32 (3–4), 423–430.
Johnson, K.L., Kendall, K., Roberts, A., 1971. Surface energy and the contact of elastic solids. Proc. R. Soc. Lond. a Math. Phys. Sci. 324 (1558), 301–313.
Kesari, H., Doll, J.C., Pruitt, B.L., Cai, W., Lew, A.J., 2010. Role of surface roughness in hysteresis during adhesive elastic contact. Philos. Mag. Philos. Mag. Lett. 90 (12), 891–902.
Kesari, H., Lew, A.J., 2011. Effective macroscopic adhesive contact behavior induced by small surface roughness. J. Mech. Phys. Solids 59 (12), 2488–2510.
Lan, H., Ding, Y., 2010. Nanoimprint Lithography. InTech Rijeka.
Lee, G., Zarei, M., Wei, Q., Zhu, Y., Lee, S.G., 2022. Surface wrinkling for flexible and stretchable sensors. Small 18 (42), 2203491.
Li, B., Cao, Y., Feng, X., Gao, H., 2012. Mechanics of morphological instabilities and surface wrinkling in soft materials: a review. Soft Matter 8 (21), 5728–5745.
Li, C., Liang, X., Yuan, W., Ding, Y., Wang, G., 2026. Size-dependent effects and surface roughness in contact mechanics. Appl. Mech. Rev. 78 (1), 010801.
Li, X., An, Y.H., Wu, Y.-D., Song, Y.C., Chao, Y.J., Chien, C.-H., 2007. Microindentation test for assessing the mechanical properties of cartilaginous tissues. J. Biomed. Mater. Res. B: Appl. Biomater.: off. J. Soc. Biomater. Jpn. Soc. Biomater. Aust. Soc. Biomater. Korean Soc. Biomater. 80 (1), 25–31.
Liang, X., Chen, S., Wang, S., Gong, Z., Feng, J., Wang, G., 2024. Adhesive contact of elastic solids with self-affine fractal rough surfaces. Acta Mech. Solida Sin. 37 (2), 265–270.
Linghu, C., Zhang, S., Wang, C., Song, J., 2018. Transfer printing techniques for flexible and stretchable inorganic electronics. Npj Flex. Electron. 2 (1), 26.
Lu, P., Foo, Y.L., Shen, L., Cheong, D. W.C., O'Shea, S.J., 2011. A general relation for contact stiffness including adhesion in indentation analysis. J. Mater. Res. 26 (11), 1406–1413.
Maugis, D., 1992. Adhesion of spheres: the JKR-DMT transition using a dugdale model. J. Colloid Interface Sci. 150 (1), 243–269.
Maugis, D., 2000. Contact, Adhesion and Rupture of Elastic Solids. Vol. 130. Springer Science & Business Media.
McKee, C.T., Last, J.A., Russell, P., Murphy, C.J., 2011. Indentation versus tensile measurements of young's modulus for soft biological tissues. Tissue Eng. B: Rev. 17 (3), 155–164.
Meitl, M.A., Zhu, Z.-T., Kumar, V., Lee, K.J., Feng, X., Huang, Y., Adesida, I., Nuzzo, R.G., Rogers, J.A., 2006. Transfer printing by kinetic control of adhesion to an elastomeric stamp. Nat. Mater. 5 (1), 33–38.
Mijar, A.R., Arora, J.S., 2004. An augmented lagrangian optimization method for contact analysis problems, 1: formulation and algorithm. Struct. Multidiscip. Optim. 28 (2), 99–112.
Mora, S., Abkarian, M., Tabuteau, H., Pomeau, Y., 2011. Surface instability of soft solids under strain. Soft Matter 7 (22), 10612–10619.

Mu, T., Li, R., Linghu, C., Liu, Y., Leng, J., Gao, H., Hsia, K.J., 2025. Nonlinear contact mechanics of soft elastic spheres under extreme compression. J. Mech. Phys. Solids 203, 106229.
Mu, T., Linghu, C., Liu, Y., Leng, J., Gao, H., Hsia, K.J., 2026. Universal scaling laws and a geometric mapping framework for deep indentation of soft materials. J. Mech. Phys. Solids , 106572.
Mukherjee, R., Sharma, A., 2015. Instability, self-organization and pattern formation in thin soft films. Soft Matter 11 (45), 8717–8740.
Narayanan, P., Pramanik, R., Arockiarajan, A., 2025. Leveraging instabilities in multifunctional soft materials: a cutting edge review. Adv. Eng. Mater. , 2500125.
Ogden, R.W., 1992. Nonlinear elasticity: incremental equations and bifurcation phenomena. In: Mathematics in Science and Engineering. Elsevier. 185, pp. 437–468.
Papangelo, A., Ciavarella, M., 2020. A numerical study on roughness-induced adhesion enhancement in a sphere with an axisymmetric sinusoidal waviness using lennard–jones interaction law. Lubricants 8 (9), 90.
Persson, B., 2002. Adhesion between an elastic body and a randomly rough hard surface. Eur. Phys. J. E 8 (4), 385–401.
Persson, B. N.J., Tosatti, E., 2001. The effect of surface roughness on the adhesion of elastic solids. J. Chem. Phys. 115 (12), 5597–5610.
Popov, V.L., et al., 2010. Contact Mechanics and Friction. Springer.
Rodriguez, E.K., Hoger, A., McCulloch, A.D., 1994. Stress-dependent finite growth in soft elastic tissues. J. Biomech. 27 (4), 455–467.
Schäffer, E., Thurn-Albrecht, T., Russell, T.P., Steiner, U., 2000. Electrically induced structure formation and pattern transfer. Nature 403 (6772), 874–877.
Sharma, A., Khanna, R., 1998. Pattern formation in unstable thin liquid films. Phys. Rev. Lett. 81 (16), 3463.
Wang, Y., Chu, J., Yuan, J., Kang, G., Chen, W., Li, X., 2025. Accurate prediction of contact stiffnesses of irregular interfaces. Int. J. Mech. Sci. , 110969.
Wang, Y., Du, Y., Xu, F., 2023. Strain stiffening retards growth instability in residually stressed biological tissues. J. Mech. Phys. Solids 178, 105360.
Wang, Y., Li, Z., Chen, X., Tan, Y., Wang, F., Du, Y., Zhang, Y., Su, Y., Xu, F., Wang, C., et al., 2024a. Electroactive differential growth and delayed instability in accelerated healing tissues. J. Mech. Phys. Solids 193, 105867.
Wang, Y., Zhao, J., He, Y., Yang, M., Chu, J., Yuan, J., Li, X., Chen, W., 2024b. Contact stiffness of the multi-indenter contact interface. J. Mech. Phys. Solids 188, 105659.
Wu, B., Sun, Y., 2023. Normal contact analysis between two self-affine fractal surfaces at the nanoscale by molecular dynamics simulations. Tribol. Lett. 71 (2), 30.
Xia, G., Hong, W., Chen, W., 2023. Indentation of pre-deformed compressible soft electroactive layer on substrate. Int. J. Mech. Sci. 238, 107834.
Xia, G., Huang, Y., Su, Y., Chen, W., 2020. Exact axisymmetric adhesive contact analysis for a pre-deformed soft electroactive half-space. Int. J. Solids Struct. 207, 206–229.
Xu, F., Huang, Y., Zhao, S., Feng, X., 2022. Chiral topographic instability in shrinking spheres. Nat. Comput. Sci. 2 (10), 632–640.
Yang, J., Jin, X., 2014. Indentation of a flat circular punch with uniform heat flux at its base into transversely isotropic magneto-electro-thermo-elastic half space. J. Appl. Phys. 115 (8).
Yu, H., Xu, M., Xu, W.-C., Liang, S., Wu, S., 2026. Designing resists for nanoimprint lithography enabling functional patterning. Chin. J. Chem. 44 (9), 1457–1472.
Zhang, W., Qian, J., Chen, W., 2012. Indentation of a compressible soft electroactive half-space: some theoretical aspects. Acta Mech. Sin. 28 (4), 1133–1142.
Zhu, Y., Zheng, Z., Zhang, Y., Wu, H., Yu, J., 2021. Adhesion of elastic wavy surfaces: interface strengthening/weakening and mode transition mechanisms. J. Mech. Phys. Solids 151, 104402.